



Transportation Consortium of South-Central States

Solving Emerging Transportation Resiliency, Sustainability, and Economic Challenges through the Use of Innovative Materials and Construction Methods: From Research to Implementation

Corrosion Management System of Regional Reinforced Concrete (RC) Bridges

Project No. 19STLSU10

Lead University: Texas A&M University

Collaborative Universities: Louisiana State University

Final Report
November 2020

Disclaimer

The contents of this report reflect the views of the authors, who are responsible for the facts and the accuracy of the information presented herein. This document is disseminated in the interest of information exchange. The report is funded, partially or entirely, by a grant from the U.S. Department of Transportation's University Transportation Centers Program. However, the U.S. Government assumes no liability for the contents or use thereof.

Acknowledgements

The authors would also like to acknowledge the technical discussion and co funding from AZZ and CMC. We would like to acknowledge the collaboration by Mike Stroia and Allen Scarborough from AZZ and CMC companies.

TECHNICAL DOCUMENTATION PAGE

1. Project No. 19STLSU10	2. Government Accession No.	3. Recipient's Catalog No.	
4. Title and Subtitle Corrosion Management System of Regional Reinforced Concrete (RC) Bridges		5. Report Date Nov. 2020	
		6. Performing Organization Code	
7. Author(s) PI: Homero Castaneda https://orcid.org/0000-0002-9252-7744 Co-PI: Ayman M. Okeil https://orcid.org/0000-0001-9685-9458		8. Performing Organization Report No.	
9. Performing Organization Name and Address Transportation Consortium of South-Central States (Tran-SET) University Transportation Center for Region 6 3319 Patrick F. Taylor Hall, Louisiana State University, Baton Rouge, LA 70803		10. Work Unit No. (TRAIS)	
		11. Contract or Grant No. 69A3551747106	
12. Sponsoring Agency Name and Address United States of America Department of Transportation Research and Innovative Technology Administration		13. Type of Report and Period Covered Final Research Report Aug. 2019 – Aug. 2020	
		14. Sponsoring Agency Code	
15. Supplementary Notes Report uploaded and accessible at Tran-SET's website (http://transet.lsu.edu/) .			
16. Abstract Civil infrastructure assets, including buildings, transportation networks, energy grids and networks, and water-sewer systems, are critical functional components of day-to-day life activity in a modern society. The durability and reliability of these civil infrastructures are largely affected by corrosion-induced structural deterioration. In addition to continual use and increasing traffic demands, natural environmental conditions set degradation due to corrosion damage as a critical condition to durable and reliable infrastructures. Therefore, in order to improve the durability of the bridge infrastructures affected by corrosion in the most efficient manor, we propose a procedure/methodology to manage integrity of corroding RC bridges which is resulted by corrosion assessment by assuming different initial RC systems (including control actions). Our approach involves corrosion characterization in laboratory scale RC samples, quantification of damage based on different corrosion conditions with different corrosion control technologies, and integration of proposed models of the environmental conditions effect on corrosion of RC. Finally, a methodology is included for assessing the component performance and reliability following the performance observed and characterized for different control actions. The corrosion assessment models include deterministic approach and localized probabilistic approach strategies in a system management tool for use by owner agencies in addressing vulnerable structures in aggressive environments. The proposed research consists of three technical tasks and implementations task. The final goal is to validate the methodology with the proposed tools for monitoring and modeling for the corrosion assessment.			
17. Key Words Corrosion Management, corrosion control, reliability, corrosion monitoring.		18. Distribution Statement No restrictions. This document is available through the National Technical Information Service, Springfield, VA 22161.	
19. Security Classif. (of this report) Unclassified	20. Security Classif. (of this page) Unclassified	21. No. of Pages 85	22. Price

Form DOT F 1700.7 (8-72)

Reproduction of completed page authorized.

SI* (MODERN METRIC) CONVERSION FACTORS

APPROXIMATE CONVERSIONS TO SI UNITS

Symbol	When You Know	Multiply By	To Find	Symbol
LENGTH				
in	inches	25.4	millimeters	mm
ft	feet	0.305	meters	m
yd	yards	0.914	meters	m
mi	miles	1.61	kilometers	km
AREA				
in ²	square inches	645.2	square millimeters	mm ²
ft ²	square feet	0.093	square meters	m ²
yd ²	square yard	0.836	square meters	m ²
ac	acres	0.405	hectares	ha
mi ²	square miles	2.59	square kilometers	km ²
VOLUME				
fl oz	fluid ounces	29.57	milliliters	mL
gal	gallons	3.785	liters	L
ft ³	cubic feet	0.028	cubic meters	m ³
yd ³	cubic yards	0.765	cubic meters	m ³
NOTE: volumes greater than 1000 L shall be shown in m ³				
MASS				
oz	ounces	28.35	grams	g
lb	pounds	0.454	kilograms	kg
T	short tons (2000 lb)	0.907	megagrams (or "metric ton")	Mg (or "t")
TEMPERATURE (exact degrees)				
°F	Fahrenheit	5 (F-32)/9 or (F-32)/1.8	Celsius	°C
ILLUMINATION				
fc	foot-candles	10.76	lux	lx
fl	foot-Lamberts	3.426	candela/m ²	cd/m ²
FORCE and PRESSURE or STRESS				
lbf	poundforce	4.45	newtons	N
lbf/in ²	poundforce per square inch	6.89	kilopascals	kPa

APPROXIMATE CONVERSIONS FROM SI UNITS

Symbol	When You Know	Multiply By	To Find	Symbol
LENGTH				
mm	millimeters	0.039	inches	in
m	meters	3.28	feet	ft
m	meters	1.09	yards	yd
km	kilometers	0.621	miles	mi
AREA				
mm ²	square millimeters	0.0016	square inches	in ²
m ²	square meters	10.764	square feet	ft ²
m ²	square meters	1.195	square yards	yd ²
ha	hectares	2.47	acres	ac
km ²	square kilometers	0.386	square miles	mi ²
VOLUME				
mL	milliliters	0.034	fluid ounces	fl oz
L	liters	0.264	gallons	gal
m ³	cubic meters	35.314	cubic feet	ft ³
m ³	cubic meters	1.307	cubic yards	yd ³
MASS				
g	grams	0.035	ounces	oz
kg	kilograms	2.202	pounds	lb
Mg (or "t")	megagrams (or "metric ton")	1.103	short tons (2000 lb)	T
TEMPERATURE (exact degrees)				
°C	Celsius	1.8C+32	Fahrenheit	°F
ILLUMINATION				
lx	lux	0.0929	foot-candles	fc
cd/m ²	candela/m ²	0.2919	foot-Lamberts	fl
FORCE and PRESSURE or STRESS				
N	newtons	0.225	poundforce	lbf
kPa	kilopascals	0.145	poundforce per square inch	lbf/in ²

TABLE OF CONTENTS

TECHNICAL DOCUMENTATION PAGE	II
TABLE OF CONTENTS	IV
LIST OF FIGURES	V
LIST OF TABLES	IX
ACRONYMS, ABBREVIATIONS, AND SYMBOLS	X
EXECUTIVE SUMMARY	XI
1. INTRODUCTION.....	1
2. OBJECTIVES.....	3
3. LITERATURE REVIEW	4
4. METHODOLOGY AND ANALYSIS.....	6
TASK 1: DEVELOP QUANTITATIVE ASSESSMENT METHODOLOGIES TO RANK THE PREVENTION OR CONTROL ACTION BY USING QUALITATIVE INDICES	6
4.1. Macroscopic approach based on weather conditions and macroparameters	6
4.2. Short terms experiments -accelerated conditions	10
4.3. Laboratory testing -steady state conditions.....	14
4.4. Steady-state conditions	17
TASK 2: DEVELOP A RELIABILITY MODEL FOR DIFFERENT CORROSION PREVENTION, CONTROL OR MITIGATION CONDITIONS	22
4.5. Design Space.....	23
4.6. Modeling of Time to Corrosion Initiation	25
4.7. Modeling of Pitting corrosion.....	27
4.8. Reliability Analysis.....	31
4.9. Sample Results.....	33
4.10. Concrete specimens with different rebar coatings (organic and inorganic)	40
4.11. Deterministic Modeling	61
5. RESULTS AND FINDINGS	75
TASK 3: DEVELOP A PROCEDURE FOR TRACKING THE PERFORMANCE OF CONTROL ACTIONS USED IN REINFORCED CONCRETE BRIDGE ELEMENTS BY COMPARING THE CURRENT METHODS	75
5.1. Corrosion Propagation Model: Based on mechanistic analysis of damage evolution ...	75
6. CONCLUSIONS	82
REFERENCES.....	83

LIST OF FIGURES

Figure 1. Damage evolution of the rebar in corrosive environments.	5
Figure 2. Damage evolution stages due to the classic steel rebar and galvanized layer as part of RC elements.	5
Figure 3. Spatial distribution of 30 year mean annual temperature and precipitation data in Texas. [From www.weather.com, www.noaa.gov].....	6
Figure 4. Spatial distribution of 30 year mean annual temperature and precipitation data in Louisiana. [From www.weather.com, www.noaa.gov].....	6
Figure 5. Spatial distribution of 30 year mean annual temperature and precipitation in New Mexico. [From www.weather.com, www.noaa.gov]	7
Figure 6. Spatial distribution of 30 year mean annual temperature and precipitation data in Oklahoma. [From www.weather.com, www.noaa.gov].....	7
Figure 7. Spatial distribution of 30 year mean annual temperature and precipitation in Arkansas. [From www.weather.com, www.noaa.gov].....	7
Figure 8. Spatial distribution of mean total chloride content (kg/ha) deposited over 30 years in Texas, Louisiana, Arkansas, New Mexico and Oklahoma. [From www.noaa.gov]	9
Figure 9. Spatial distribution of mean relative humidity over 30 years (1990-2020) in Texas, Louisiana, Arkansas, New Mexico and Oklahoma. [From www.noaa.gov].....	9
Figure 10. Artificial defect in rebar specimens exposed to salt spray test.....	11
Figure 11. Artificial defect in rebar specimens exposed to salt spray test following 7 cycles.	12
Figure 12. Photographs of the rebar specimens after different wet/dry cycles in the salt fog chamber.....	14
Figure 13. Stereo microscope images of the artificial defect in the rebar specimens exposed to the salt fog chamber after seven wet/dry cycles.	15
Figure 14. SEM micrographs and EDS maps of rebar specimens after seven wet/dry cycles in the salt fog chamber.....	16
Figure 15. Electrochemical set up for full-immersion test of rebar specimens in simulated concrete pore solution.	17
Figure 16. OCP results of (a) bare rebar (615) and 1055 coating and (b) galvanized coatings (767,1095,1035 (CM-z), 1035 (CS-) immersed for 30 days in a simulated concrete pore solution.	18
Figure 17. EIS spectra of the rebar specimens immersed for 30 days in a simulated concrete pore solution: a) 615, b) 1055, c) 1094, d) 767, e) 1035 (CM-z), f) 1035 (CM-z).....	22
Figure 18. Details of typical bridge used to cover design space (23)	23
Figure 19. Typical girder details (Okeil et al, 23).....	25

Figure 20. Pit configuration (43).	28
Figure 21. Pit configuration (34).	28
Figure 22. PDF vs. Location Parameter of Pitting Factor.....	33
Figure 23. Reliability Index vs. Time design space 1 WC46C12C135.....	34
Figure 24. Reliability Index vs. Time design space 1 WC46C15C135.....	34
Figure 25. Reliability Index vs. Time design space 1 cover WC46C18C135.....	35
Figure 26. Reliability Index vs. Time design space 2 WC46C11C130.....	35
Figure 27. Reliability Index vs. Time design space 2 WC50C11C130.....	36
Figure 28. Reliability Index vs. Time design space 2 WC53C.....	36
Figure 29. Reliability Index vs. Concrete Cover design space 1 at T=75 years.....	37
Figure 30. Reliability Index vs. Concrete Cover design space 2 at T=75 years.....	37
Figure 31. Reliability Index vs. Concrete Cover design space 3 at T=75 years.....	38
Figure 32. Time to Reliability Index Threshold design space 1.....	38
Figure 33. Time to Reliability Index Threshold design space 2.....	39
Figure 34. Time to Reliability Index Threshold design space 3.....	40
Figure 35. Set-up of tested concrete sample.....	41
Figure 36. (a-d) Bode plots of sample 1 and 2, (e-f) Nyquist plots of sample 1 and sample 2 of 615 steel in 1% NaCl.....	43
Figure 37. (a-d) Bode plots of sample 1 and 2, (e-f) Nyquist plots of sample 1 and sample 2 of 615 steel in 3.5% NaCl.....	44
Figure 38. (a-d) Bode plots of sample 1 and 2, (e-f) Nyquist plots of sample 1 and sample 2 of 1094 in 1% NaCl.....	45
Figure 39. (a-d) Bode plots of sample 1 and 2, (e-f) Nyquist plots of sample 1 and sample 2 of 1094 in 3.5% NaCl.....	46
Figure 40.(a-d) Bode plots of sample 1 and 2, (e-f) Nyquist plots of sample 1 and sample 2 of 1035 (CS-M) in 0% NaCl.....	48
Figure 41. (a-d) Bode plots of sample 1 and 2, (e-f) Nyquist plots of sample 1 and sample 2 of 1035 (CS-M) in 1% NaCl.....	49
Figure 42. (a-d) Bode plots of sample 1 and 2, (e-f) Nyquist plots of sample 1 and sample 2 of 1035 (CS-M) in 3.5% NaCl.....	50
Figure 43. (a-d) Bode plots of sample 1 and 2, (e-f) Nyquist plots of sample 1 and sample 2 of 1035 (CM-z) in 0% NaCl.....	51

Figure 44. (a-d) Bode plots of sample 1 and 2, (e-f) Nyquist plots of sample 1 and sample 2 of 1035 (CM-z) in 1% NaCl.....	52
Figure 45.(a-d) Bode plots of sample 1 and 2, (e-f) Nyquist plots of sample 1 and sample 2 of 1035 (CM-z) in 3.5% NaCl.....	53
Figure 46.(a-d) Bode plots of sample 1 and 2, (e-f) Nyquist plots of sample 1 and sample 2 of 1055 in 1% NaCl.....	54
Figure 47. (a-d) Bode plots of sample 1 and 2, (e-f) Nyquist plots of sample 1 and sample 2 of 1055 in 3.5% NaCl.....	55
Figure 48. Circuits used to fit the EIS data.....	56
Figure 49. Change in charge transfer resistance of 615 steel in (a) 0% NaCl, (c) 1% NaCl, (e) 3.5% NaCl and corrosion rates in (b) 0% NaCl, (d) 1% NaCl, (f) 3.5% NaCl with time.....	56
Figure 50. Change in charge transfer resistance of 1035 (CS-M) in (a) 0% NaCl, (c) 1% NaCl, (e) 3.5% NaCl and corrosion rates in (b) 0% NaCl, (d) 1% NaCl, (f) 3.5% NaCl with time.	58
Figure 51. Change in charge transfer resistance of 1035 (CM-z) in (a) 0% NaCl, (c) 1% NaCl, (e) 3.5% NaCl and corrosion rates in (b) 0% NaCl, (d) 1% NaCl, (f) 3.5% NaCl with time.	59
Figure 52. Change in charge transfer resistance of 1094 in (a) 0% NaCl, (c) 1% NaCl, (e) 3.5% NaCl and corrosion rates in (b) 0% NaCl, (d) 1% NaCl, (f) 3.5% NaCl with time.....	60
Figure 53. Change in charge transfer resistance of 1055 in (a) 3.5% NaCl and corrosion rates in (b) 3.5% NaCl with time.....	60
Figure 54: Stage 1 results for RC element with steel and galvanized steel.	61
Figure 55. Equivalent circuit model for EIS spectra of the rebar specimens immersed in a simulated concrete pore solution: (a) 615 CS, (b) 1055 (, (c) 767, (d) 1035, (e)1094.....	63
Figure 56. Diffusion impedance for EIS spectra of the cylindrical rebar specimens immersed in a simulated concrete pore solution.	63
Figure 57. Fitted EIS spectra based on equivalent circuit model for the rebar specimens immersed in a simulated concrete pore solution: (a) 615 CS, (b) 1055 (CGR+Epoxy), (c) 797, (d) 1035, (e) 1094.	64
Figure 58. Charge transfer phenomenon vs immersed time for 615 cs rebar specimens immersed in a simulated concrete pore solution.	65
Figure 59. Diffusion phenomenon vs immersed time for 615 cs rebar specimens immersed in a simulated concrete pore solution.	72
Figure 60. Charge transfer phenomenon vs immersed time for 1055 rebar specimens immersed in a simulated concrete pore solution.....	72
Figure 61. Charge transfer resistance vs immersed time for 767, 1035, and 1094 rebar specimens immersed in a simulated concrete pore solution.....	73

Figure 62. CPE of double layer phenomenon vs immersed time for 767,1035, and 1094 rebar specimens immersed in a simulated concrete pore solution.	73
Figure 63. Film resistance vs immersed time for 767,1035, and 1094 rebar specimens immersed in a simulated concrete pore solution.....	74
Figure 64. CPE of film vs immersed time for 767, 1035, and 1094 rebar specimens immersed in a simulated concrete pore solution.	74
Figure 65. Damage evolution of the loss of capacity and or increase in the loading conditions when the propagation stage dominates the process.....	76
Figure 66. Effect of different intervention strategies on expected service life.....	80
Figure 67. Bridges made with galvanized steel rebar.	81
Figure 68. Stages of rebar degradation correlated with observed impedance values.	82

LIST OF TABLES

Table 1. Environmental parameters range by considering different levels of corrosion mechanism influence.....	9
Table 2. Samples used for different rebar and coating layers.....	10
Table 3. Corrosion condition based on OCP values and corrosion rate.	18
Table 4. Qualitative index based on electrochemical results for the corrosion control systems simulating corrosion environment and RC conditions.	22
Table 5. Moment loads for design space 1.	24
Table 6. Moment loads for design space 2.	24
Table 7. Moment loads for design space 3.	24
Table 8. Chloride diffusion model parameters and statistics.....	25
Table 9. Water to cement ratio correction factor.	26
Table 10. Curing day correction factor.	26
Table 11. Interpolated chloride threshold values.....	27
Table 12. Load modifiers and factors for LRFD design equation.	30
Table 13. Statistical characteristics of random variables for each design space.	32
Table 14. Pitting factor for each design space.	33
Table 15: Properties of the concrete samples used in the study.	41
Table 16. 615 CS Samples and equivalent circuit values.	66
Table 17. 767 Samples and equivalent circuit values.	67
Table 18. 1035 (2) Samples and equivalent circuit values.	68
Table 19. 1055 Samples and equivalent circuit values.	69
Table 20. 1094 Samples and equivalent circuit values.	70
Table 21. Some examples of evaluation of NDE technologies used in the laboratory and in the field.	77
Table 22. Repair and corrosion control methods.	78
Table 23. Parameters considered for the study.	81

ACRONYMS, ABBREVIATIONS, AND SYMBOLS

AASHTO	American Association of State Highway and Transportation Officials
AC	Alternating Current
AIC	Akaike Information Criterion
BIC	Bayesian Information Criterion
CDF	Cumulative Distribution Function
COV	Coefficient of Variation
DC	Direct Current
DOT	Department of Transportation
EIS	Electrochemical Impedance Spectroscopy
FHWA	Federal Highway Administration
FORM	First Order Reliability Method
i_{corr}	Corrosion current density
LADOTD	Louisiana Department of Transportation and Development
LRFD	Load and Resistance Factor Design
LTRC	Louisiana Transportation Research Center
MCS	Monte Carlo Simulations
NACE	National Corrosion Association Engineers
OCP	Open Circuit Potential
RC	Reinforced Concrete
TAMU	Texas A&M University
w/c	Water to cement

EXECUTIVE SUMMARY

A team comprised of TAMU and LSU researchers performed a joint effort for developing a corrosion management tool based on general and local degradation rebar materials and reliability assessment models. One particular aspect is the natural degradation of the materials forming the reinforced concrete element while in service. The rebar/concrete system was studied in laboratory scale by simulating real or macroconditions. The conditions included general degradation (uniform corrosion) and local attack. For the damage evolution modeling of the RC elements, we followed the classical initiation, transition and propagation stages. The modeling included the mechanistic analysis based on electrochemical set up and quantification while the probability modeling was based on literature and also the laboratory experiments. The experimental results guided the pathway for the modeling of the reinforced concrete elements. The research team considered different corrosion control systems to identify and quantify with time the differences between the classical steel rebar and inorganic and organic coatings, that in principle extend the life of the RC element. The first set of experiments included a pore solution concrete simulation and the second RC elements with different rebar characteristics. The approaches lead to the procedure for corrosion management establishing a set of steps based on degradation of different materials used for reinforced elements. The final step planned for this project could not be included due to the circumstances. The step included the measurement of RC elements containing different rebar materials and corrosion control conditions. The measurement will be used to validate the proposed approach based on the characterization, sensing and modeling. It is apparent that the steps can be used for a field condition procedure and benefit greatly from a research project to develop an effective management system for corrosion damaged reinforced concrete bridge elements. The unique features of this management system include the methods for corrosion condition evaluation, the methods for assessing the structure condition and monitoring, methodology for selecting most suitable corrosion prevention and controls.

1. INTRODUCTION

In the US, DOTs in different states forming the Gulf of Mexico, such as Texas and Louisiana, corrosive environment prevails due to the humidity, temperature and salt content in the environment during operation conditions. Some inspection processes and control action practices cannot provide sufficient information that can be used for addressing corrosion-induced damage, since it does not include comprehensive corrosion assessment, reliable inspection tools and control actions based on quantitative testing and monitoring to analyze the extent of damage where general or local corrosion may be occurring and actions should, or were, taken. The classical corrosion process by Tutti (1) consists of two steps: initiation and propagation connected by a transition or activation stage. During the initiation step the corrosion precursors uptake the concrete structure as illustrated in Figure 1, the breakdown of the passive layer formed initially by the corrosion products on the rebar activate the metallic reinforcement. However, the location where this breakdown occur is not easy to characterize or estimate. The local activation conditions will propagate leading to a failure due to the loss of capacity in the RC elements. This process each stage can be extended or reduced depending on the current conditions of the structure and the surrounding environmental conditions. A large bridge inventory of over 610,000 bridges in the US requires routine inspection and maintenance. A significant portion of this inventory is subjected to corrosive precursors in the environment. Consequently, corrosion-induced damages to structural elements are one of the leading causes for damage, which consumes an enormous amount of annual budget for bridge maintenance, repair, inspection, and replacement.

Reinforced concrete structures are frequently exposed to aggressive/corrosive environments that can promote deterioration of their structural properties and shortening of their service life. Chloride-induced corrosion of reinforcing steel in concrete represents one of the most severe and common forms of reinforced concrete degradation. Diffusion and accumulation of chloride ions within the concrete matrix and at the metallic surface interface promote the breakdown of the passive film formed as a result of the high alkaline pH of concrete on the reinforcing steel, and the initiation of localized corrosion at the steel surface. This chloride-induced corrosion process can cause reduction of the cross-sectional area of the reinforcing steel and formation of voluminous corrosion products that can induce cracking and spalling of the concrete structure.

To prevent or mitigate this damage process, surface modification in terms of inorganic or organic coatings are proposed as a control corrosion action due to their claims of excellent corrosion protection before any metallic activation. These coatings prevent the ingress of the chloride ions to the metal surface; hence, slowing down the formation of corrosion products and subsequent failure. The corrosion products are less voluminous for the galvanized system, and the sacrificial protection mechanism produces species that can migrate to the concrete matrix pores. This product relocation process into the porous voids will not add or generate an additional local stress condition (2). The degradation process will be different than the bare steel making the system to have additional stages before failure. Each stage can take longer or shorter time depending on the interfacial mechanism. (b) illustrates the zinc layer added to the steel rebar.

The proposed research will develop a series of steps and methodologies for the characterization, quantification of corrosion-damaged RC elements and corrosion control actions so that the current management system can be improved to have more robust tools. Also, an important class of physical assets – RC bridges – can be preserved and be more reliable by mitigating corrosion induced damages in a cost-effective way. The proposed research provides the combination of quantification of corrosion control action in terms of the rebar approach based on the chemical

simulation and RC elements conditions. The theoretical framework for the general degradation of the rebar and the local attack is also included in the steps taken for the corrosion management. The integration between the deterministic degradation mechanisms of the rebar in RC elements with the performance in operation conditions when concrete properties vary can lead to a robust methodology to estimate the reliability. Using theoretical tools and experimental results, the proposed research provided methods for scientific assessment of reliability for the RC elements and robust degradation principles design for repair or control of critical RC structures exposed to corrosion environments. This research aims to address two important Center and DOT missions: 1) Preserve what we have – by providing best practice tools for preserving physical infrastructures and extending their service life; and 2) Implement a decision support system that helps streamline infrastructure operations.

2. OBJECTIVES

The main goal of this research is to develop a comprehensive and effective management system of corrosion-damaged RC structural elements. The management system will encompass several components: (i) model, characterization and methodologies for conducting corrosion assessment as well as in-depth corrosion control characterization for both uniform and local corrosion processes, (ii) methodologies for selecting the most suitable repair, inspection and corrosion control methods based on modeling to meet a generic and mechanistic qualitative index, (iii) methodologies for monitoring the component performance following the repair or control action, (iv) experiment-based and data driven probabilistic models of corroding RC structures.

Our team approach involves corrosion characterization in laboratory scale samples, quantification of damage based on different corrosion conditions at different stages for different corrosion control methods in rebars, characterization and corrosion quantification in RC elements, and integration of proposed models of the general and local attack leading to the reliability approach. Finally, a methodology will be developed for assessing the component performance and reliability following the prevention, repair or control action. The proposed models will be integrated in a system management algorithm/method in addressing metallic structures in aggressive environments. The proposed research consists of three technical tasks and implementations task.

3. LITERATURE REVIEW

Corrosion of the reinforced concrete (RC) structures has become an important threat for infrastructure reliability. Total of 55% of existing U.S. bridges are classified as “Fair” or “Poor” as of 2018 according to Federal Highway Administration (FHWA). Around 15% of RC bridges in the United State are estimated to be structurally deficient due to corrosion of the reinforcement. From the direct cost of \$22.6 billion for the aged infrastructures, \$8.3 billion is estimated for the annual replacement/repair of RC bridge structures (3). The critical factor influencing the performance of RC is the chemical/electrochemical degradation as described in Figure 2. Such chemical/electrochemical degradation could be approached by the effect of the surrounding environment, as it affects the chemical/electrochemical properties of the concrete and rebar. The estimation of such property change has been determined indirectly by several technologies and methods. (3-5) Modelling is one indirect method to estimate rebar degradation; different models have considered the chloride as the main corrosion precursor for reinforced rebar where a chloride concentration threshold initiates the rebar surface activation for corrosion process due to the passivation layer breakdown as previously described. The corrosion mechanisms present unique routes and challenges to estimate damage as a consequence of decrease in mechanical properties. The corrosion process can be initiated by carbonation, or a build up of chlorides at the rebar/concrete interface. The leading cause of corrosion is due to the ingress and buildup of chloride ions at the rebar/concrete interface. A passive layer is formed due to the high alkalinity of local environment (pH 12.5-14) (4), which can be broken down by local pH or from the buildup of chloride ions in a localized area. Carbonation will cause a lowering of the local pH, due to the reaction of CO₂ with pore water to form carbonates (CO₃²⁻) and bicarbonates (HCO₃⁻). The pH will be around 8.5 for carbonated concrete compared to 12.5-14 for fresh uncarbonated concrete (4). The corrosion of reinforcing steel will occur once a critical chloride threshold has been met (5, 6). Once the passive layer is destroyed the corrosion process will begin, where the anodic and cathodic reactions are (7):



When the anodic/cathodic reactions are influenced by the mass transport of chloride and oxygen to initiate the rebar activation, the breakdown of the passive layer occurs at local sites on the rebar surface. Another route to control the degradation stages is to enlarge or extend the stage initiation time. The failure could be delay by altering the interface or chemical/electrochemical reactions. Figure 2 shows a different approach by having an additional sacrificial layer on the steel rebar. A zinc layer functions a sacrificial and also protected layer added to the steel. The stages for the galvanized rebar propose a modification on the degradation stages. The initiation stage includes the activation of the zinc layer when the electrolyte reaches the surface followed by the propagation of zinc dissolution. The activation of the steel rebar is proposed to be reached at later point than the bare steel configuration (see Figure 2a). The activation and propagation of steel in principle should take more time than a standard carbon steel rebar system (8).

The use of epoxy coated rebar (ECR) began in the 1970's as a low cost low maintenance form of corrosion protection for reinforced concrete bridges, since then ECR has been used in over 20,000 reinforced concrete bridge decks (9). The epoxy coating on the rebar can only provide protection as long as the coating is intact or water has not diffused through the coating. ECR can become mechanically damaged during fabrication, transport, or construction of the reinforced structure.

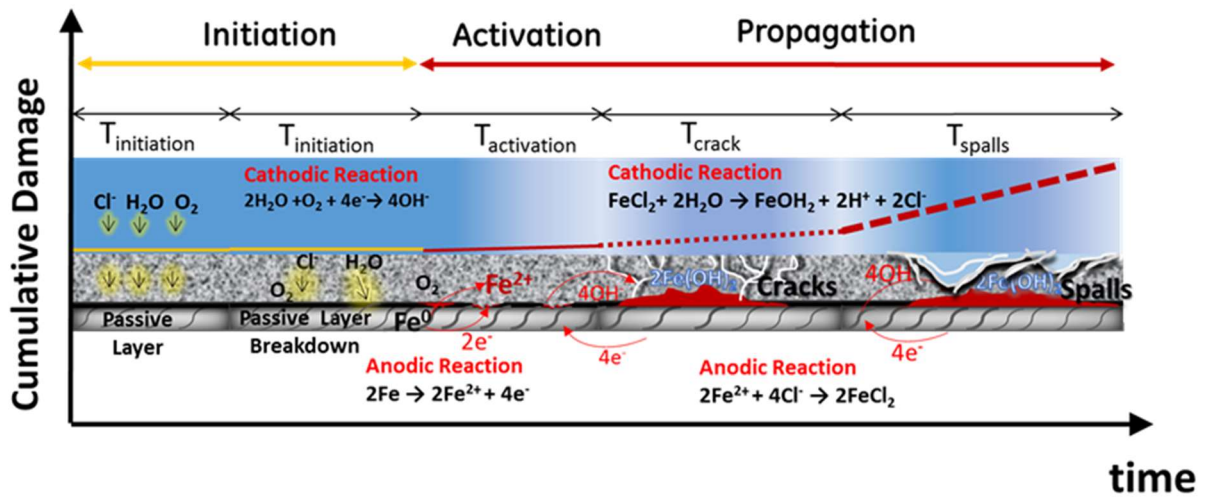


Figure 1. Damage evolution of the rebar in corrosive environments.

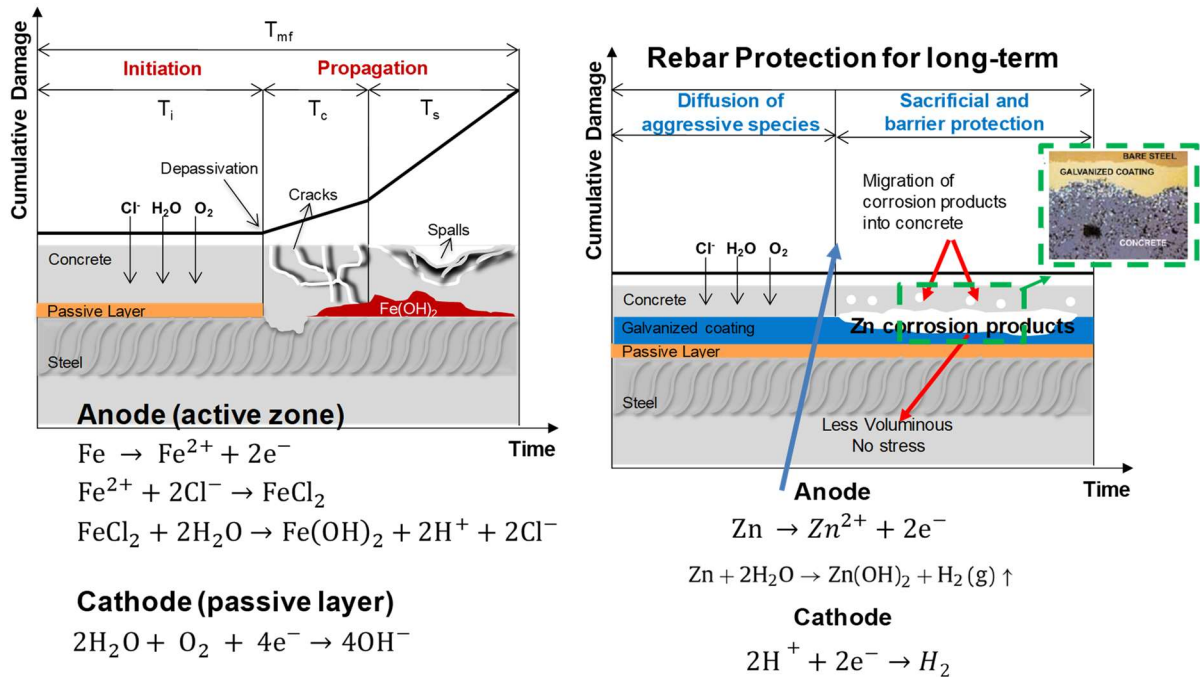


Figure 2. Damage evolution stages due to the classic steel rebar and galvanized layer as part of RC elements.

4. METHODOLOGY AND ANALYSIS

Task 1: Develop quantitative assessment methodologies to rank the prevention or control action by using qualitative indices

From the damage evolution point of view, Figure 1 describes different stages for the rebar degradation. The corrosion precursors will vary depending on the environmental conditions and the degradation mechanisms. The steel rebar has been known for several decades to have as the highest threat the accumulation of chlorides within the concrete matrix. The chloride content has been characterized for several works covering the relationship with the environmental parameters in the chloride uptake within the concrete. The location of the RC elements will have different impact in terms of the degradation mechanisms, the transport rate will depend on the parameters associated or influencing the mechanisms. For the initiation stage as described in Figure 2, either the steel rebar or coated (galvanized) rebar is activated by the electrolyte up taking the concrete matrix. The chloride will breakdown the passive layer while the electrolyte with oxygen content will initiate the electrochemical reaction with the zinc layer. Macro parameters as corrosion precursor agents will be distributed based on location and time. There are some critical parameters to consider when the corrosion control action is implemented for the RC elements or systems. The following section includes such parameters that account for the damage evolution of the environment and the critical parameters influencing corrosion mechanism.

4.1. Macroscopic approach based on weather conditions and macroparameters

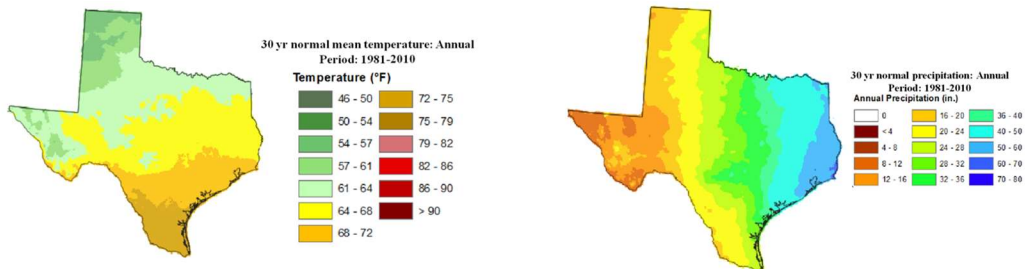


Figure 3. Spatial distribution of 30 year mean annual temperature and precipitation data in Texas. [From www.weather.com, www.noaa.gov]

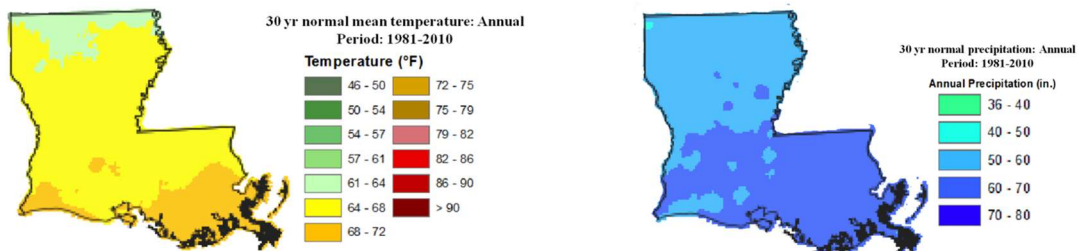


Figure 4. Spatial distribution of 30 year mean annual temperature and precipitation data in Louisiana. [From www.weather.com, www.noaa.gov]

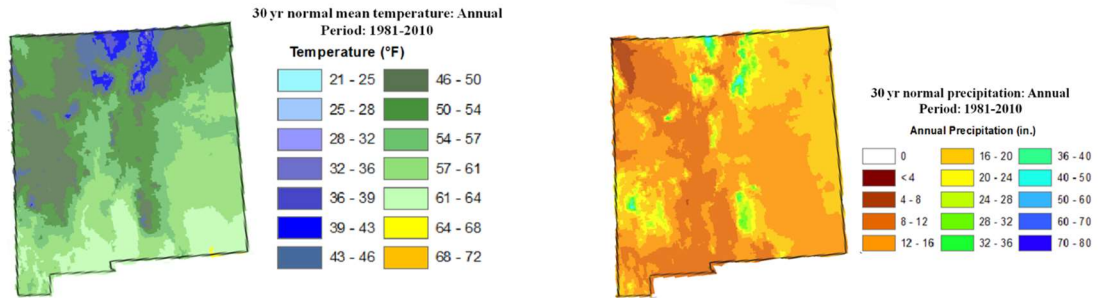


Figure 5. Spatial distribution of 30 year mean annual temperature and precipitation in New Mexico. [From www.weather.com, www.noaa.gov]

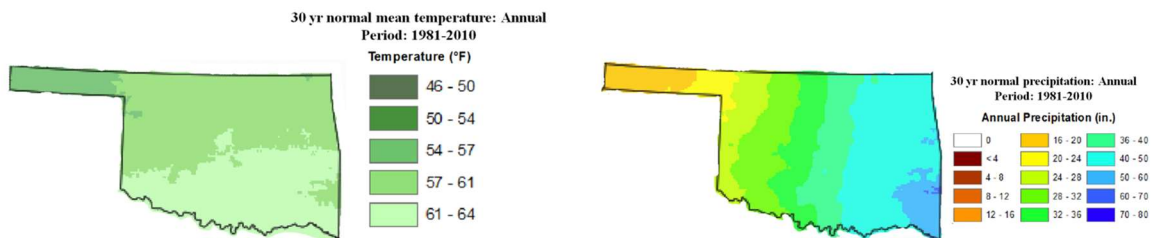


Figure 6. Spatial distribution of 30 year mean annual temperature and precipitation data in Oklahoma. [From www.weather.com, www.noaa.gov]

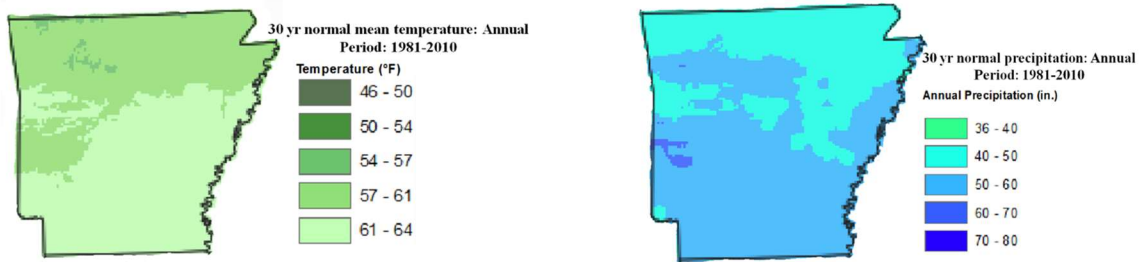
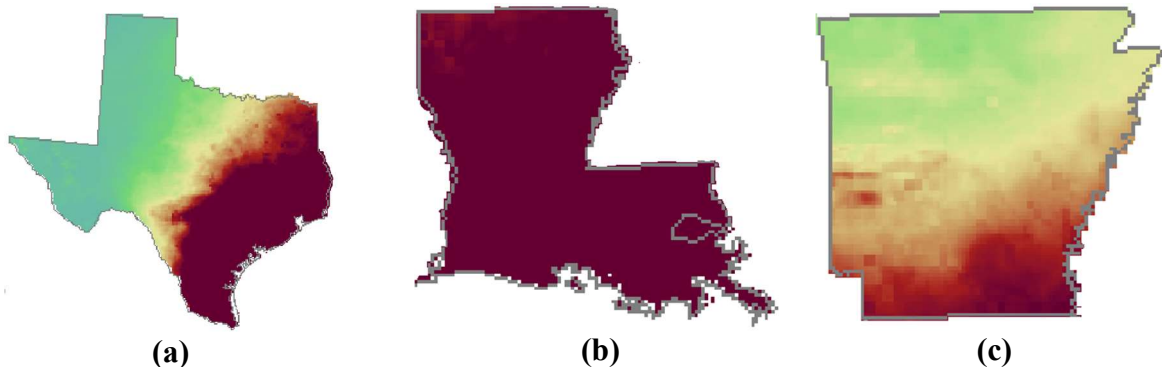


Figure 7. Spatial distribution of 30 year mean annual temperature and precipitation in Arkansas. [From www.weather.com, www.noaa.gov]

Figure 3-Figure 7 show the spatial distribution of mean temperature and annual precipitation averaged over 30 years (1981-2010) in Texas, Louisiana, New Mexico, Oklahoma and Arkansas. The humidity distribution averaged over 30 years (1990-2020) and the total precipitated chlorides are shown in Figure 8 and Figure 9 respectively. The temperature and humidity values cover a wide range of values over Texas which makes it important to understand how different regions within the same state can affect the corrosion mechanisms of the same concrete structure. Several correlations have been attempted to quantify each environmental parameter in terms of corrosion rate.

The expressions have been used based on qualitative approach and considering the field data acquired for some systems. Currently there is no rating in terms of environmental parameters that guide any estimation, The rating should be based on the influence in the corrosion mechanisms based on the proposed damage evolution models. The most critical parameters that can be related to the damage evolution of RC elements have been chlorides and moisture content, even with several works covering the two parameters the oxygen content should be considered as important parameter due to the cathodic reaction included in the corrosion mechanism. Due to the lack of estimation of the oxygen content as a solely parameter we can characterize it as indirect parameter the air content or also during the cycles of humidity content. The molecular oxygen will be dissolved in the electrolyte and participate in the electrochemical reaction. The parameter by itself is difficult to estimate but can be determine indirectly. The named critical parameters can be level as primer precurosrs for corrosion or firs level. Other set of macroparamters influencing the corrosion process and damage evolution for RC elements are indirect or second level parameters. The enviromental parameters such as temperature, precipitation, CO₂ content, can be categorized as paramters that influence eachmechanism occurring in each degradation stage. Temperature affects the transport of the species within the concrete matrix by influencing the tranSPORT of the electrolyte, the temperature has been used in different electrochemical correlations to characterize the rate of an homogeneous or heterogeneous mechanism. Indirectly the temperature with precipitation include an important paramter for the corrosion mechanism. Icyng conditions marks an important threath in the infrastructure system due to deicyng procedudres. When the addition of chemical to the roads, bridges and assets to melt and minimize the effect of the hazard conditions due to the ice layer, this latter produce condudtions for the addition of chlorides and chemicals producing corrosion condidtions. Precipitation parameter is proportional to the amount of potential water infiltrated or uptaking the RC elements or systems. The time of wetness and mass tranSfer mechanism is a process following the amount of water presented in a specific location and time. Then the temperature and precipitation can be considered second level parameters for corrosion mechanism not only because the implication in the mechanims but alos due to the effect in other parameters. The CO₂ content is an indirect paramter that participates in the corrosion mechanism process. The dissolution of the CO₂ in the electrolyte within the concrete structure will form carbonate and then bicarbonate species shifting the local conditions to be more acidic, the carbonation will influence in the breakdown of the passive layer for the steel rebar corrosion process. Also the acidic conditions will participate in the propagation of the corrosion process. There are more enviromental parameters that will directly or indirectly participate in the interfacial mechanism. Table 1 includes the concept of ranking in terms of primary parameters affecting the corrosion mechanism and the damage evolution process for the RC elements.



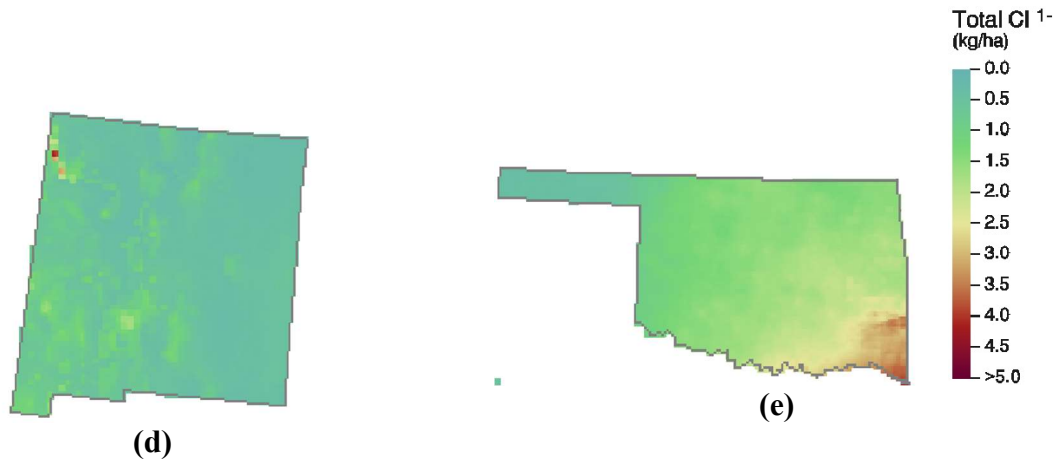


Figure 8. Spatial distribution of mean total chloride content (kg/ha) deposited over 30 years in Texas, Louisiana, Arkansas, New Mexico and Oklahoma. [From www.noaa.gov]

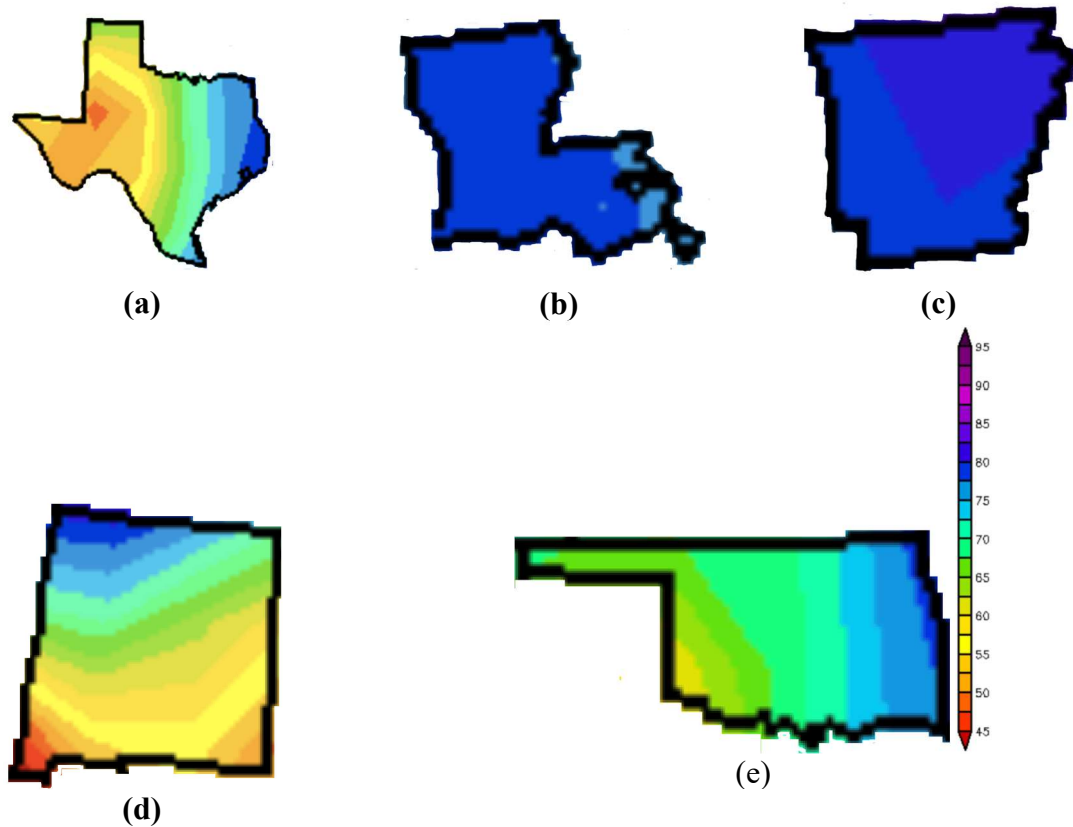


Figure 9. Spatial distribution of mean relative humidity over 30 years (1990-2020) in Texas, Louisiana, Arkansas, New Mexico and Oklahoma. [From www.noaa.gov]

Table 1. Environmental parameters range by considering different levels of corrosion mechanism influence.

Parameter	1 st level (critical parameter for steel/galvanized)	2 nd level Indirect or lower influence	3 rd level Lowest influence
Temperature	-20 ⁰ C to 0 ⁰ C	~20 ⁰ to 25 ⁰ C	~20 ⁰ to 25 ⁰ C

	and 30 °C to 50°C		
Precipitation	> 80 in	40 to 80 in	<8in
CO ₂	~0.002%	~0.002%	~0.002%
Humidity	70 to 90	50 to 70	<50
Total Chloride content	>4Kg/ha	1 to 4Kg/ha	<1 Kg/ha
Oxygen content	~21%	~21%	~21%

4.2. Short terms experiments -accelerated conditions

Table 2 illustrates the samples and the characteristics of the rebar and galvanized systems based on each layer and substrate. Short term experiments are included to characterize the corrosion products being formed during corrosion conditions. **Error! Reference source not found.** shows the activation stage for the steel rebar when there is a breakdown of the passive layer while new corrosion products are formed. The iron-based corrosion products have more volume than the original iron oxide layer originally formed and also the precipitation distribution. The galvanized steel exposed to corrosive environment illustrate the zinc-based corrosion products properties and distribution. The short term or accelerated testing included a pre-scratch sample on the coating, this latter also was to accelerate the corrosion products formation on the substrate surface.

4.2.1. Salt Spray Test with scratch and intact conditions

A different set of rebar specimens were placed in a salt spray chamber following the ASTM B117 standard “Standard Practice for Operating Salt Spray (Fog) Apparatus”. The ASTM standard gives a qualitative approach for accelerating conditions. This standard is not considered to be an indicative of performance but rather see the evolution and distribution of corrosion products under harsh conditions and how the distribution is in place for two different conditions. The first is an artificial defect on the outer coating and the second is an intact coating. This latter will show how the distribution of corrosion products occur in these conditions. An artificial defect of ~2.75 mm of diameter and 1 mm of penetration was done in the rebar samples using a drill bit of 1/8” as seen in Figure 10. The samples were exposed for 7 wet/dry cycles, in which each cycle consisted of 48 h wet followed by 48 h dry. Photographs were taken after each cycle to visually inspect the surface conditions of the rebar systems. In order to guarantee the reproducibility of the results, three samples of each formulation were tested.

Table 2. Samples used for different rebar and coating layers.

Sample number	Rebar	Galvanized system
No 615	Bare steel ASTM A615	NA
No 767	Bare steel ASTM A615	ASTM A767
No 1055	Bare steel ASTM A615	ASTM A1055
No 1094	Bare steel ASTM A615	ASTM A1094
No 1035 (CM-z)	ChromX ASTM A1035 (4100)	ASTM A1094
No 1035 (CS-z)	ChromX ASTM A1035 (9100)	ASTM A1094

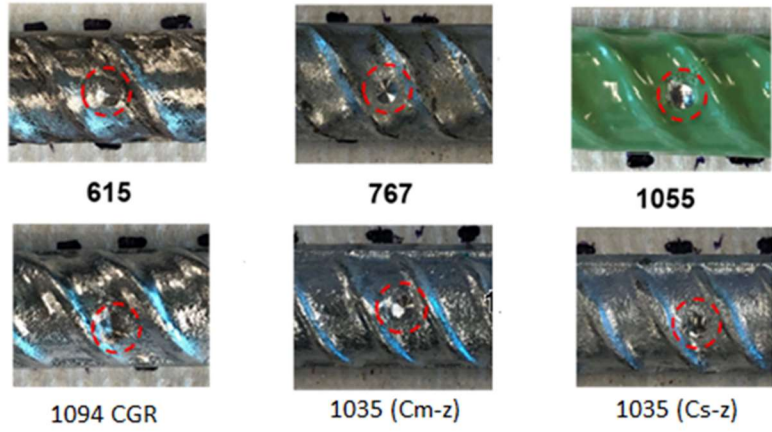
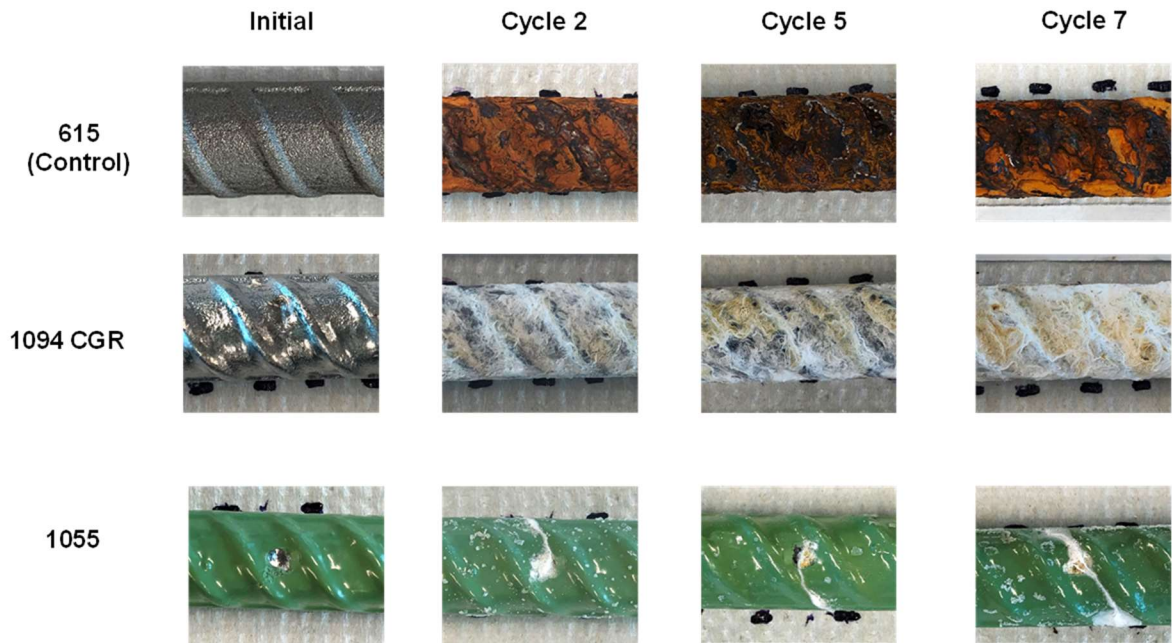


Figure 10. Artificial defect in rebar specimens exposed to salt spray test.



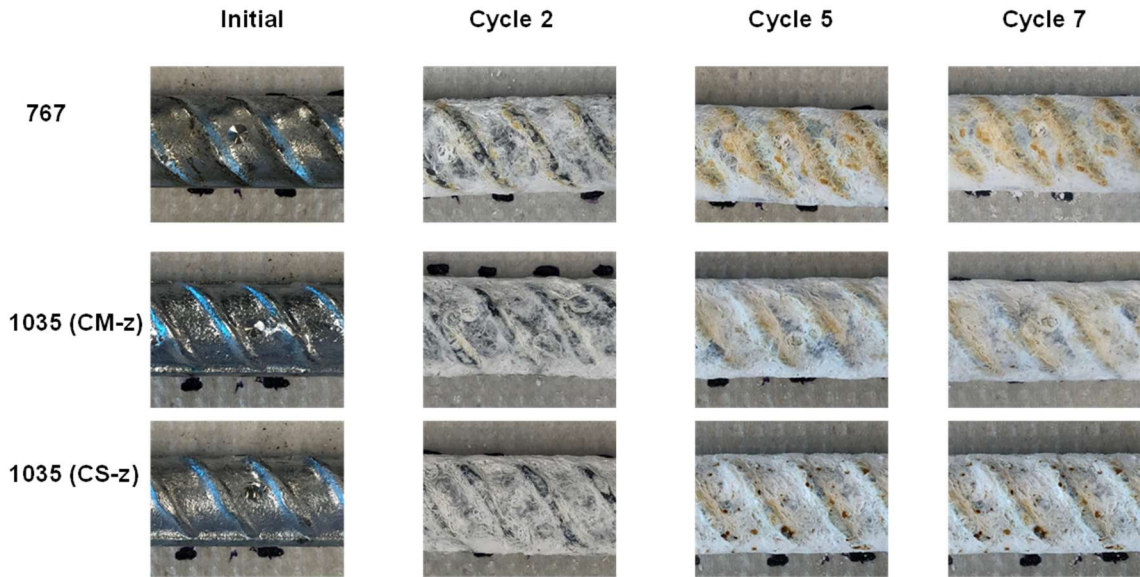


Figure 11. Artificial defect in rebar specimens exposed to salt spray test following 7 cycles.

Salt spray exposure was performed to provide a visual assessment of the corrosion protection performance of the coating systems as a function of exposure time. [6] Figure 12 shows photographs of the different coated rebar after exposure to salt spray fog chamber based on the methodology established by the ASTM B117 standard (as previously described for qualitative characterization of the products distribution along the area). After exposure for two wet/dry cycles, the bare steel rebar is completely covered by a thick layer of iron corrosion products. The 1055 rebar shows zinc corrosion products formed in the artificial defect and no signs of degradation or accumulation of corrosion products in other regions. These results show that the 1055 coating can provide a dual corrosion protection, whenever the coating is intact (without previous induced defects), it can provide an excellent barrier protection, but in the presence of an artificial defect, the galvanized coating underneath the epoxy primer can provide effective sacrificial protection to the exposed reinforcing steel. The galvanized rebar samples are completely covered by zinc corrosion products after two wet/dry cycles indicating that these coatings provide sacrificial protection to the steel substrate. After five wet/dry cycles corrosion products were formed on the galvanized rebar specimens producing more homogeneous corrosion product distribution and less volumetric with respect to bare steel samples (ASTM A615).

Figure 13 shows stereo microscope images of the artificial defect introduced in the rebar specimens that were exposed to the salt spray fog chamber after seven wet/dry cycles. The bare steel rebar was completely covered by iron corrosion products. The 1055 rebar shows no sign of corrosion in the intact regions of the coatings and a combination of iron and zinc corrosion products formed in the artificial defect. The intact regions of the galvanized coatings are mainly covered by zinc corrosion products. The 1094 rebar samples show activation along the exposed area with a good distribution of the corrosion products (zinc and iron products). The 1035 rebar samples show surface activation following the exposure the corrosion products cover in the entire surface with a homogeneous distribution. The volumetric difference following the salt spray exposure is noticeable for the color and the expanded products (rust color) from the bare steel (ASTMA615) and the galvanized samples (1094, 767 and 1035).

Figure 14 shows SEM micrographs and their corresponding EDS maps of selected rebar specimens after seven wet/dry cycles in the salt fog chamber. Images and EDS maps of the defect and a transverse rib are shown for different samples. After exposure to the salt fog chamber, the defect in the 1094 rebar shows the presence of a thin inner layer of zinc corrosion products and a thicker outer layer of iron corrosion products. This latter agrees with the macro-optical images that shows a high accumulation of iron and zinc corrosion products distribution at the induced defect. These results indicate that the 1094 coating was able to provide sacrificial protection to the exposed steel substrate for certain number of cycles but then, corrosion of the substrate occurred resulting in the formation of a surface amount of iron corrosion products. Looking at one of the transverse ribs, it is seen that only zinc corrosion products were formed, suggesting that whenever the coating is intact, the 1094 coating can provide an effective sacrificial protection to the underneath steel substrate. In addition, it can be only seen that metallic zinc is still available to provide sacrificial protection for a longer exposure time. The 1055 coating also shows the presence of zinc and iron corrosion products in the defect, also indicating that the coating provided a short-number of cycles sacrificial protection and a further corrosion of the steel substrate.

In one of the transverse ribs, it can be seen that most of the galvanized coating remained intact after the test with a very small, localized anomaly region. In addition, no evidence of iron corrosion products was detected. These results suggest that the intact 1055 coating provides an excellent corrosion protection, and the galvanized coating underneath of the epoxy primer was a second line of control but remained uncorroded. Interestingly, the 1035 coatings show the formation of mainly zinc corrosion products in the defect, suggesting that these coatings were effective in providing sacrificial protection even in regions where the bare steel was directly exposed to the aggressive environment. In the transverse ribs, there was formation of mainly zinc corrosion products with no evidence of iron corrosion products, also demonstrating the high effectiveness of these coatings in providing cathodic protection to the steel substrate.

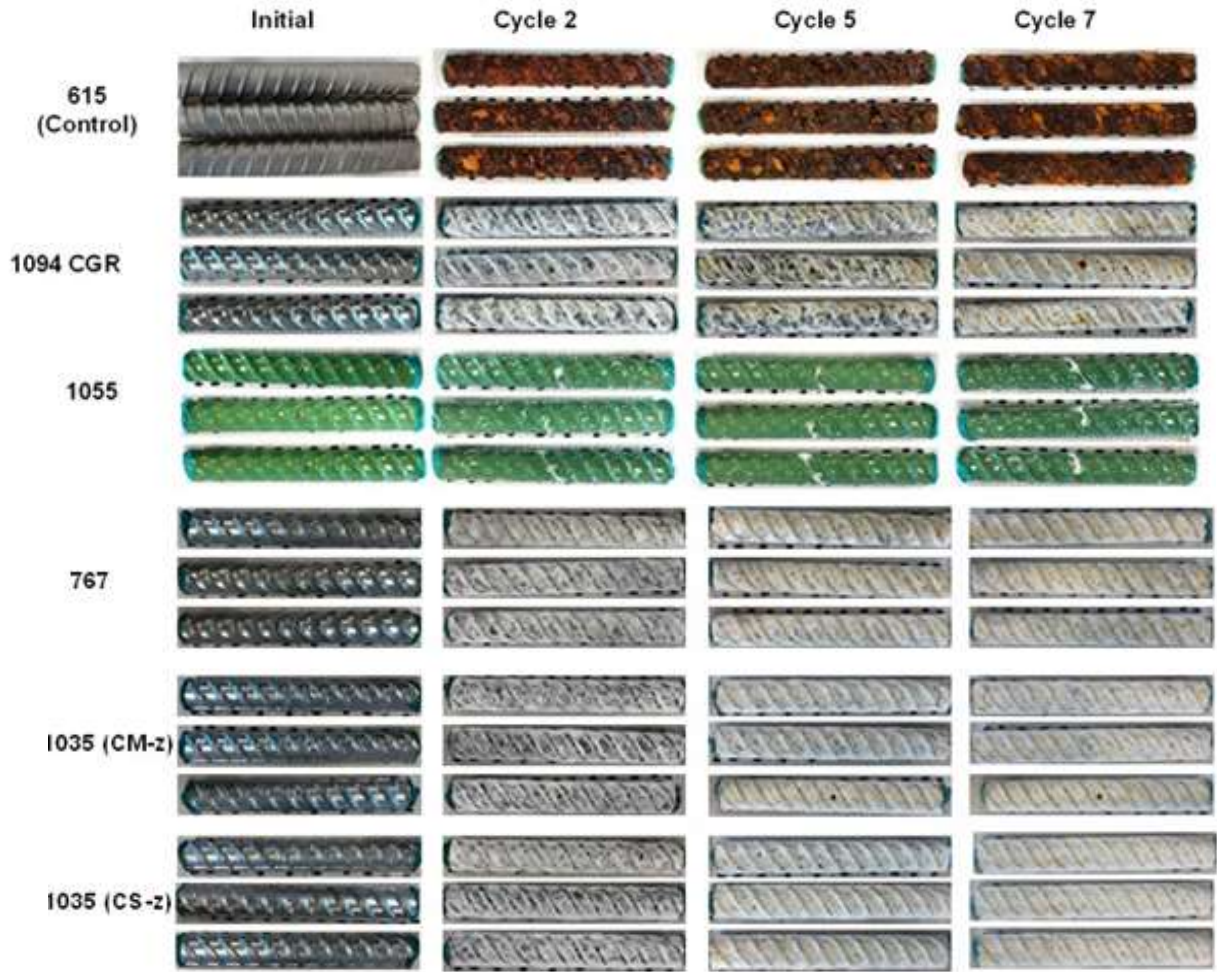


Figure 12. Photographs of the rebar specimens after different wet/dry cycles in the salt fog chamber.

4.3. Laboratory testing -steady state conditions

Long term experiments included steady state conditions. Figure 2 illustrates different stages proposed when different RC elements are exposed to corrosion environments. There are two different simulation conditions, the first covers as initial condition the activation stage. The samples illustrated in Table 2 will be exposed to the concrete pore solution environment, the conditions will skip stage 1 and start as the initial condition to have activation, the sample will be in contact with the electrolyte at initial time. Also, the chloride concentration to be used is higher than the threshold needed for the activation stage in the case of the steel rebar. The galvanized samples will be exposed to pore solution and will skip stage 1.

The second set of experiments include RC elements (from Table 2) with different rebars, this second conditions will simulate the complete damage evolution of the samples. This latter set will be described in part 3.

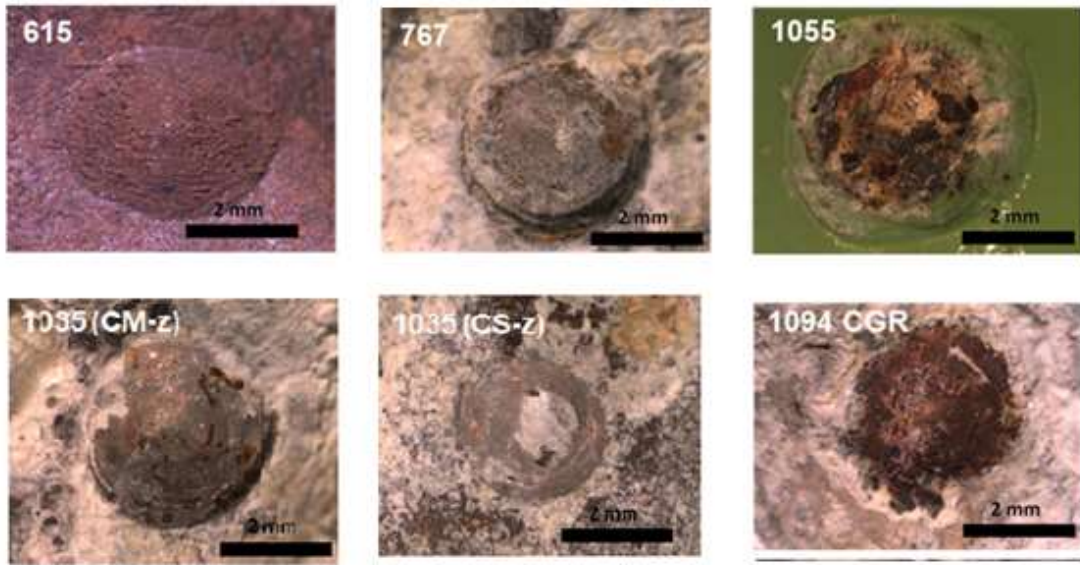
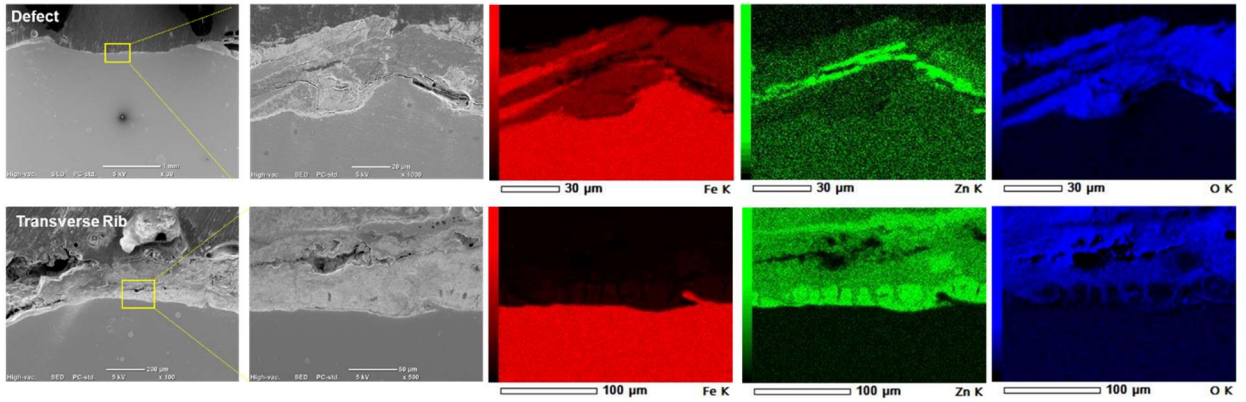
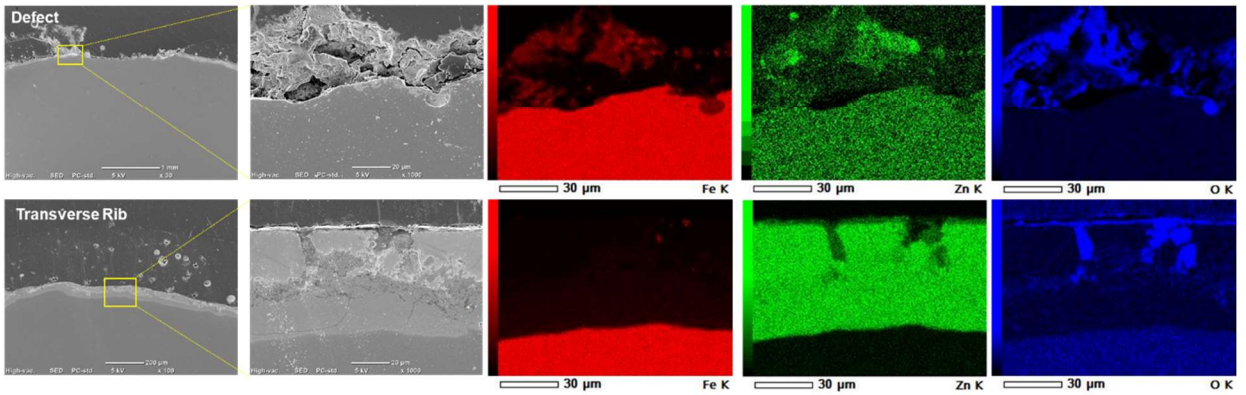


Figure 13. Stereo microscope images of the artificial defect in the rebar specimens exposed to the salt fog chamber after seven wet/dry cycles.

1094



1055



1035 (CS-z)

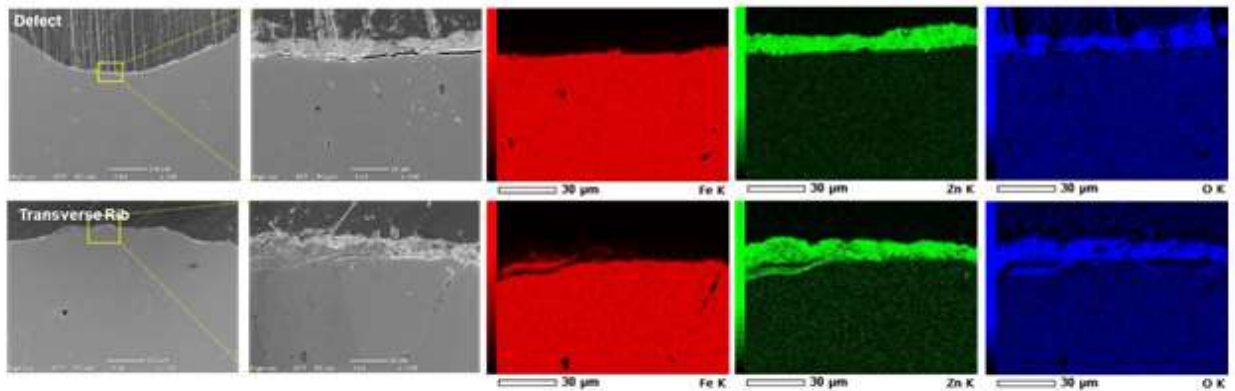


Figure 14. SEM micrographs and EDS maps of rebar specimens after seven wet/dry cycles in the salt fog chamber.

4.3.1. Full-immersion test -Initial condition Stage 2 (pore solution simulation)

For the full immersion testing, an electrochemical cell was designed to characterize each system in this task for short and medium-term exposure. The substrate/coating sample serves as the working electrode in a typical 3-electrode electrochemical cell set up; the sample characteristics include the selected coated metallic substrates. The mechanisms encountered at the metallic coating-electrolyte interface were coded in qualitative/quantitative analysis. The results were correlated with physical characteristics of the coating layer, and interfacial mechanisms due to the influence of each element by the coating. We employed open circuit potential (OCP) technique for rebar active-passive behavior and electrochemical impedance spectroscopy (EIS) method to characterize the performance as a function of physical features within the coating layer and/or metallic substrates in different electrolyte conditions. OCP and EIS measurements were performed in a Gamry, Interface 1000TM Potentiostat/Galvanostat/ZRA using the three-electrode configuration shown in Figure 15 where the rebar specimens were used as the working electrode, a saturated calomel electrode was used as the reference electrode and a graphite rod was used as the counter-electrode. The electrolyte solution was a simulated concrete pore solution that consisted of 0.08 M KOH, 0.02 M NaOH, 0.001 M Ca(OH)₂, 0.5 M NaCl and has a pH of about 12. The OCP measurements were performed for 10 min followed by EIS measurements at OCP in a frequency range from 100 kHz to 10 mHz with a sinusoidal amplitude of 10 mV. The immersion test was performed for more than 13 months.

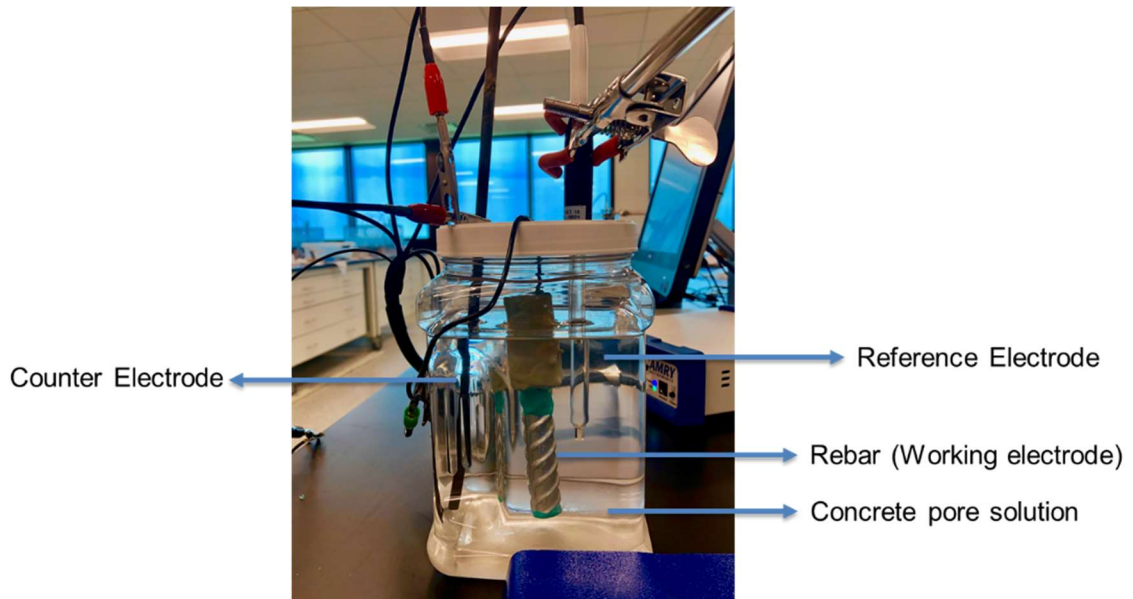


Figure 15. Electrochemical set up for full-immersion test of rebar specimens in simulated concrete pore solution.

4.4. Steady-state conditions

(a) Open Circuit Potential (OCP)

The sacrificial protection behavior of galvanized rebar samples is commonly studied by monitoring the OCP of the system. Metallic zinc exhibits highly negative OCP values of about -1.4 V vs. SCE when exposed to simulated concrete environments. The NACE standard 0290 “Impressed Current Cathodic Protection of Reinforcing Steel in Atmospherically Exposed Concrete Structures” proposes two criteria for cathodic protection in reinforced concrete structure: 1) a 100-mV polarization development/decay and 2) the E-log I test [8]. According to the first criterion, a minimum of 100 mV of polarization must be achieved to guarantee effective sacrificial cathodic protection of reinforcing steel embedded in concrete. This means that the electrode potential under cathodic protection must be at least 100 mV more negative than the electrode potential of bare reinforcing steel under the same exposure conditions. Figure 11 shows the OCP values for the different rebar specimens immersed for 30 days in the simulated concrete pore solution. The 30 days of exposure illustrates the NACE standard for a metallic coupon and weight loss measurements, the corrosion rate is taken at 28 days. The evolution of OCP for the bare rebar and the different coatings is separated in two plots as seen in Figure 16. Figure 16(a) shows the OCP evolution of bare steel (615) and the 1055 coating (dual coat-galvanized and epoxy), while Figure 16(b) shows the OCP evolution of the galvanized coatings. This is because there are different criteria to evaluate the corrosion behavior of bare rebar (and organic coatings) and galvanized rebar according to the OCP values. For bare steel and organic coated-rebar in concrete, the corrosion degree is assessed based on the OCP values reported by Broomfield et al. (8) shown in Table 3. From Table 3, it is seen that bare rebar is in a passive condition when the OCP is less than -50 mV vs. SCE. In contrast, there is a high risk of corrosion when the OCP values are more negative than -426 mV vs. SCE. These two conditions are depicted in Figure 16(a). Figure 16(a), it is seen that the bare steel is actively corroding after three days of immersion due to the presence of chloride ions (higher concentration than the breakdown threshold) in the solution that induces

the breakdown of the passive film and the initiation of corrosion. The OCP values of the 1055 coating are similar to the values of the bare rebar. These results suggest that corrosion of the steel substrate underneath the coating might also occurred. However, it is also possible that these values are associated with an IR drop developed through the coating that induces a more negative OCP value than the actual value. For the case of the galvanized rebar, we assessed the performance of these specimens according to the cathodic protection criterion mentioned above. In this study, the OCP of the bare rebar in the simulated concrete pore solution is about -500 mV vs. SCE (see Figure 16(a)). Therefore, we defined the cathodic protection limit as -600 mV vs. SCE following the 100-mV polarization development/decay. The OCP values of the majority of galvanized rebar were below the cathodic protection limit suggesting that during 30 days of immersion, they were effective in providing sacrificial protection to the reinforcing steel.

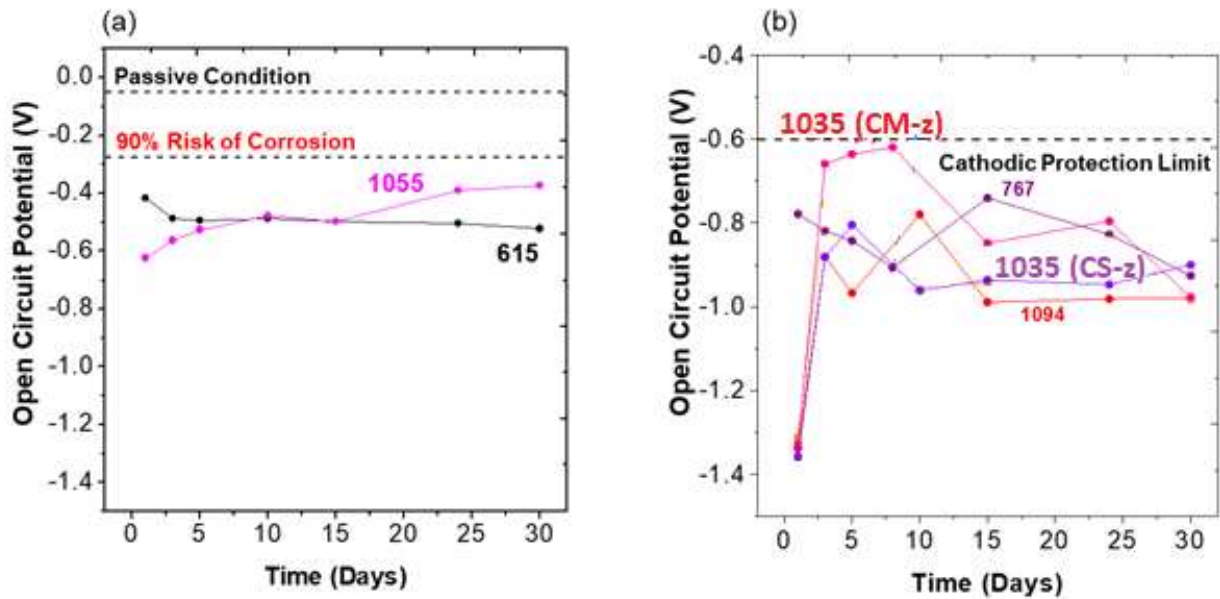


Figure 16. OCP results of (a) bare rebar (615) and 1055 coating and (b) galvanized coatings (767,1095,1035 (CM-z), 1035 (CS-)) immersed for 30 days in a simulated concrete pore solution.

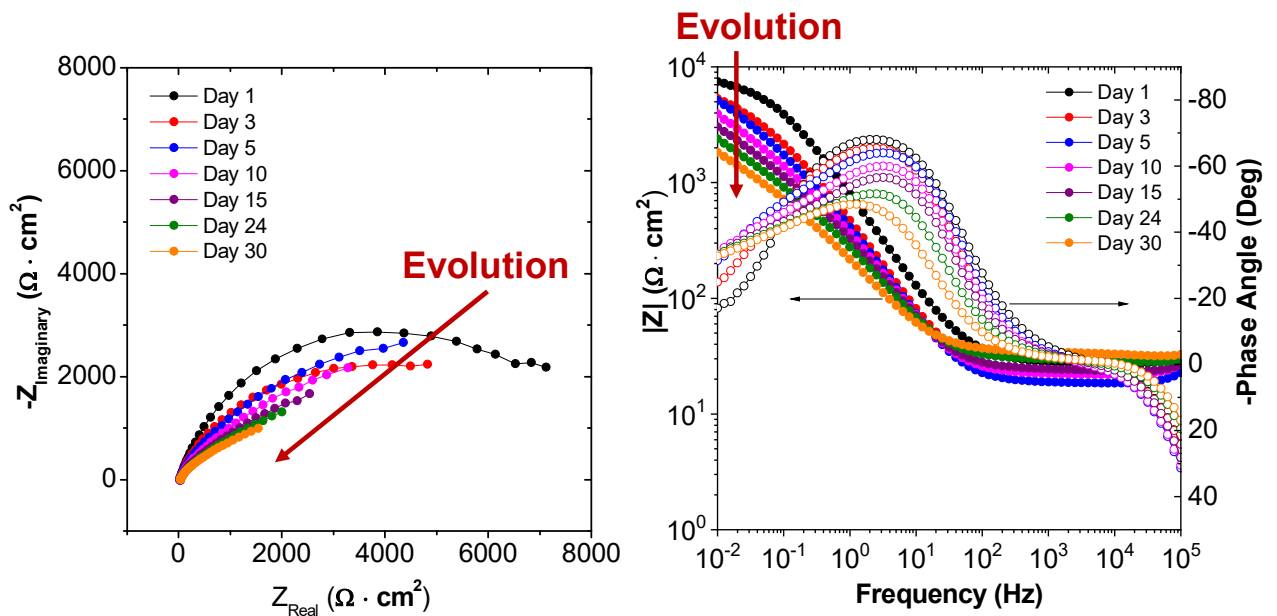
Table 3. Corrosion condition based on OCP values and corrosion rate.

Corrosion potential (mV vs SCE)	Corrosion rate ($\mu\text{A}/\text{cm}^2$)	Corrosion condition
<-50	<0.1	Passive condition
-50 to -126	0.1 to 0.5	Low (<0.1%) risk of corrosion
-126 to -276	0.5 to 1	Intermediate (~ 50%) corrosion risk
-276 to -426	1 to 1.5	High (>90%) risk of corrosion
<-426	> 1.5	Severe corrosion

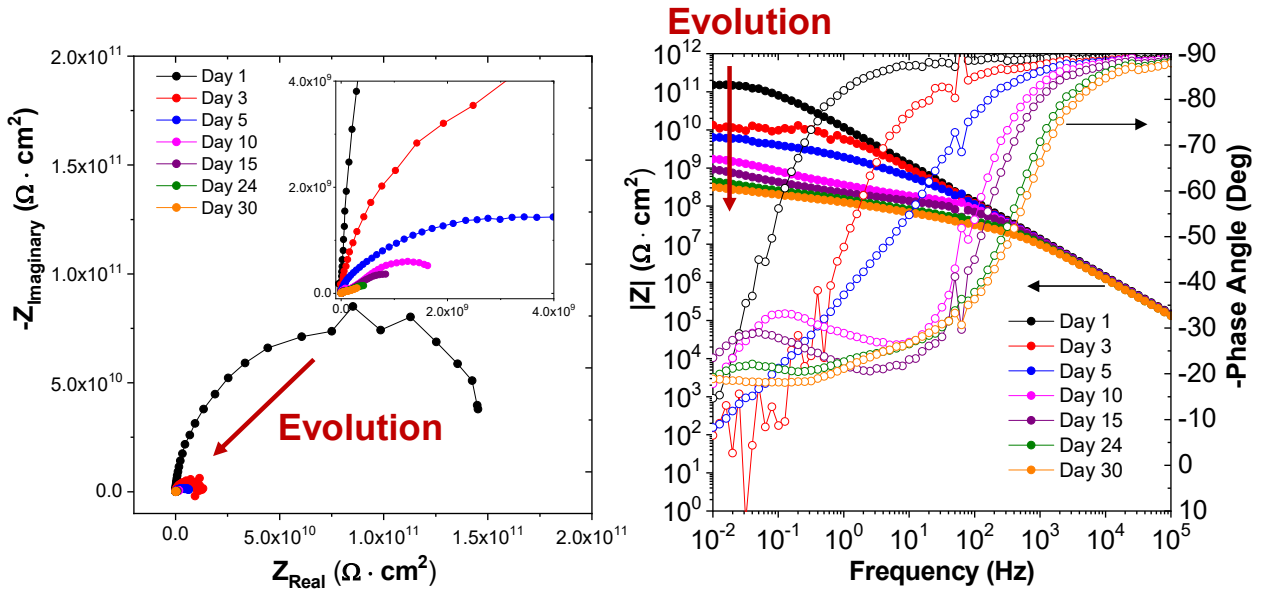
(b) *Electrochemical Impedance Spectroscopy (EIS)*

Electrochemical impedance spectroscopy was performed in order to provide additional information about the mechanisms of corrosion degradation of the different rebar specimens. The

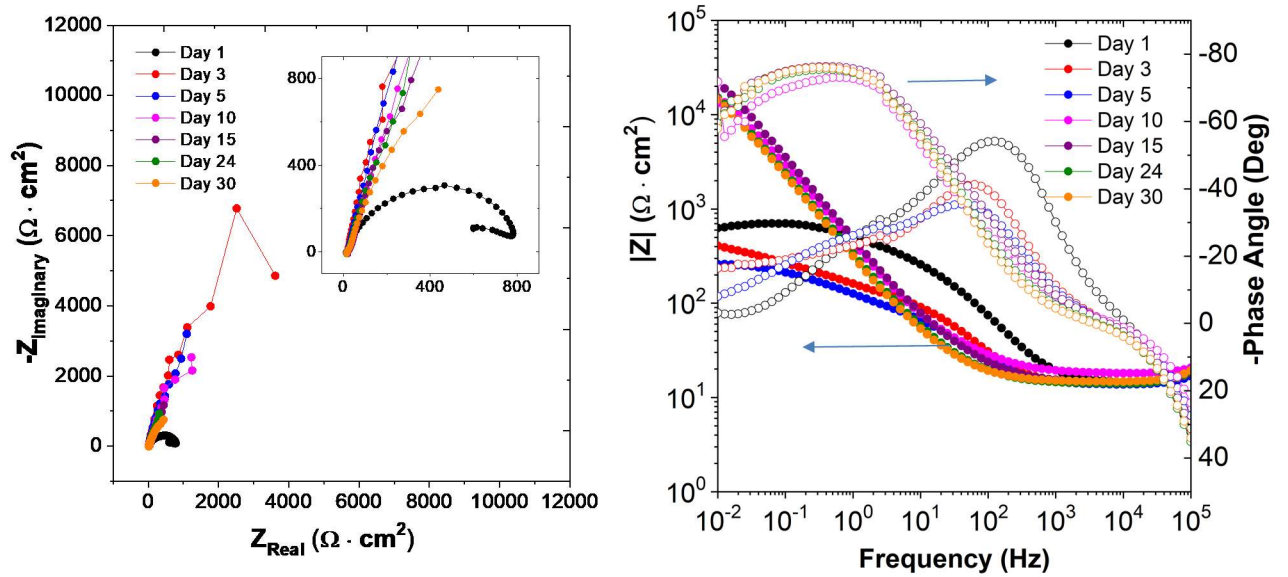
evolution of the Nyquist and Bode representations for the rebar specimens during 30 days of immersion in the simulated concrete pore solution are displayed in Figure 17. The Nyquist representation of the bare steel (Figure 17a) shows one capacitive loop that can be associated with the electrochemical activity at the steel/electrolyte interface. As seen from Figure 17a, the impedance gradually decrease overtime suggesting a continuous degradation of the carbon steel substrate by the chloride ions for the 615 sample. The 1055 coating showed large impedance values (10^{10} - $10^{11} \Omega \cdot \text{cm}^2$) and only one time constant during the first five days of immersion. This time constant is mainly related to the barrier properties of the epoxy primer. However, a second time constant at low frequency (~ 0.1 Hz) is clearly recognized after 10 days of immersion. This second time constant might be related to initiation of charge transfer processes that could be attributed to the zinc layer. Further studies need to be done to analyze this behavior. In terms of evolution, the impedance of the 1055 coating gradually decreases overtime, also suggesting a continuous degradation of the coating by the corrosive environment. The EIS spectra evolution of the galvanized coatings systems show a similar trend between them. During the first day of immersion, the EIS signal shows one-time constant that can be related to charge transfer processes between the galvanized coating and the electrolyte solution. After three days of immersion, the phase angle plots show the presence of two-time constants, the time constant at high frequency can be associated with the charge transfer process whereas the one at lower frequencies can be related to the formation of zinc corrosion products on the coated rebar. The majority of the galvanized coatings show an increased in impedance after few days of initial immersion, which is mainly attributed to the formation of zinc corrosion products that can provide an extra barrier protection against aggressive species. However, at longer immersion time, there is a decrease in impedance, suggesting that the chloride ions attack the corrosion products and reactivate the galvanized coating. The results show 30 days of immersion, the evolution in impedance for longer times marks the stability of stage 2, where the corrosion products are formed and form a thicker corrosion product more compact and less dense.



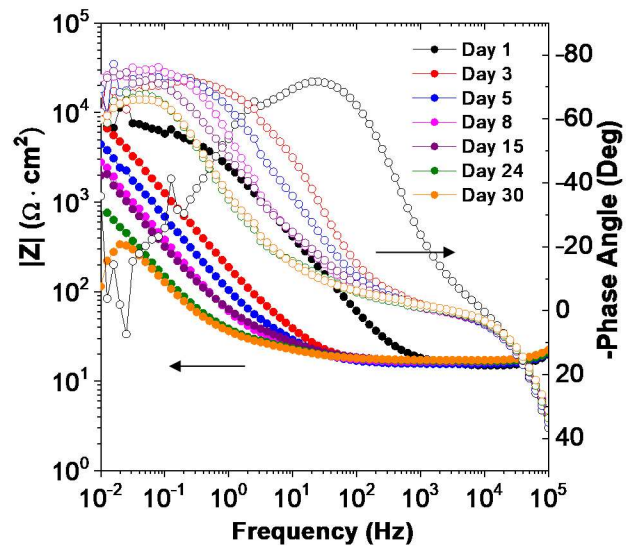
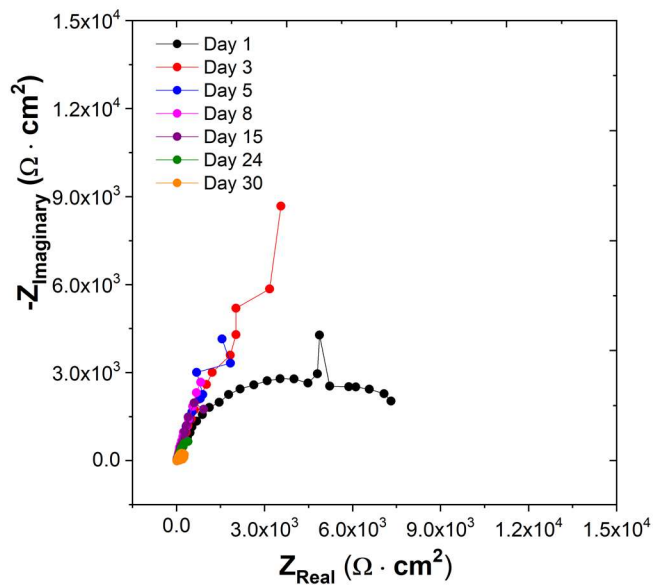
(a) 615 sample



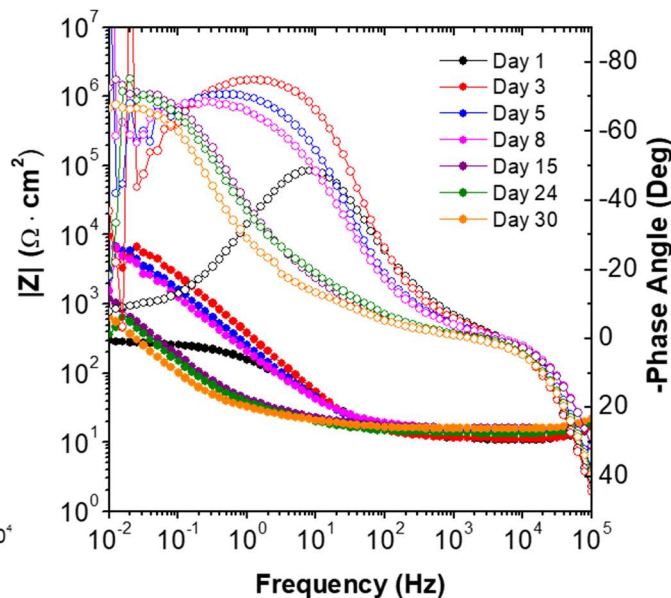
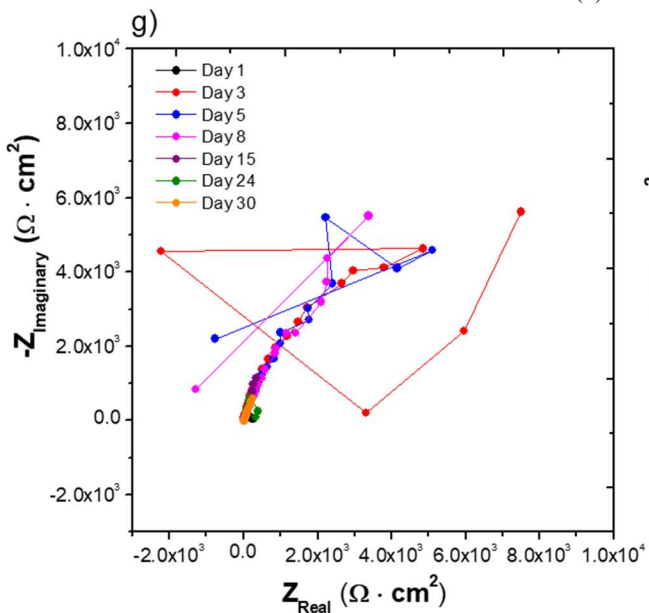
(b) 1055 sample



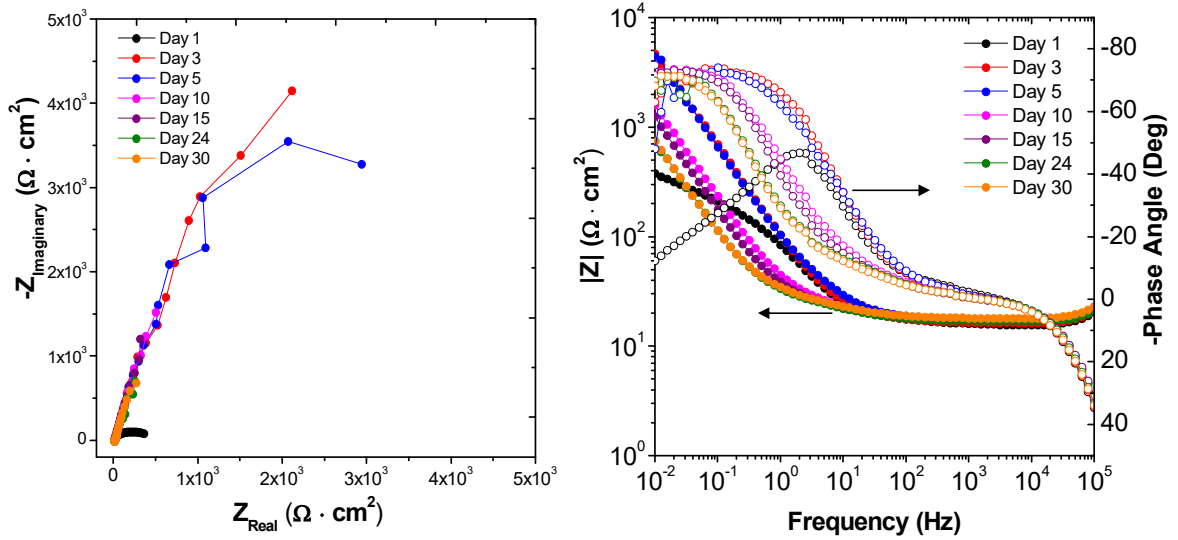
(c) 1094 sample



(d) 767 sample



(e) 1035 (CM-z)



(f) 1035 (CM-z)

Figure 17. EIS spectra of the rebar specimens immersed for 30 days in a simulated concrete pore solution: a) 615, b) 1055, c) 1094, d) 767, e) 1035 (CM-z), f) 1035 (CM-z).

4.5 Qualitative Index based on the laboratory testing and corrosion activity

Table 4 illustrates the qualitative index that considers the interfacial mechanisms occurring at the surface when different corrosion control systems are exposed to RC simulated chemical environment. The index is based on continuous monitoring of impedance magnitude. The chemical solution includes chloride ions, this latter assumes the environment exceeds the threshold magnitude needed to activate the surface of the rebar. The Rct parameter characterizes the dissolution reaction and is proportional to the corrosion rate or dissolution mechanism in the simulated conditions. The index was based on Rct parameter during different exposure times, 30 days and 360 days.

Table 4. Qualitative index based on electrochemical results for the corrosion control systems simulating corrosion environment and RC conditions.

Standard Description	ASTM A615 Carbon-Steel Rebar	ASTM A767 Hot Dipped Galvanized Rebar (HDGR)	ASTM A1094 Continuous Galvanized Rebar (CGR)	ASTM A1035 (9) Low-carbon Chromium (Chrom X + CGR)	ASTM A1055 Dual-Coated Rebar (CGR + Epoxy)
Industry Standard Performance Factors					
OCP (ASTM St)	-276 mV vs. SCE (90% risk of corrosion)	-600 mV vs. SCE (100-mV polarization development/decay)	-600 mV vs. SCE (100-mV polarization development/decay)	-600 mV vs. SCE (100-mV polarization development/decay)	Not Available
OCP Laboratory (for 30 days)	E (30 days) = -521.1 mV vs. SCE	E (30 days) = -925.6 mV vs. SCE	E (30 days) = -979.1 mV vs. SCE	E (30 days) = -899.8 mV vs. SCE	E (30 days) = -374.7 mV vs. SCE
EIS results for damage evolution at different times	$ Z _{0.01 \text{ Hz}} (30 \text{ days}) = 1104.6 \Omega \cdot \text{cm}^2$	$ Z _{0.01 \text{ Hz}} (30 \text{ days}) = 914 \Omega \cdot \text{cm}^2$	$ Z _{0.01 \text{ Hz}} (30 \text{ days}) = 3210.3 \Omega \cdot \text{cm}^2$	$ Z _{0.01 \text{ Hz}} (30 \text{ days}) = 3760 \Omega \cdot \text{cm}^2$	$ Z _{0.01 \text{ Hz}} (30 \text{ days}) = 3.17 \times 10^8 \Omega \cdot \text{cm}^2$
	$ Z _{0.01 \text{ Hz}} (360 \text{ days}) = 1327 \Omega \cdot \text{cm}^2$	$ Z _{0.01 \text{ Hz}} (360 \text{ days}) = 4064.0 \Omega \cdot \text{cm}^2$	$ Z _{0.01 \text{ Hz}} (360 \text{ days}) = 10008.0 \Omega \cdot \text{cm}^2$	$ Z _{0.01 \text{ Hz}} (360 \text{ days}) = 6234.9 \Omega \cdot \text{cm}^2$	$ Z _{0.01 \text{ Hz}} (360 \text{ days}) = 1.88 \times 10^7 \Omega \cdot \text{cm}^2$
Qualitative index based on EIS results Following 360 days based on stage	5	8.5	9	9	9.5

Task 2: Develop a reliability model for different corrosion prevention, control or mitigation conditions

Figure 2 shows the damage evolution of the RC elements and illustrates the corrosion mechanisms occurring at the interface between steel and the concrete. Different works have carried the characterization of the corrosion conditions without considering a local attack.

Pitting is a form of corrosion where localized loss of material occurs as opposed to a uniform loss. It is considered to be a more dangerous form because it is harder to detect and predict. In this section, we will use pitting corrosion models available in the literature to study the reliability of reinforced concrete bridge beams over time. A design space will first be established to provide results over a wide range of bridge configurations. For each of the configurations in the design space, the parameters known to affect corrosion will also be investigated.

4.5. Design Space

To evaluate localized or pitting corrosion, a design space used by Okeil et al. (23) to study shear reliability of reinforced concrete bridge beams strengthened in shear using fiber reinforced polymers (FRP) was selected to investigate the reliability levels over a wide range of bridge design scenarios. Three different bridge configurations with varying span lengths were chosen. A bridge cross section consisting of five reinforced concrete girders spaced at seven feet transversally from each other was assumed for all bridges. The cross section can be seen in Figure 18.

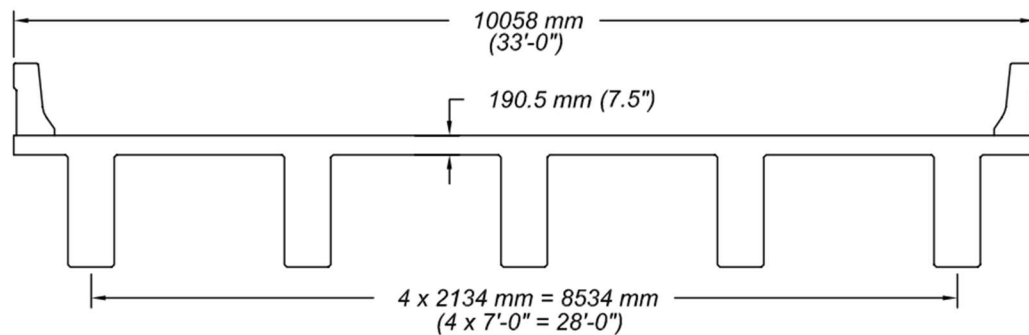


Figure 18. Details of typical bridge used to cover design space (23)

The span length for each considered bridge is 45 feet, 60 feet, and 75 feet. This study focused on one interior reinforced concrete girder from each bridge, as shown in Figure 19. The nominal flexural demands for the selected beams were calculated following AASHTO LRFD Bridge Design Specifications (2017) and can be found in Table 5 through Table 7. More details on these design spaces can be found elsewhere in Okeil et al. 2013 (24).

Table 5. Moment loads for design space 1.

M_D/M_L	M_D (kN.m.)	M_L (kN.m.)	M_n (kN.m.)	M_u (kN.m.)
0.5	1245	2490	6572	5914
0.75	1651	2201		
1	1971	1971		
1.25	2232	1785		
1.5	2447	1632		
1.75	2629	1502		
2	2783	1392		
2.25	2917	1296		
2.5	3033	1213		
2.75	3135	1140		
3	3226	1075		

Table 6. Moment loads for design space 2.

M_D/M_L	M_D (kN.m.)	M_L (kN.m.)	M_n (kN.m.)	M_u (kN.m.)
0.5	736.0	1472	3885	3496
0.75	975.7	1301		
1	1165	1165		
1.25	1319	1055		
1.5	1447	964.5		
1.75	1554	887.9		
2	1645	822.6		
2.25	1724	766.3		
2.5	1793	717.2		
2.75	1853	674.0		
3	1907	635.7		

Table 7. Moment loads for design space 3.

M_D/M_L	M_D (kN.m.)	M_L (kN.m.)	M_n (kN.m.)	M_u (kN.m.)
0.5	431.7	863.4	2278	2051
0.75	572.3	763.0		
1	683.5	683.5		
1.25	773.8	619.0		
1.5	848.5	565.7		
1.75	911.4	520.8		
2	965.0	482.5		
2.25	1011	449.4		
2.5	1052	420.6		
2.75	1087	395.3		
3	1118	372.8		

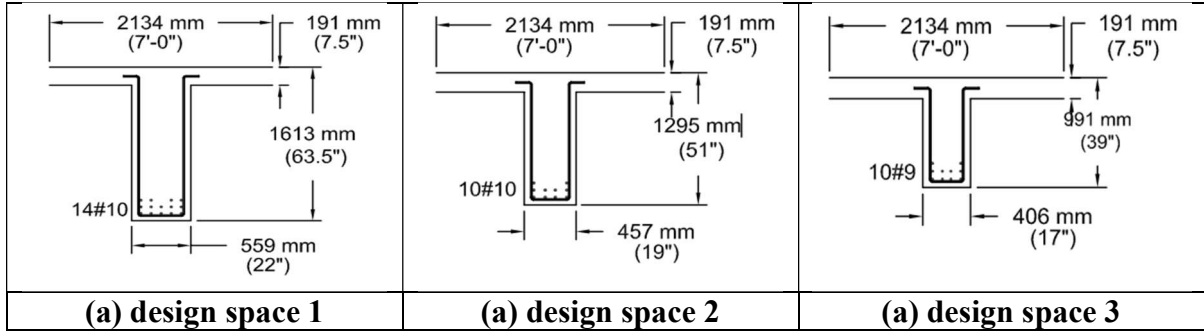


Figure 19. Typical girder details (Okeil et al, 23)

4.6. Modeling of Time to Corrosion Initiation

The diffusion coefficient is dependent on conditions such as concrete material properties, water to cement ratio, and exposure conditions. However, Castaneda et al. (31) shifted focus on developing an effective, probabilistic model using the least number of parameters based on model selection criteria for developing the diffusion coefficient in a manner where it would not be a deterministic constant value. Bayesian methodology was utilized within the evidence-based models using experimental data. The impacts of each parameter including material properties, environmental conditions, and the structural geometries were investigated considering the uncertainties within the system. A statistical approach was added utilizing Bayesian updating technique to decide the model parameters. The model parameters, θ_1 , θ_2 , and θ_3 , were estimated by the maximization function that maximizes the concentration profile likelihood when previous reference case data set was given. Still using Fick's law (38), Equations 1 and 2 were established by Castaneda et al. (31).

$$C(x, t) = C_s \left(1 - \operatorname{erf} \frac{x}{2\sqrt{Dt}} \right) \quad [1]$$

$$D(t) = \theta_1 (\theta_3 / t)^{\theta_2} \quad [2]$$

where:

- $C(x, t)$ = Chloride concentration (% mass),
- C_s = Chloride concentration on concrete surface (% mass),
- x = Distance from surface (mm),
- D = Chloride diffusivity (mm^2/month),
- t = Time (month), and
- $\theta_1, \theta_2, \theta_3$ = Parameters in the diffusion model

Table 8 displays the consequent statistics of the parameters for the chloride diffusion model using the reference case of $w/c = 0.46$ and 7 days of curing, based on the diffusion equation without the correction factor. Sigma, σ , represents the model error. The correlation coefficient shows the parameters' correlation with one another. In this case, θ_2 and θ_3 shows relatively higher correlation compared to other parameters' correlation, which means that those two parameters are possibly merged to increase the equation efficiency, but there is also other possibility that such a merging process increases the model uncertainty. It was observed that the model has low statistical uncertainty as is evident by the generally low standard deviation values.

Table 8. Chloride diffusion model parameters and statistics

	Mean	Std. Dev.	Correlation Coefficient		
			θ_1	θ_2	θ_3
θ_1	500	1	1	0.013	-0.213
θ_2	30	1.13	0.013	1	-0.26
θ_3	0.56	0.027	-0.213	-0.26	1
σ	0.342	0.019	0.019	-0.336	0.044

In order to express the different concrete conditions compared to the reference case, the correction factors, α_1 and α_2 , from Table 9 and Table 10 were added on the diffusivity equation. The correction factor helped improve the model fit to the given data set, and reflects the trend that may not be observed in the posterior statistics with reference case. The factors, α_1 and α_2 , represent a water to cement ratio correction factor and curing day correction factor, respectively.

Table 9. Water to cement ratio correction factor.

w/c Correction Factor, α_1			
w/c Ratio	Distribution	α_1 Mean	α_1 Std. Dev.
0.46	Normal	1	0.4
0.5	Normal	1.719	0.576
0.53	Normal	2.283	0.673
0.7	Normal	2.678	--
0.76	Normal	2.783	0.984

Table 10. Curing day correction factor.

Curing Days Correction Factor, α_2			
C_d Model	Distribution	α_2 Mean	α_2 Std. Dev.
1	Normal	1.265	0.221
3	Normal	0.716	0.073
7	Normal	0.875	0.09

Using these correction factors and model parameters, Castaneda et al. (31) probabilistically generated the following time to corrosion initiation Equation 3

$$T_{corr} = \left[\frac{c^2}{4(\alpha_1 \theta_1 (\theta_2)^{\theta_3})} \left[\text{erf}^{-1} \left(1 - \frac{C_{th}}{C_s} \right) \right]^{-2} \right]^{1/(1-\theta_3)} \quad [3]$$

As previously stated, there is no known single, precise value for the chloride threshold value. Therefore, the experimental work of Castro-Borges et al. (32) involving polarization resistance techniques provided interpolated chloride threshold values at five respective water to cement ratios for Castaneda et al. (31), which will be the assumed critical chloride values herein. These values are provided in Table 11.

Table 11. Interpolated chloride threshold values

Water to Cement Ratio, w/c	Interpolated Chloride Threshold Value, C_{th} (% per weight of concrete)
0.46	0.1120
0.50	0.1447
0.53	0.1265
0.70	0.06797
0.76	0.0586

4.7. Modeling of Pitting corrosion

Several researchers investigated pitting corrosion of steel reinforcement in concrete structures. For example, Tutti (1) and Gonzalez et al. (36) modeled pitting corrosion within chloride-contaminated structures. The maximum pit depth, P_{max} , was found to exceed the penetration calculated based on general corrosion, P_{av} Stewart (41). However, there is a significant uncertainty associated with the ratio between these two values. Gonzalez et al. (36) findings show that the maximum ratio of maximum pit depth to penetration of general corrosion, R , varies from 4 to 8 in concrete specimens exposed to natural environments. These results are generally in agreement with Tutti (1) who suggested that the ratio usually falls within a range of 4 to 10. Darmawan and Stewart (41) suggested the distribution of maximum pit depths for prestressing wires is best represented by the Gumbel (Extreme Value-Type I) distribution, which has been widely used to characterize other pitting corrosion scenarios such as that in steel plates and pipes as well as prestressing strands. Stewart (2004) agreed that it is, therefore, reasonable that the Gumbel distribution be appropriate for modeling maximum pit depths of reinforcing bars.

A popular approach in modeling pit depth using extreme value theory originates from Turnbull (42). The ratio of maximum pit depth to average penetration from general corrosion, R , is treated as a random variable modeled by the Gumbel distribution using Equation 4. This random variable is also referred to as the pitting factor.

$$F(R) = e^{-e^{-(R-\mu)/\alpha}} \quad [4]$$

where:

μ = Location parameter

α = Scale parameter

The location and scale parameters characterize the shape of the distribution, which is an indication of the dispersion of the data. Stewart (41) suggested that these parameters can be determined from the results of Gonzalez et al. (36). For an 8-millimeter bar, $R=4$ and $R=8$ represent the 5th and 95th percentiles of the distribution, respectively. Accordingly, the mean and coefficient of variation are found to be 5.65 and 0.22, which translate into the parameters of the Gumbel distribution $\mu_0=5.08$ and $\alpha_0=1.02$. Turnbull (42). suggests that for a reinforcing bar with different dimensions, the Gumbel distribution parameters can be determined using Equations 5 and 6. The mean and standard deviation are related to these parameters by Equations 7 and 8.

$$\mu = \mu_0 + \frac{1}{\alpha_0} \ln\left(\frac{A}{A_0}\right) \quad [5]$$

$$\alpha = \alpha_0 \quad [6]$$

where:

A = surface area of the respective bar

A_0 = surface area of an 8mm diameter bar of 125 mm length

$$\mu_X \approx \mu + \frac{0.5772}{\alpha} \quad [7]$$

$$\sigma_X \approx \frac{1.282}{\alpha} \quad [8]$$

After the statistical descriptors of the pitting factor random variable, R , the maximum pit depth along a reinforcing bar can be evaluated using Equation 9.

$$P(T) = 0.0116 * i_{corr}(T) * R * T \quad [9]$$

This equation considers Faraday's law where a unit current density induces a uniform corrosion penetration of 11.6 micrometers per year (36). A model to predict the loss of the cross-sectional area of a reinforcing bar due to pitting has been proposed by Val and Melchers (44). The pit configurations, as seen in Figure 20 and Figure 21, the width of the pit, and cross-sectional area of the pit can be expressed using Equations 10-15.

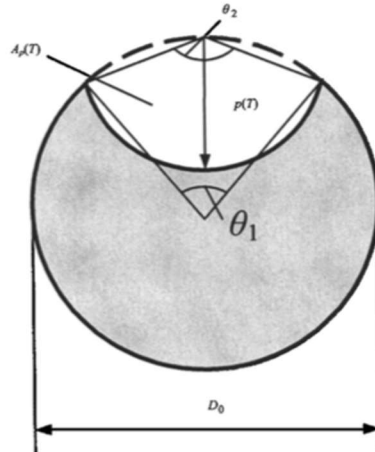


Figure 20. Pit configuration (43).

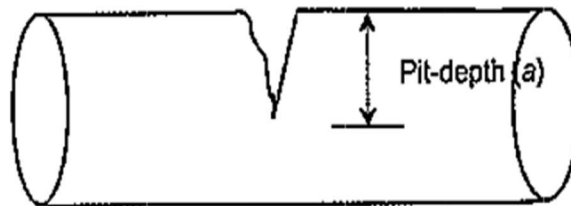


Figure 21. Pit configuration (34).

$$b = 2 * P(T) * \sqrt{1 - \left(\frac{P(T)}{D_0}\right)^2} \quad [10]$$

$$A_1 = 0.5 \left[\theta_1 \left(\frac{D_0}{2} \right)^2 - b \left| \frac{D_0}{2} - \frac{P(T)^2}{D_0} \right| \right] \quad [11]$$

$$A_2 = 0.5 \left[\theta_2 * P(T)^2 - b \frac{P(T)^2}{D_0} \right] \quad [12]$$

$$\theta_1 = 2 \arcsin \left(\frac{b}{D_0} \right) \quad [13]$$

$$\theta_2 = 2 \arcsin \left(\frac{b}{2P(T)} \right) \quad [14]$$

$$A_{pit}(T) = \begin{cases} A_1 + A_2 & P(T) \leq \frac{D_0}{\sqrt{2}} \\ A_s - A_1 + A_2 & \frac{D_0}{\sqrt{2}} < P(T) \leq D_0 \\ A_s & P(T) > D_0 \end{cases} \quad [15]$$

Using the residual area for pitting corrosion from Equation 16, the flexural limit state function formed for the reliability analysis of each design space is molded from basic bending theory.

$$A_s(T) = n \left(\frac{\pi D_0^2}{4} - A_{pit} \right) \geq 0 \quad [16]$$

where:

D_0 is the nominal diameter of the reinforcing bar.

The nominal flexural strength, M_n , is estimated from reinforced concrete basic principles, which leads to Equation 17 for certain cross section width, b , effective depth, d , concrete compressive strength, f'_c , and steel yield stress, f_y . The depth of the equivalent compression stress block, a , can be found from equilibrium using Equation 18. It can be seen that the area of steel rebars directly affects the flexural resistance of reinforced concrete sections.

$$M_n = A_s * f_y * \left[d - \frac{a}{2} \right] \quad [17]$$

$$a = \frac{A_s * f_y}{0.85 * b * f'_c} \quad [18]$$

The limit state function for flexural capacity is generally conveyed as the ultimate flexural moment due to external loads, M_u , subtracted from the nominal moment flexural resistance as seen in Equation 19.

$$g(M) = M_n - M_u \quad [19]$$

With this relationship, a probabilistic model, Equation 20, developed by Ghanooni-Bagha et al. (15) was used as the limit state function for evaluation of each design space.

$$g(M) = ME_m * A_s(T) * f_y(T) * \left[d - K * \frac{A_s * f_y(T)}{b * f'_c} \right] - M_u \quad [20]$$

where:

ME_m = flexural model uncertainty coefficient

$A_s(T)$ = residual area of steel reinforcement (m^2)

$f_y(T)$ = residual yielding steel strength of steel reinforcement (N/m^2)

- d = effective depth of cross section (cm)
 A_s = initial area of steel reinforcement (m²)
 b = width of cross section (m)
 f'_c = compressive strength of concrete (N/m²)

Accounting for stress concentrations due to pitting, the residual steel yield stress is computed using Equation 21.

$$f_y(T) = \left(1 - \alpha * \frac{A_s - A_s(T)}{A_s}\right) * f_y \quad [21]$$

where:

- α = yielding strength uncertainty coefficient
 f_y = initial yielding strength of steel reinforcement (N/m²)

The ultimate flexural moment was estimated using the conceptual nature of reinforced concrete and stated by AASHTO LRFD (30) in Equations 17 and 22. For a T-beam, as those in each design space of note within this research, if the neutral axis is assumed to fall within the flange of the beam, the value of the 'a' can be computed similarly using equilibrium equations. According to Equation 22, a resistance factor is applied to the nominal moment in order to find the ultimate moment capacity (AASHTO LRFD, 30).

$$\phi_f M_n \geq M_u \quad [22]$$

where:

ϕ_f = flexure resistance factor

From AASHTO LRFD (30), the ultimate moment could be further broken down into a general design equation portraying the effects of both dead and live loads. The general AASHTO LRFD design equation, Equation 23 displays how loads, distribution factors, and ultimate resistance correspond to the strength limit state.

$$\eta_i(\gamma_D Q_D + \gamma_L Q_L) \leq R_r \quad [23]$$

where:

- n_i = load modifier, relating to ductility, redundancy, and operational importance
 γ_D = dead load factor
 γ_L = live load factor
 R_n = nominal resistance
 R_r = factored resistance ϕR_n

The modifiers and distribution factors taken from AASHTO LRFD (30) for a bridge evaluated for flexure are displayed in Table 12.

Table 12. Load modifiers and factors for LRFD design equation.

n_i	1.00
γ_D	1.25

γ_L	1.75
ϕ	0.90

Furthermore, eleven dead to live load ratios, ranging from 0.5 to 3.0, are considered in evaluating the reliability of the corroded structure to investigate the consequences of more demanding dead load scenarios. Derived from Equation 23, the design equation (Equation 24) and the limit state function (Equation 25) will be used in this study.

$$\sum \eta_i * \gamma_D * M_D + \sum \eta_i * \gamma_L * M_L \leq \phi * M_n = M_u \quad [24]$$

$$g(M) = ME_m * A_s(T) * f_y * \left[d - K * \frac{A_s * f_y(T)}{b * f'_c} \right] - (M_D + M_L) \quad [25]$$

4.8. Reliability Analysis

MATLAB was selected as the computation environment for this study since it allows for the basic functions required for assessing the structural reliability of a structure. In particular, symbolic computing allows solving for the reliability index, β , in highly nonlinear limit state functions with ease. Random variables established by Castaneda et al. (31) were implemented into the MATLAB software in order to identify the time to corrosion initiation at chloride surface concentrations for each design space using different parameters, such as concrete cover and water to cement ratio, using Equation 3.

Similarly, more complex scripts were implemented MATLAB to evaluate the pitting corrosion propagation period of each design space. The random variables for the pitting corrosion phase were obtained for the literature as described in the previous section. Using the the Symbolic Math Toolbox within the MATLAB, the First Order Reliability Method (FORM) was implemented by perform differentiation, integration, simplification, transforms, and equation solving. The resistance of the limit state function decreases with time as a result of the reduction in the steel reinforcement area as well as its yielding strength. The aforementioned definitions of residual area will show that this parameter is affected by the diameter loss of steel reinforcement for the pitting area of steel reinforcement for pitting corrosion. The pitting area is a function of the corrosion current density with respect to time, $i_{corr}(T)$. Vu and Stewart 2000 suggested the following equation for $i_{corr}(T)$.

$$i_{corr}(T) = \begin{cases} i_{corr}(1) & 0 \leq T \leq 1 \text{ year} \\ 0.85 * i_{corr}(1) * T^{-0.29} & T > 1 \text{ year} \end{cases} \quad [26]$$

where:

$$i_{corr}(1) = \text{One-year corrosion rate at the start of corrosion propagation} \left(\frac{\mu A}{cm^2} \right)$$

Dai and Wang (2009) proposed the following equation for estimating the one-year corrosion rate as a function of the water to cement ratio and the cover of reinforcement.

$$i_{corr}(1) = \frac{37.8(1-WC)^{-1.64}}{c} \quad [27]$$

Therefore, the effects of three varying concrete covers and three water to cement ratios were investigated with respect to each design space at varying dead to live load ratios for both general and pitting corrosion. In total, 54 cases were analyzed for this study evaluating three different concrete covers at three water to cement ratios for all three design spaces under both uniform and pitting corrosion cases. In the next section, results for each case are depicted. In order to easily represent each case, designations for each scenario are given in order to relay which parameters the case describes. These parameters include: water to cement ratio (WC), cover (C), and surface chloride content (Cl). For example, when analyzing design space 2 at a water to cement ratio of 0.46 with a concrete cover of 13 centimeters and chloride surface concentration of 0.3%, the designation will read “Design space 2 WC46C13Cl30”.

Table 13 displays the statistical characteristics of random variables within the limit state function, both uncertainty variables and variables influencing mechanical features, for each design space.

Table 13. Statistical characteristics of random variables for each design space.

Parameter	Mean	Bias	COV	Distribution
f'_c (MPa)	27.6	1.156	0.18	Log-normal
f_y (MPa)	414	1.145	0.10	Log-normal
Dead Load (N.m.)	varies	1.05	0.10	Normal
Live Load (N.m.)	varies	1.35	0.6	Normal
d	varies	1.0	0.02	Normal
Concrete Cover (cm)	varies	1.0	0.12	Normal

Based on the parameters determined so far, it was possible to estimate the corrosion initiation time for the different w/c ratios based on the T_{corr} equation that estimates the time to the corrosion initiation using the previously estimated statistical. As expected, at the same level of surface chloride concentration, the corrosion was expected to initiate earlier at concrete with higher w/c ratios. One exception case that did not follow the general corrosion initiation time trend was $w/c = 0.46$, and it is guessed that the sample may not be cured well, so it might had much higher permeability than any other samples, which occurs much lower chloride threshold value that triggers corrosion initiation earlier than $w/c = 0.5$ and 0.53 under certain surface chloride concentration range.

$$T_{corr} = \left[\frac{d_c^2}{4(\alpha_1\theta_1(\theta_2)\theta_3)} \left[erf^{-1} \left(1 - \frac{C_{cr}}{C_s} \right) \right]^{-2} \right]^{1/(1-\theta_3)} \quad [28]$$

The critical surface chloride concentration of each w/c ratio was observed that divide each curve into two phases. For example, the $w/c = 0.76$ or 0.7 cases, the T_{corr}/C_s value changes significantly around the surface concentration of 0.08 or 0.09, respectively. So, the surface concentration lower than the critical value showed much longer average time period for corrosion initiation even with the much higher changing rate compared to the case of the surface concentration exceeds 0.07. There was also a trend of this critical surface chloride concentration throughout the w/c ratio, which was also generally increased with it, and such this trend is consistent with the trend between T_{corr} and w/c ratio.

The pitting factor is derived using the cumulative density function and its respective probability density function from Equation 4. The developed script calculates the location parameters of these functions across a region of values, which are then used to provide information into Equation 9 for the maximum pit depth regarding instances of pitting corrosion. Similar to time to corrosion

initiation, the pitting factor is modeled by Gumbel distribution. For conservative purposes, the location parameter of the pitting factor for each design space was assumed at a 50% value of the PDF. With an assumed location parameter, the mean value of the pitting factor was found using Equation 7. The PDF of the location scale parameter and its correlated value of pitting factors from each design space are seen in Figure 22 and Table 14.

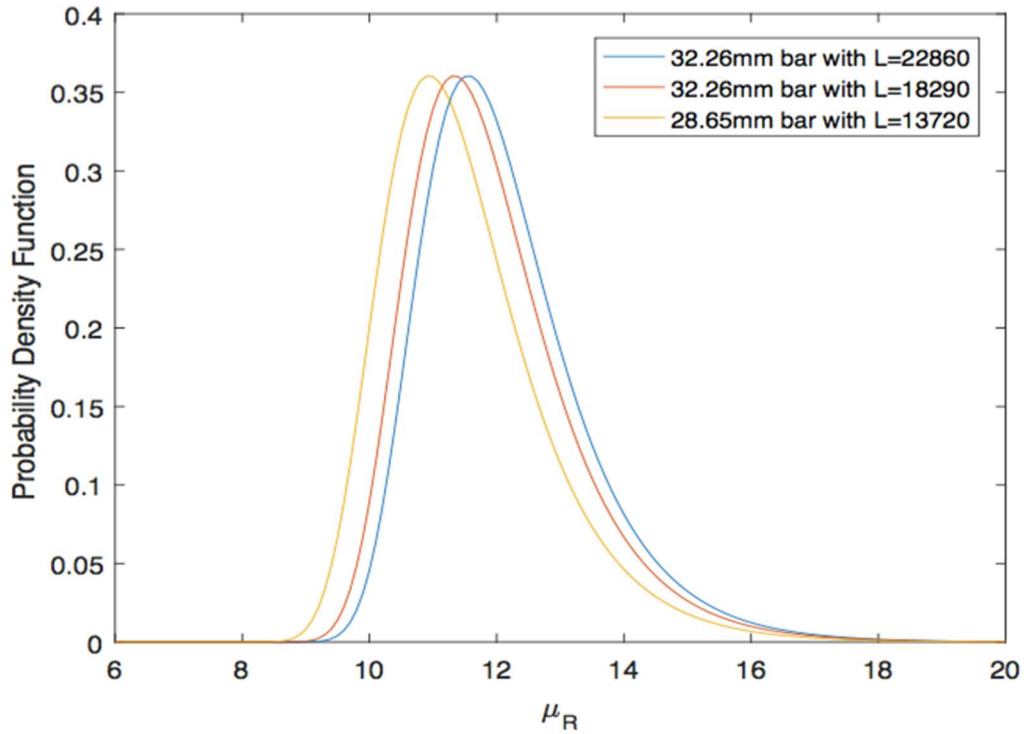


Figure 22. PDF vs. Location Parameter of Pitting Factor.

Table 14. Pitting factor for each design space.

Design Space	Pitting Factor, R	Standard Deviation, σ_R
1	12.1196	1.2569
2	11.9010	
3	11.5028	

4.9. Sample Results

Scenarios of pitting corrosion were studied to analyze more extreme corrosion situations resulting in higher pitting depths and less residual area over time, which can be seen in Figure 23 through Figure 28. Similar to the situations of general corrosion during the corrosion initiation period, the reliability index initially falls around 4 to 4.5 for each evaluated setting at each design space before the reinforcement starts corroding and still has all of its steel area. The concrete cover and water to cement ratio are all the important parameters in these occasions of corrosion since, unlike general corrosion, the corrosion rate accelerates over time, catalyzing expedited losses of steel reinforcement with each successive year. This is evident in Figure 23 through Figure 28 for Design Space 1 considering varying concrete cover values and Design Space 2 considering varying w/c

ratios. The rapid decrease of residual area lowers the likelihood that there will be enough flexural strength resisting the flexural stresses.

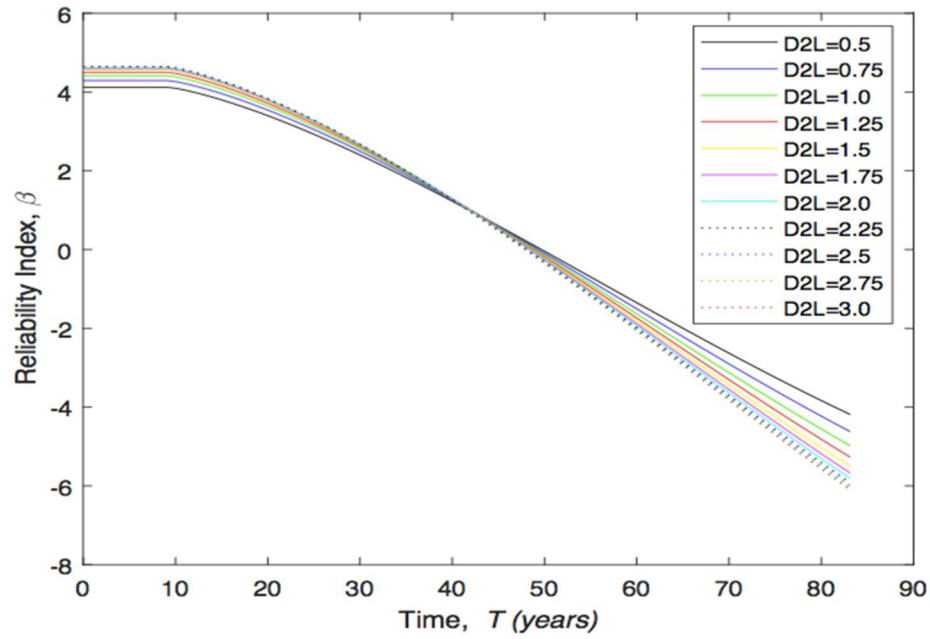


Figure 23. Reliability Index vs. Time design space 1 WC46C12C135.

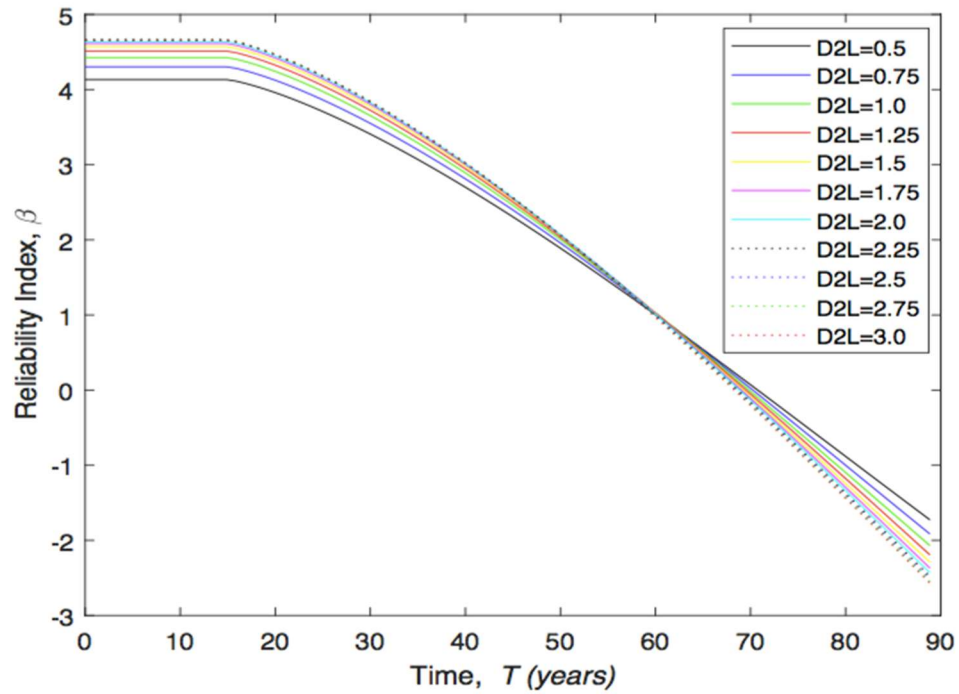


Figure 24. Reliability Index vs. Time design space 1 WC46C15C135.

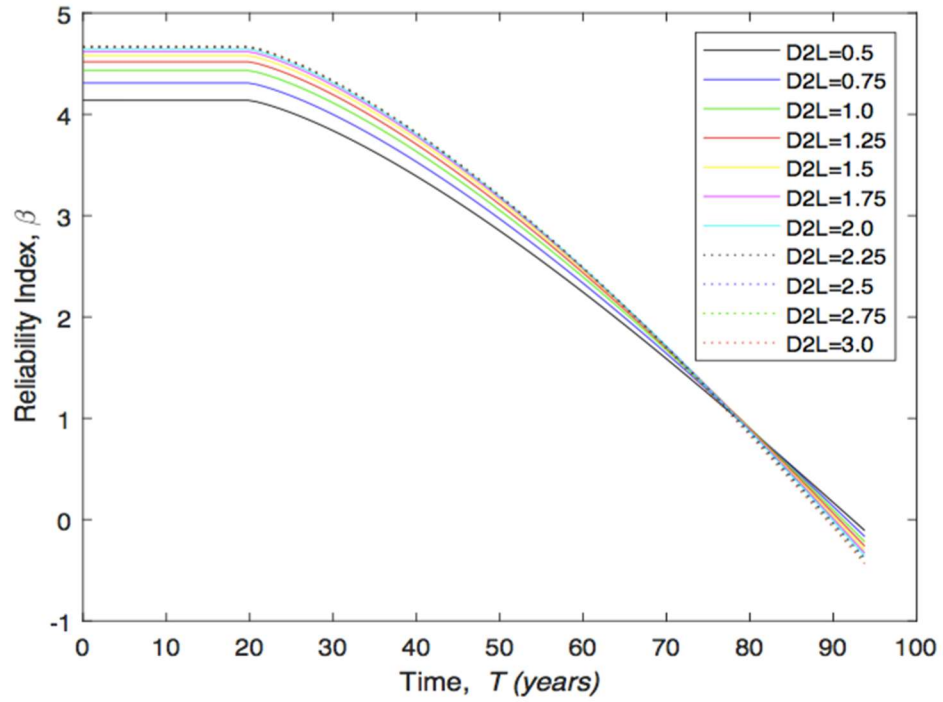


Figure 25. Reliability Index vs. Time design space 1 cover WC46C18C135.

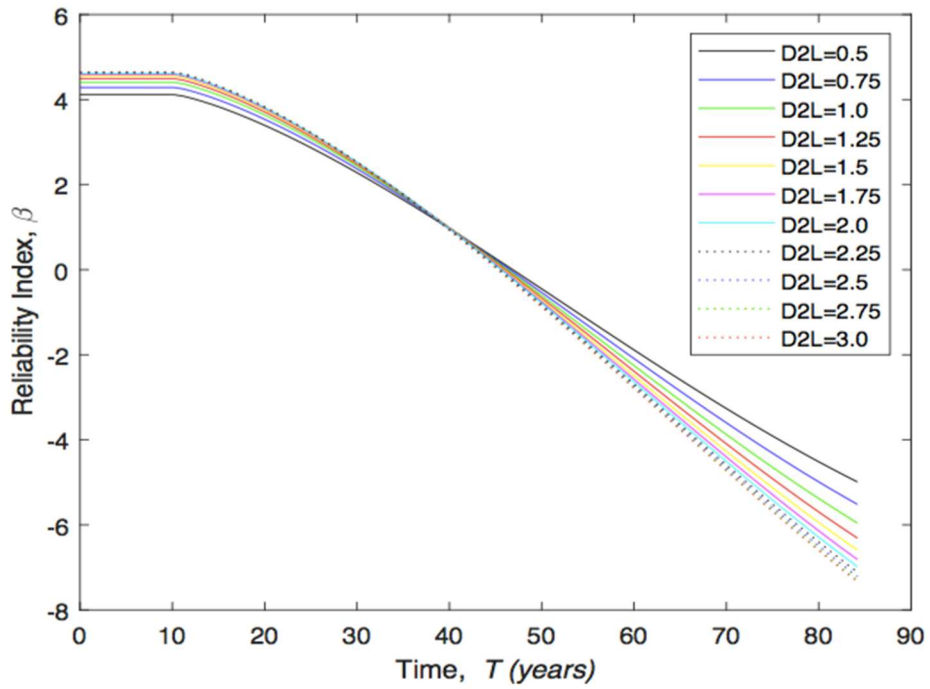


Figure 26. Reliability Index vs. Time design space 2 WC46C11C130.

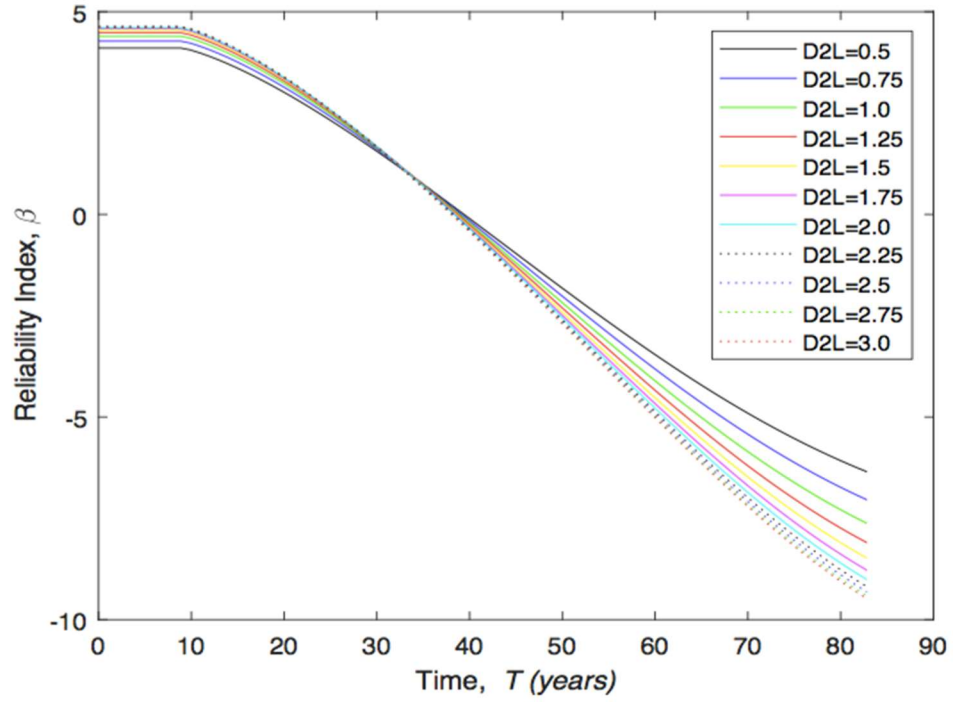


Figure 27. Reliability Index vs. Time design space 2 WC50C11C130.

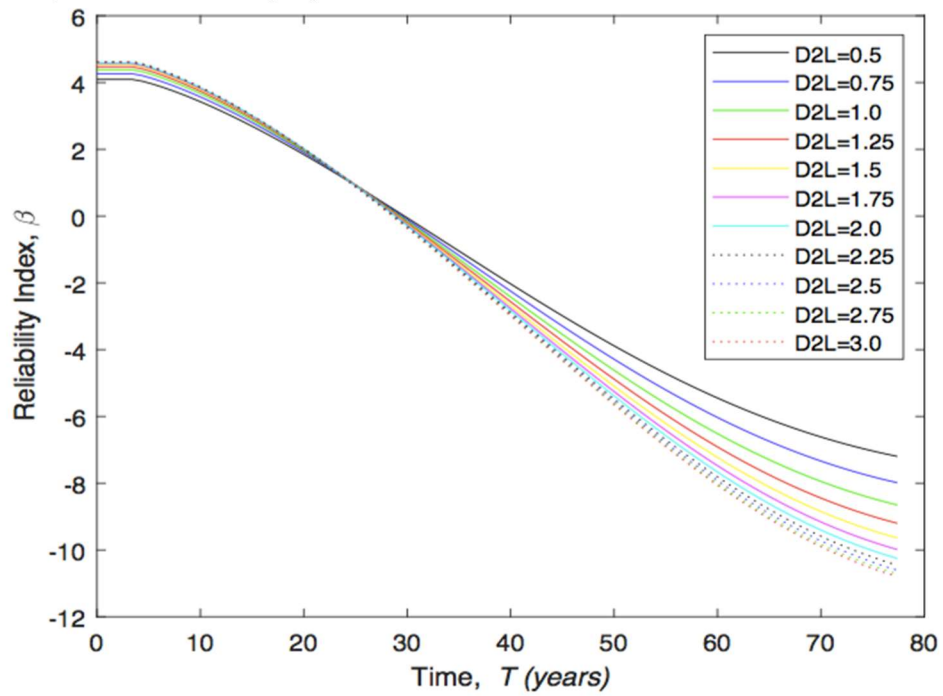


Figure 28. Reliability Index vs. Time design space 2 WC53C.

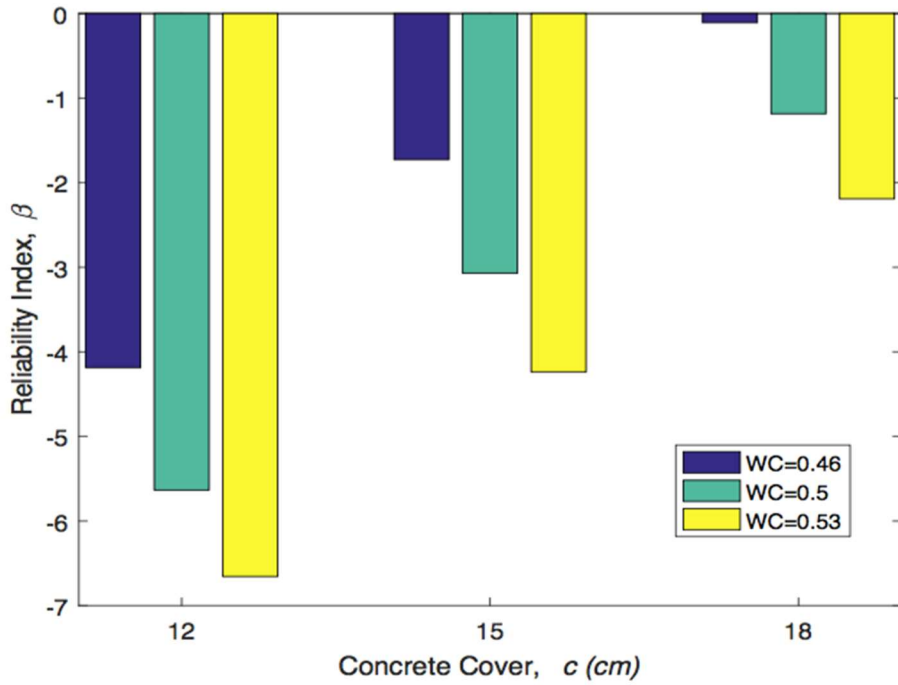


Figure 29. Reliability Index vs. Concrete Cover design space 1 at T=75 years.

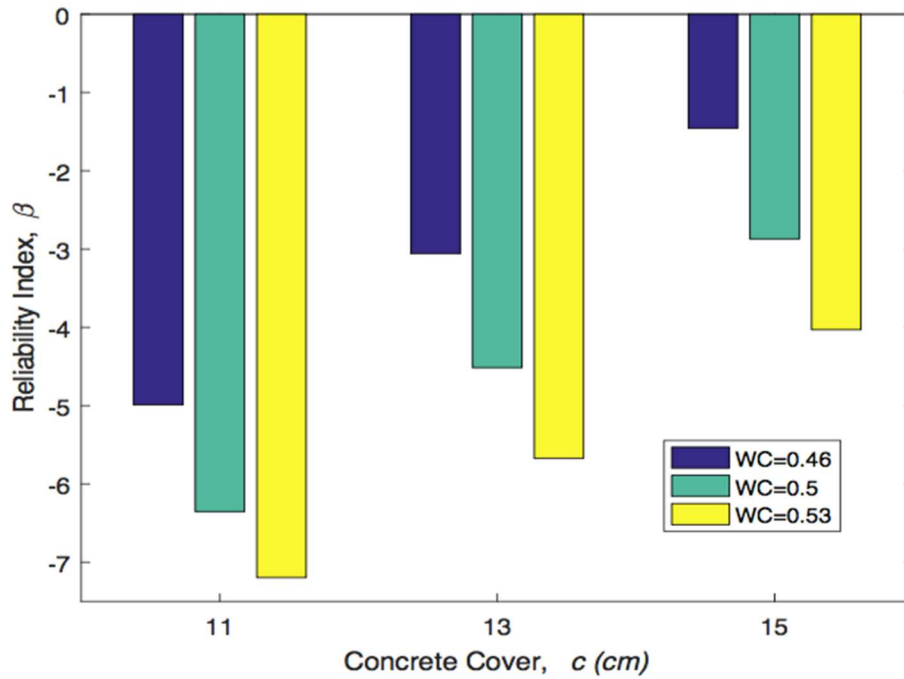


Figure 30. Reliability Index vs. Concrete Cover design space 2 at T=75 years.

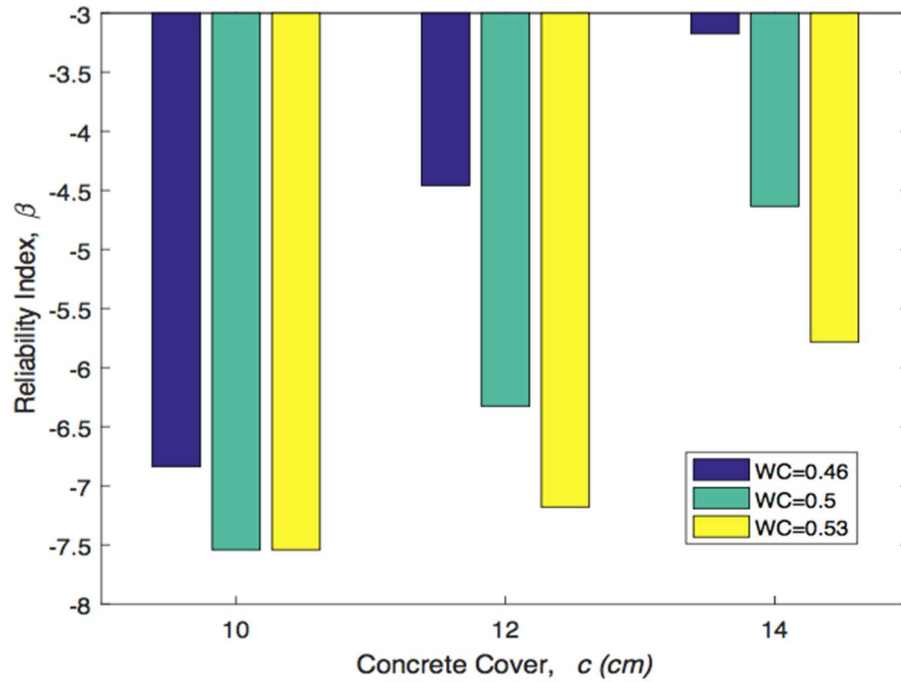


Figure 31. Reliability Index vs. Concrete Cover design space 3 at $T=75$ years.

In all the analysed cases, twenty-seven cases display a reliability index below -1, correlating to a probability of failure of about 85% probability of failure, after only $T=50$ years after the conclusion of corrosion initiation. Furthermore, twenty-four of the twenty-seven evaluations portray a probability of failure of at least 95% after $T=75$ years of propagation. Figure 29 through Figure 31 summarizes these results at $T=75$ years for different concrete cover values and w/c ratios.

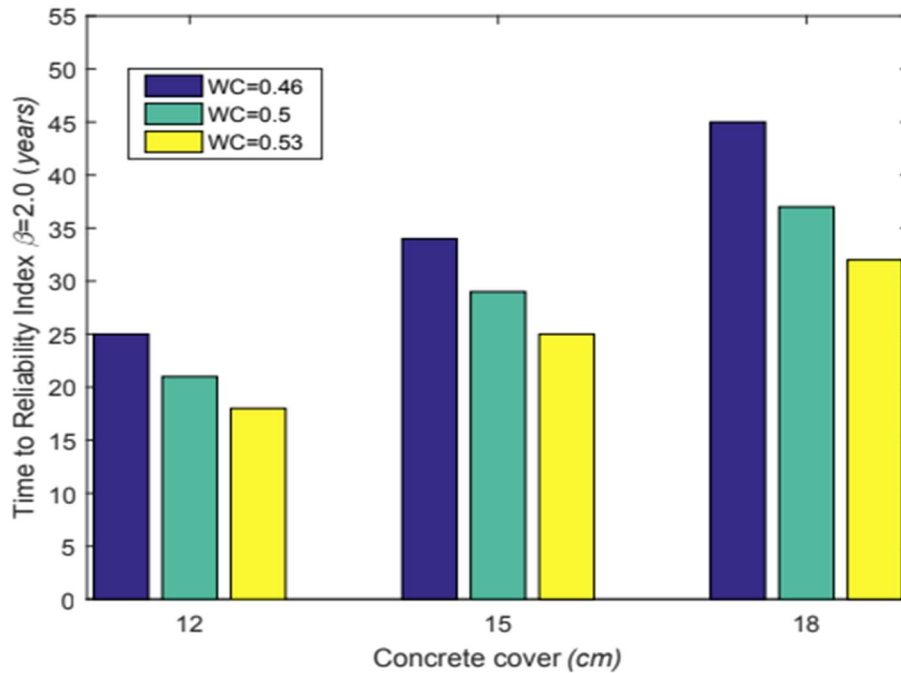


Figure 32. Time to Reliability Index Threshold design space 1.

The results can be used to estimate the time at which minimum allowable threshold reliability index is considered. If this threshold is set to 2.0 at which intervention becomes necessary, the results in Figure 32 through Figure 34 can be obtained. In the figures, the time, from the conclusion of corrosion initiation to the time of exceeding the allowable reliability threshold, is shown for each pitting corrosion design scenario. It can be seen that the design life considered in AASHTO of 75 years is not achieved for any of these scenarios. This calls for mitigation strategies by using corrosion inhibitors that can slow the rate of corrosion.

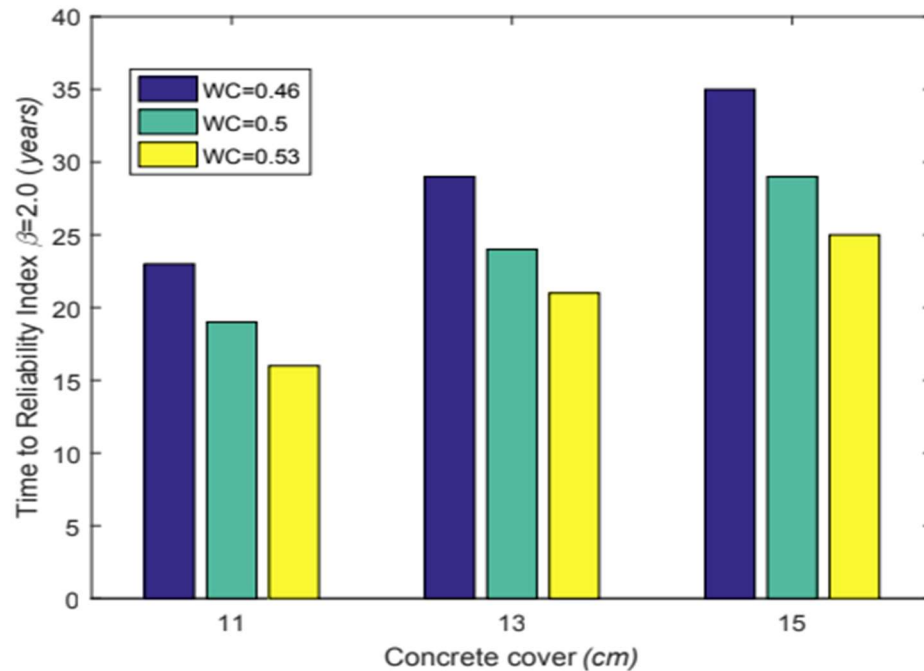


Figure 33. Time to Reliability Index Threshold design space 2.

The ultimate goal of the reliability study to translate the corrosion modeling information into useful decision-making tools for transportation asset owners. For example, a comparison between different mitigation strategies that affect the rate of corrosion propagation can be introduced. As can be seen in Figure 25, the reliability of a deficient structure is assumed to be investigated under three alternative repair methods. Two repair alternatives, Repair #1 and Repair #2, restore the reliability index to its initial value before corrosion damage. The difference between these two methods is that Repair #1 does little to reduce the rate of corrosion, which results in a service life of slightly over 50 years. Conversely, Repair #2 slows the degradation rate, which results in a service life of about 60 years. Reducing the degradation rate can be achieved using different methods. For example, Fiber Reinforced Polymer wrapping of RC beams is known to deprive the corrosion cell of oxygen, which results in slower corrosion rates.

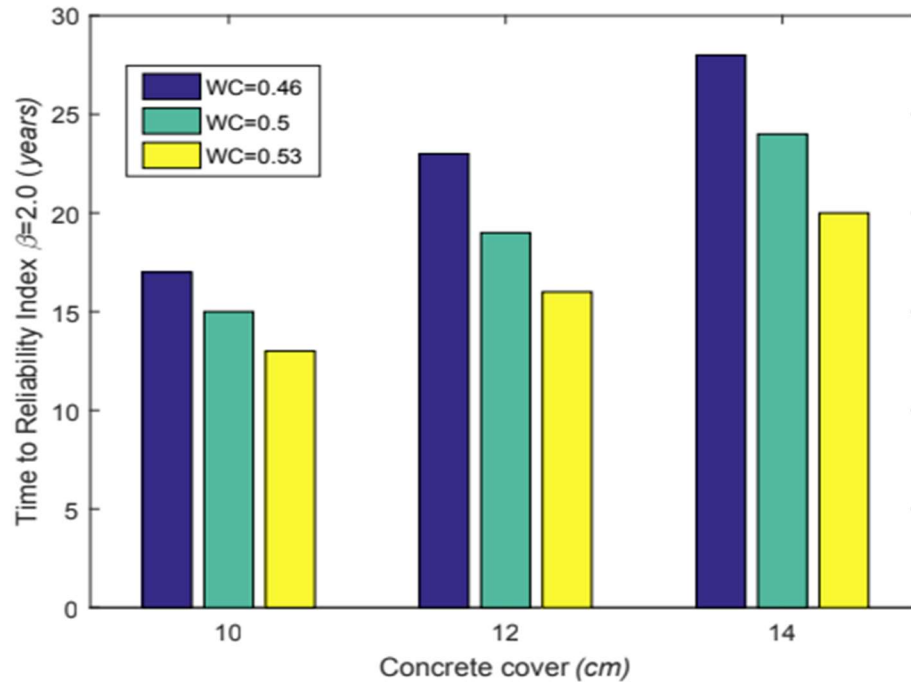


Figure 34. Time to Reliability Index Threshold design space 3.

Nevertheless, the achieved service is still below what an owner may be interested in, e.g., 75 years. To achieve a longer design life, Figure 40 shows that a higher initial reliability index, β , will be needed for the same corrosion rate as that resulting from Repair #2. This is the case for Repair #3, for which the initial β after repair is increased, which adds about 5 years of service life over Repair #2 alternative.

4.10. Concrete specimens with different rebar coatings (organic and inorganic)

In order to simulate the full damage evolution stages and characterize the corrosion mechanisms with different rebar samples and corrosion control protection conditions.

The ratio of the constituents used to cast the samples was 1:1.5:2:0.53 (concrete: sand: aggregates: water ratio) with the dimensions of the cast concrete being 4x4x4 in³. Dams were then fitted over the concrete and filled with solution with the sample set-up shown in Figure 35 The samples were tested once a week to obtain open circuit potential (OCP) and electrochemical impedance spectroscopy (EIS) results. The obtained results have been reported in

Figure 36-Figure 47. The rebars tested were 615 steel, galvanized 1035 (CS-M), 1035 (CM-z), 1094, 767 and epoxy + galvanized dual coated 1055.

They were tested in 0% NaCl, 1% NaCl and 3.5% NaCl solutions to study the effect of chloride concentration on the corrosion rates and the time taken for the solution to reach the sample.

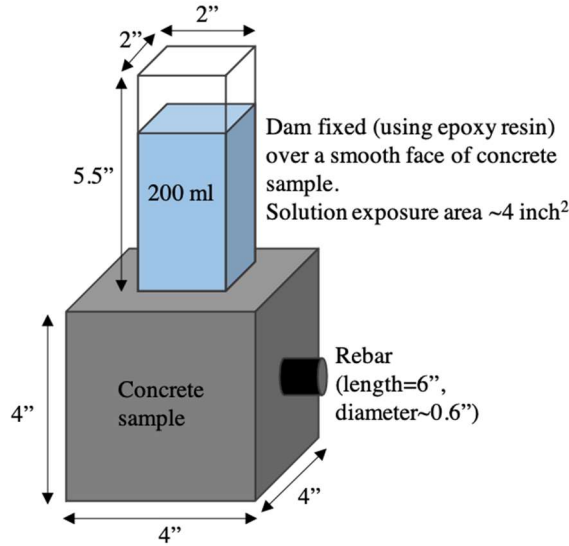


Figure 35. Set-up of tested concrete sample.

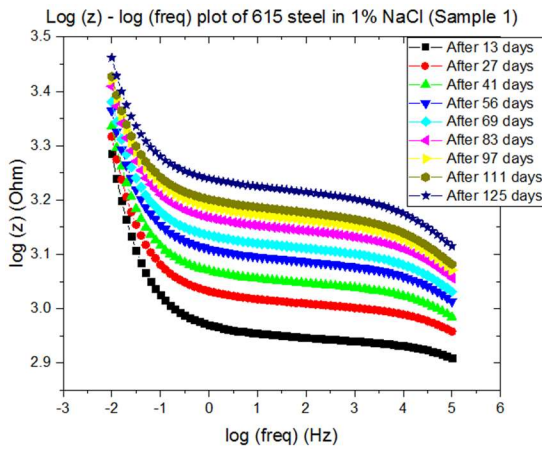
Table 15: Properties of the concrete samples used in the study.

Properties	Magnitudes
w/c	0.53
Curing time	7 days
OPC	Portland cement
Solution exposed area	4 in ²
Coarse aggregate	5/8 "
Fine aggregate	3/8"
Cement: Sand: Aggregates	1:1.5:2
Rebar exposure area (to concrete)	48.6 in ²
Electrolyte	1 wt%, 3.5%wt NaCl

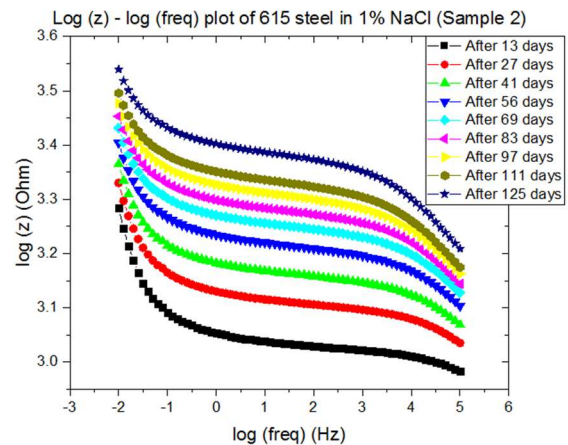
Figure 36 and 37 shows the bare steel in concrete samples following 125 days of exposure. The EIS signal show a mass transfer dominant mechanism where the water uptakes the concrete specimen. By considering the damage evolution model presented in figure 1 or 2a, the rebar was at stage one where the water transport within the concrete solid matrix and has not reached the metallic structure. Different concentration was selected to characterize the activation stage. The 1 and 3.5% NaCl shows a linear behavior for the Nyquist representation and evolution of the high frequency due to the different electrolyte concentration that influences the IR (ohmic drop). The higher concentration shows lower impedance at high frequencies for the complex or Nyquist representation (36e-f and 37e-f). The Bode representation also reveals the change with time for the impedance due to the electrolyte concentration (Figures 36a-b and 37a-b) at high frequencies. The

impedance is the effect of the NaCl concentration rather than the interfacial changes due to the water uptake mechanism occurring. The High-medium frequency range resembles the processes happening within the concrete structure, duplicates corroborate how the impedance drop from 3.1 ohm to 2 ohms with time when the NaCl concentration was at 1%wt NaCl. The higher concentration of NaCl at 3.5 % wt. NaCl influenced the rapid decrease of impedance within the concrete matrix.

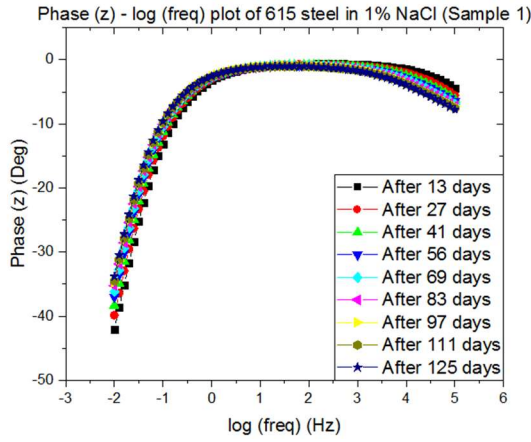
Figures 38 and 39 present the galvanized rebar system with different NaCl concentrations with time. Sample 1094 is the steel rebar with a galvanized (Zn) layer embedded in concrete exposed for more than 100 days. Duplicates samples were included for each conditions and the plots show the RC element faces stage 1 or water uptake process. Figure 38 and 39 compare the same concentration of NaCl used for the galvanized rebar and also for the carbon steel. The complex diagram 38e and 38f shown a semi-infinite diameter evolution with time when exposed in 1% NaCl. The magnitude increased with time due to the higher IR or change due to the surface lower resistance attributed to the Zn outermost layer. The Bode representation also shows an increase in magnitude with time at medium-high frequencies for the same 1%NaCl concentration. Also figures 39 (e) and 39 (f) reveal a high semicircle with infinite diameter after 127 days of exposure and a concentration of 3.5% NaCl for the complex representation. Both concentrations are situated in the stage 1 of the damage evolution. There is no activation of the outermost surface of the rebar. The two concentrations used are higher than the threshold magnitude required for the passive layer breakdown. The expected activation process will mark a change in the control process mechanism and will be detected by the low frequency region.



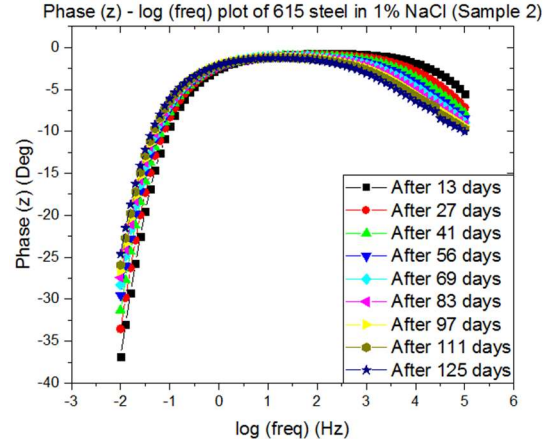
(a)



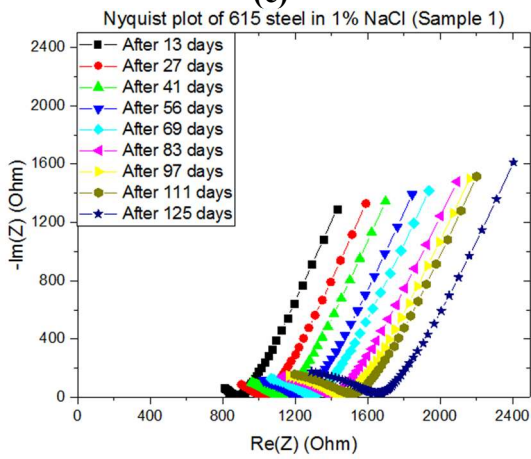
(b)



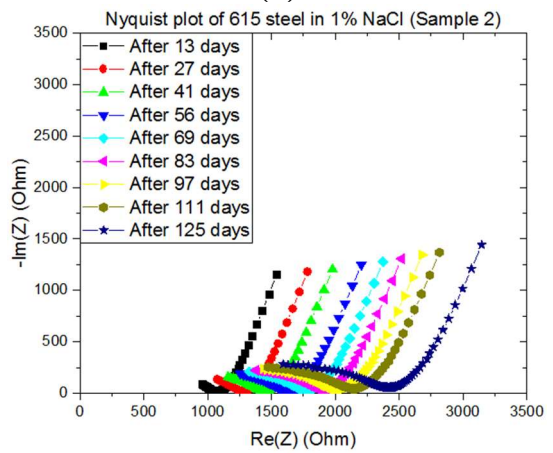
(c)



(d)

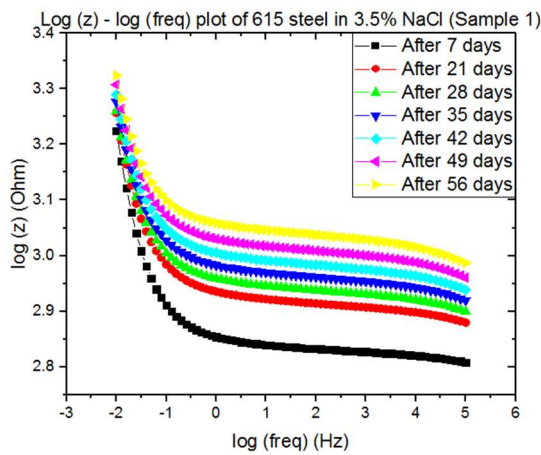


(e)

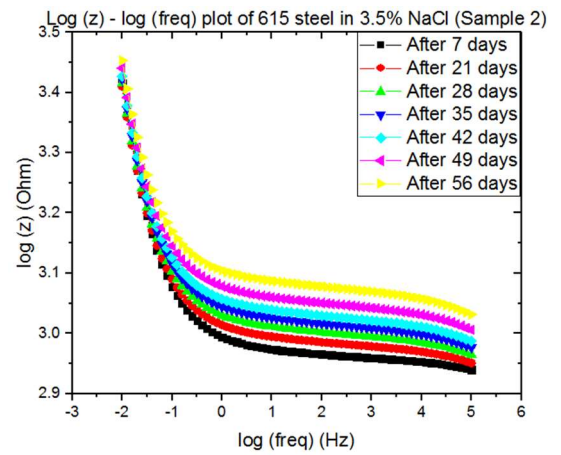


(f)

Figure 36. (a-d) Bode plots of sample 1 and 2, (e-f) Nyquist plots of sample 1 and sample 2 of 615 steel in 1% NaCl.



(a)



(b)

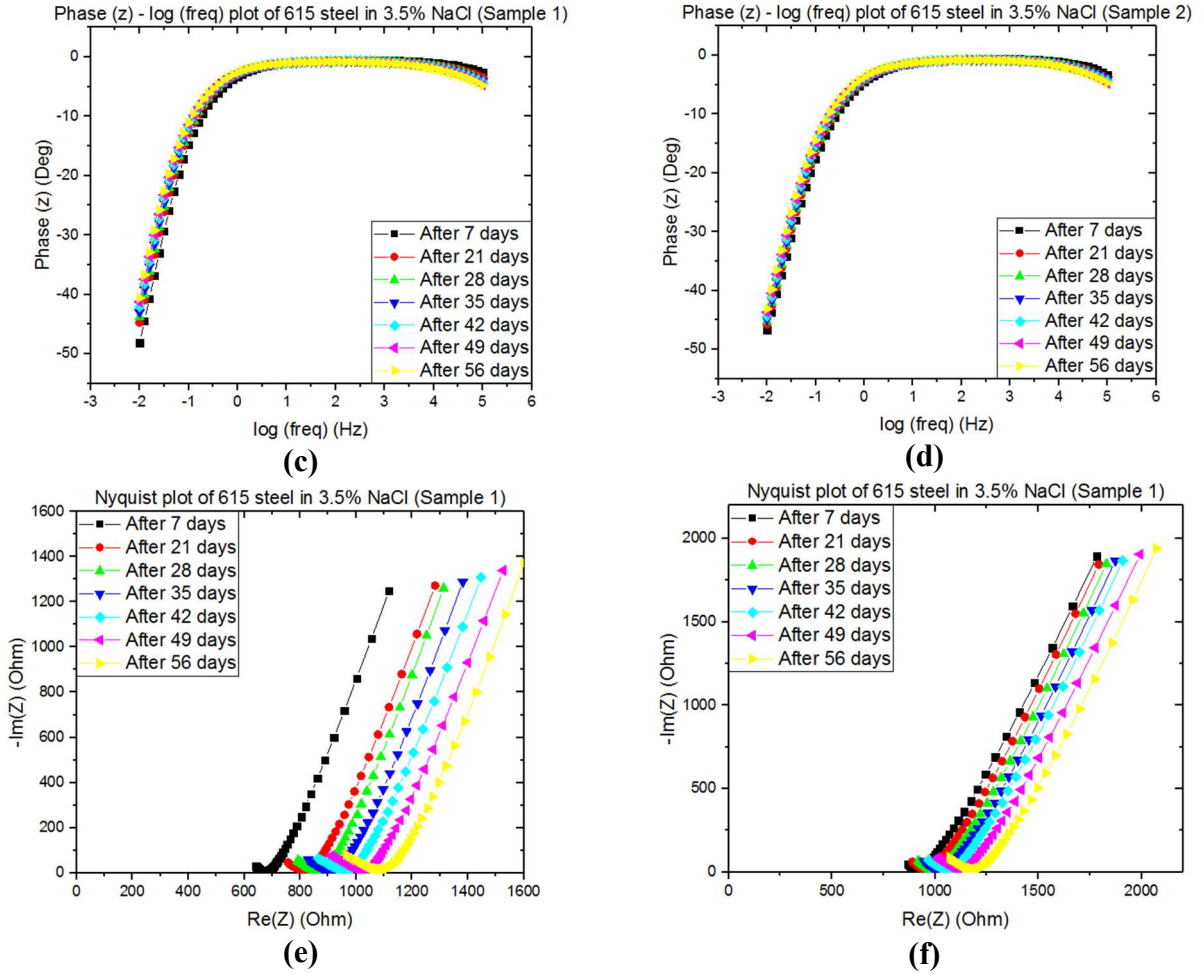
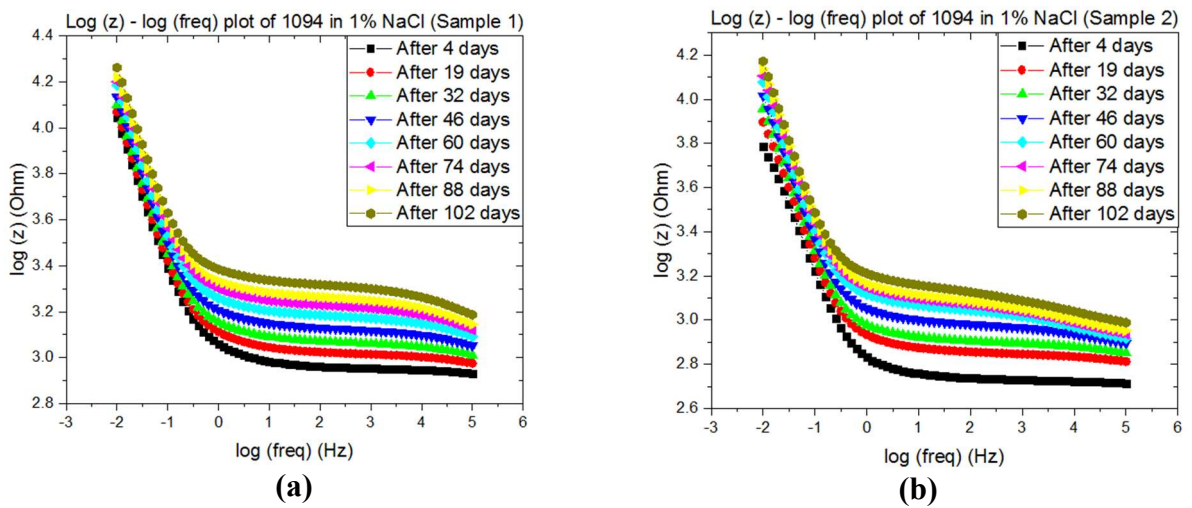
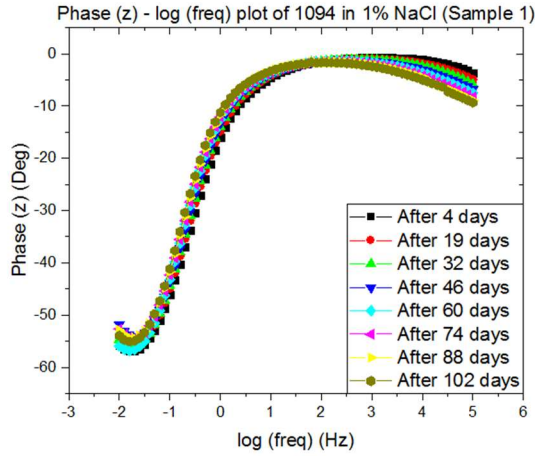
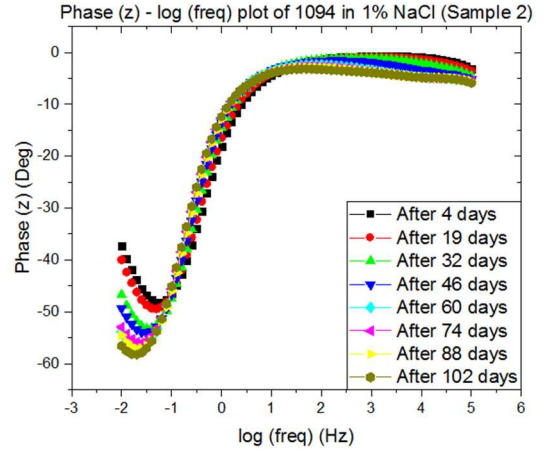


Figure 37. (a-d) Bode plots of sample 1 and 2, (e-f) Nyquist plots of sample 1 and sample 2 of 615 steel in 3.5% NaCl.

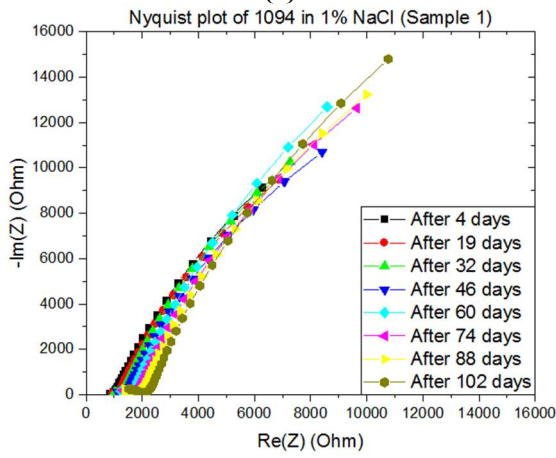




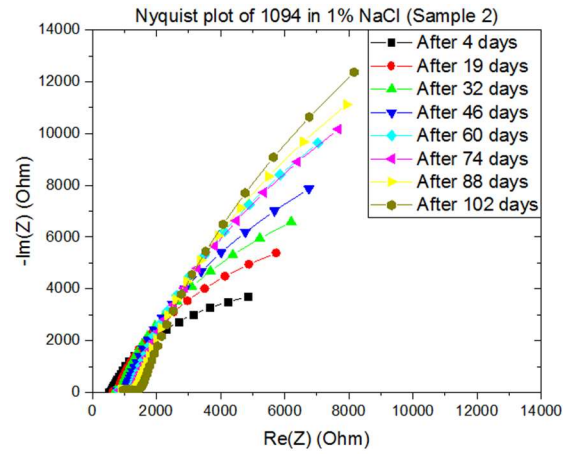
(c)



(d)

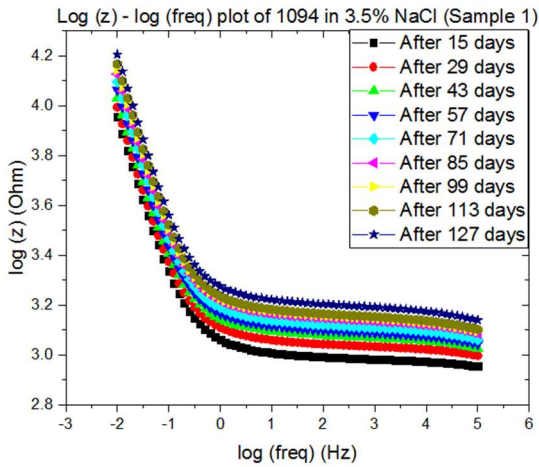


(e)

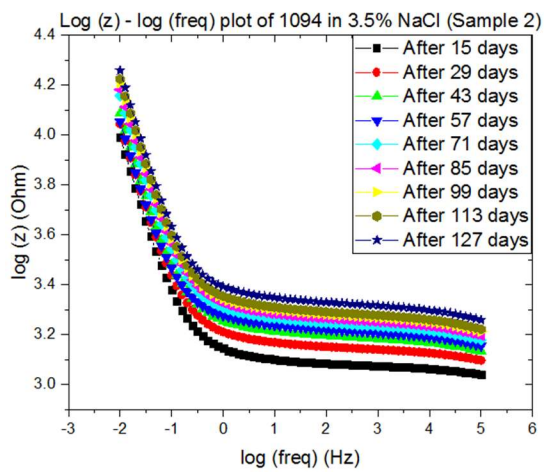


(f)

Figure 38. (a-d) Bode plots of sample 1 and 2, (e-f) Nyquist plots of sample 1 and sample 2 of 1094 in 1% NaCl.



(a)



(b)

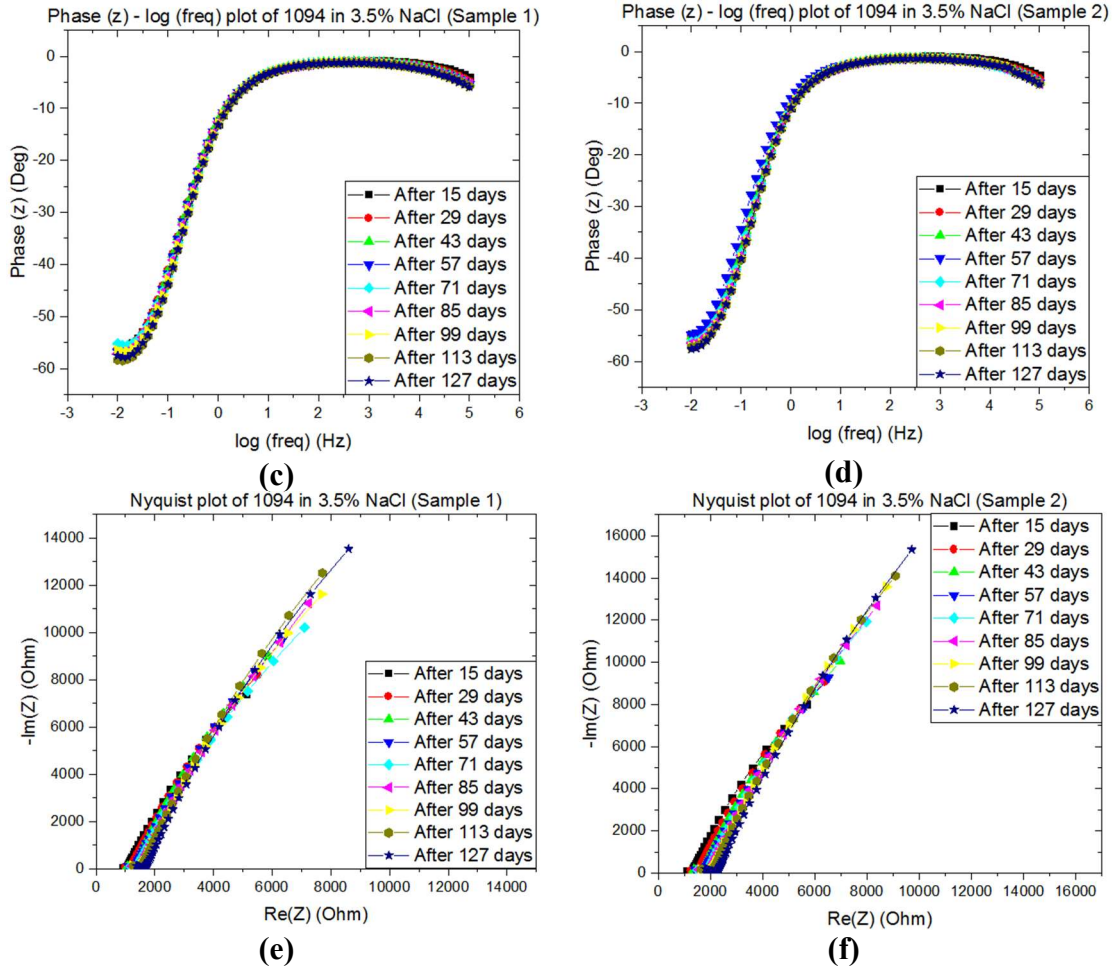


Figure 39. (a-d) Bode plots of sample 1 and 2, (e-f) Nyquist plots of sample 1 and sample 2 of 1094 in 3.5% NaCl.

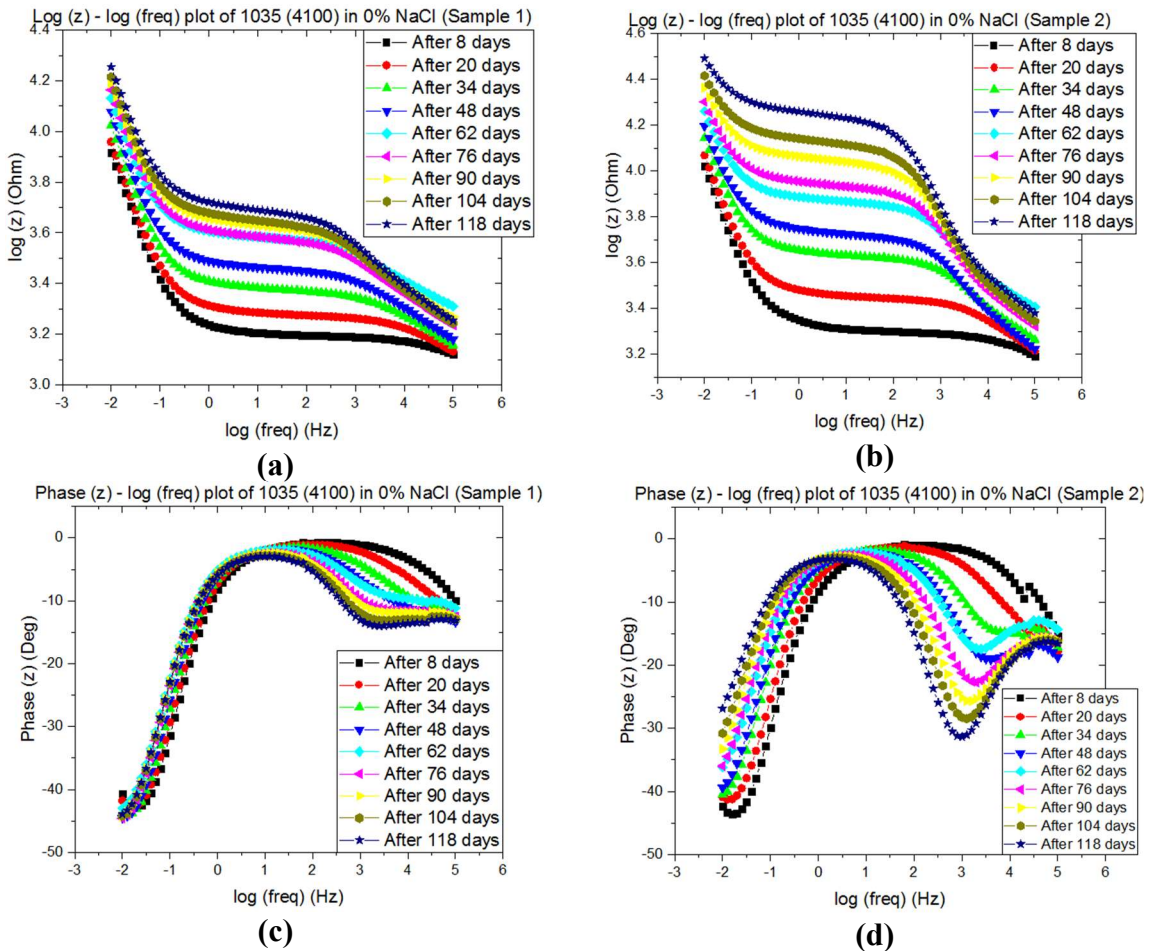
The following figures 40 to 42 show the 1035 rebar including the steel substrate with certain percentage of Chrome and a cover or layer of Zinc. The samples were exposed to more than 119 days in duplicates. The results for each representation indicate a change in the high and medium frequencies, the complex diagram shows the increase of the electrolyte and the solid-state concrete mass magnitudes that are registered or sensed by the high medium frequency range, the electrolyte uptake the concrete matrix and has not reached the surface of the substrate, this latter can be characterized at the low frequencies at longer times. Several works have been shown from several months to years to capture the activation process. The design of the system, the cement composition are some factors influencing the activation time.

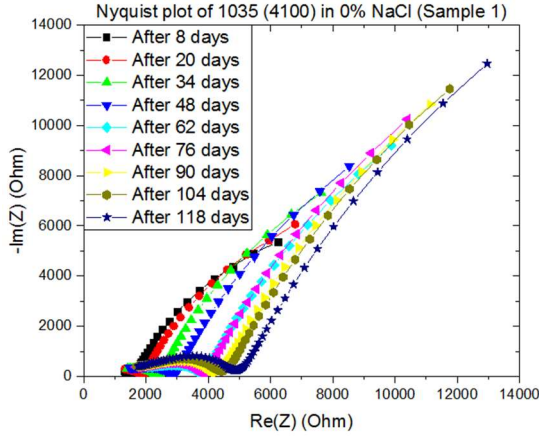
Figure 40 shows the lowest concentration of NaCl at 0%, this magnitude is below the threshold conditions for the breakdown of the layer. This latter is not expected to activate the surface regardless of the exposure time. However, following the exposure time, the surface is not active yet, the same for the higher concentrations, the samples 1035 (CS-M) at 1% and 3.5 % NaCl did not show any rebar activation or charge transfer control process, this latter is the time when the electrolyte reaches the surface of the rebar. Following the same trend were the figures 43 to 45 with different substrate 1035 (CM-z), where the electrolyte uptakes the concrete matrix and has not been able to reach the rebar surface, either to react with the Zinc layer and activate the

sacrificial mechanism or the steel rebar to breakdown of the passive layer. The same concentrations were included as the previous substrate, this latter contains more chrome in the metallic alloy. The current results coincide with the damage evolution schematic for the mechanisms illustrated in Figure 2a and 2b for the steel rebar and galvanized rebar respectively. The following stage waits for the surface activation and interface mechanisms. The pore chemistry simulation performed and reported previously helped to characterize the transition from stage 1 to stage 2 for different systems.

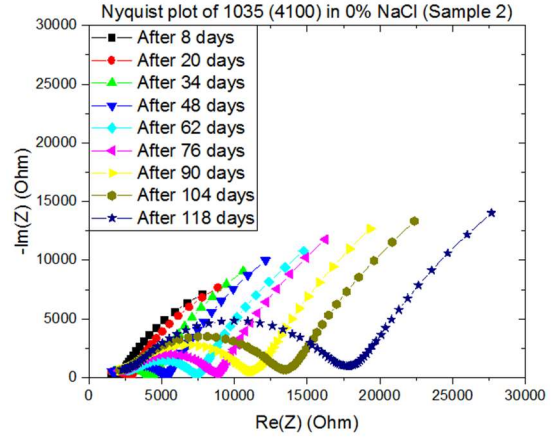
Figure 43 shows an increase of impedance with time by considering the starting exposure time as the reference point. High and medium frequencies displayed an increase in impedance in each representation when concentration of NaCl is at zero. Nyquist or complex representation shows an increase in diameters with time while the phase angle and Bode plot shows also an increase in the angle and total impedance respectively. Figure 44 and 45 shows the same trend in terms of an increase of impedance but for the complex representation there was not a noticeable semicircle at high-medium frequencies instead the resistance magnitude was lower due to the increase of NaCl concentration.

Following more than 120 days the chloride ion has not reached the surface, however we will continue to monitor the performance for longer time and publish the results in a peer review journal.



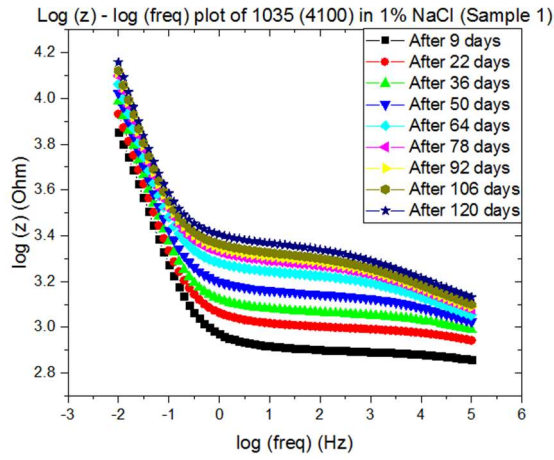


(e)

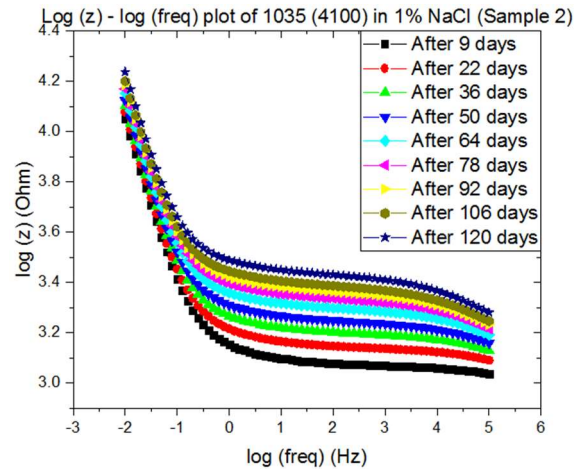


(f)

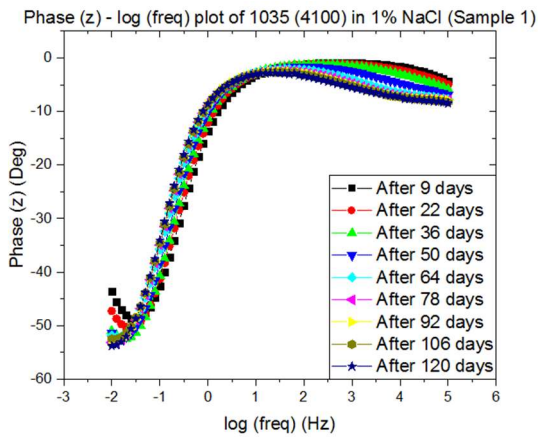
Figure 40.(a-d) Bode plots of sample 1 and 2, (e-f) Nyquist plots of sample 1 and sample 2 of 1035 (CS-M) in 0% NaCl.



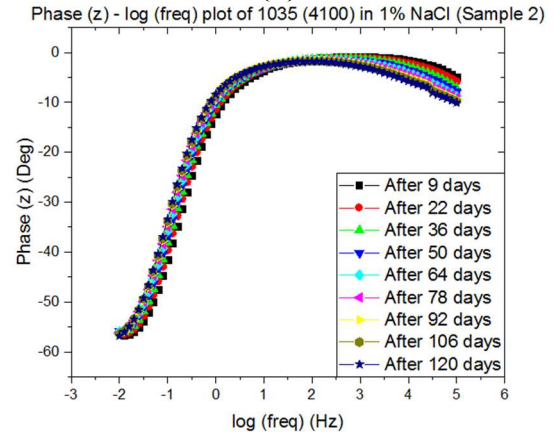
(a)



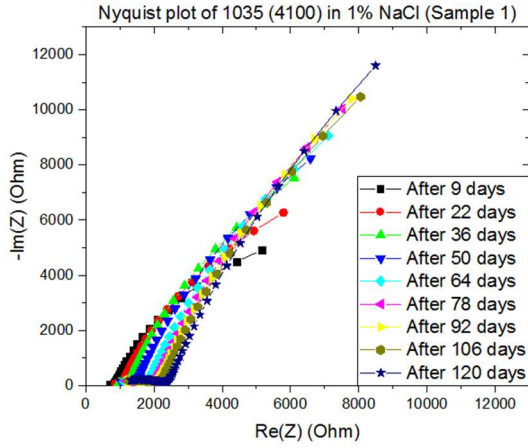
(b)



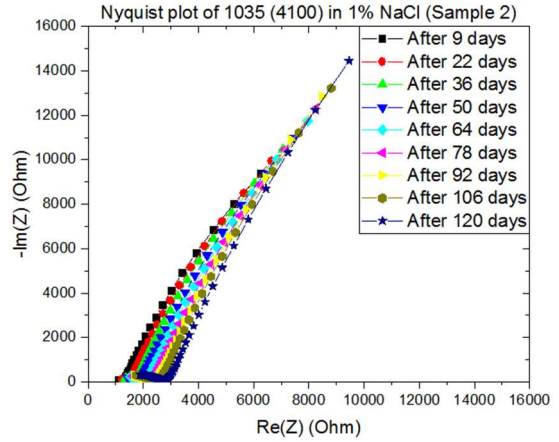
(c)



(d)

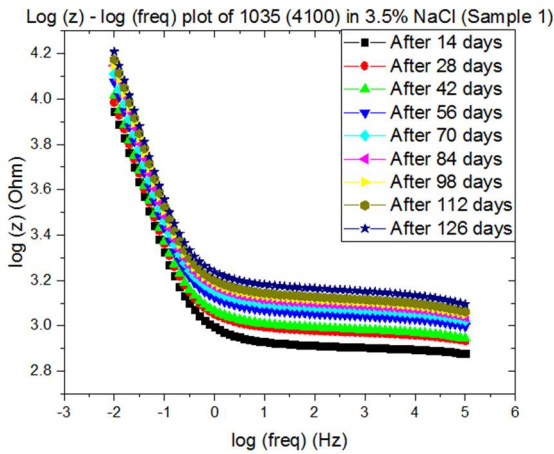


(e)

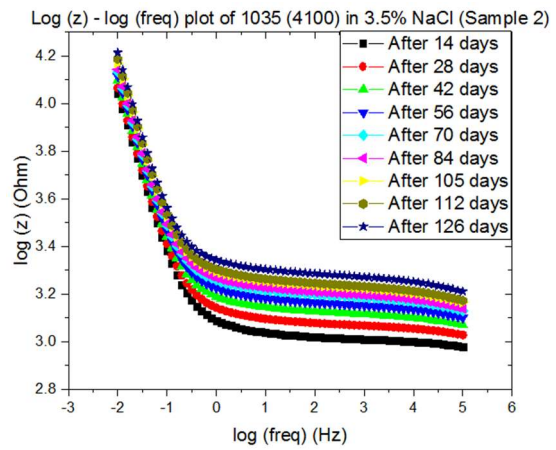


(f)

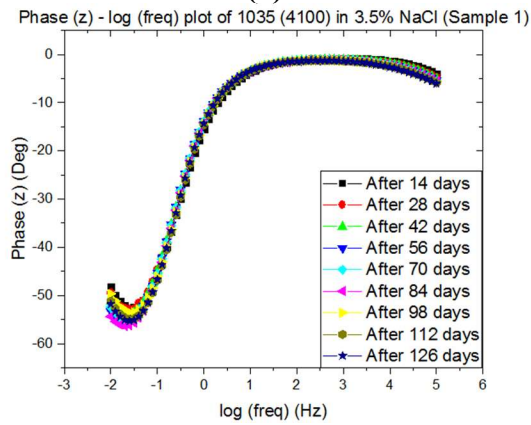
Figure 41. (a-d) Bode plots of sample 1 and 2, (e-f) Nyquist plots of sample 1 and sample 2 of 1035 (CS-M) in 1% NaCl.



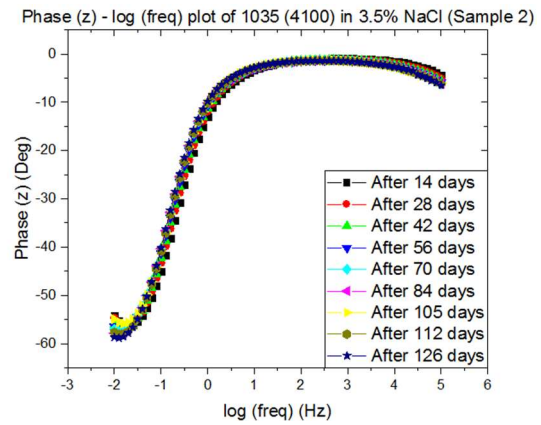
(a)



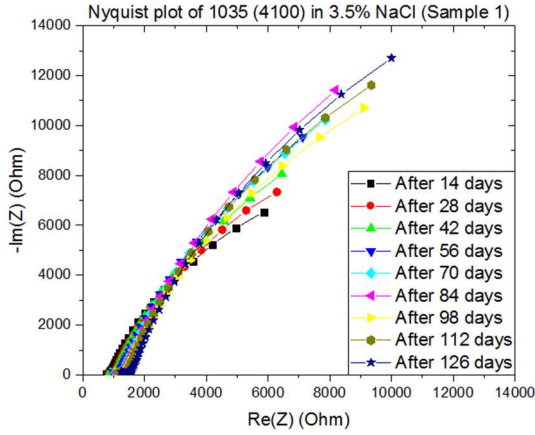
(b)



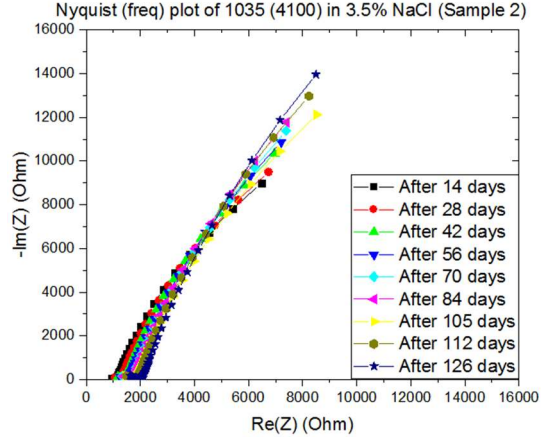
(c)



(d)

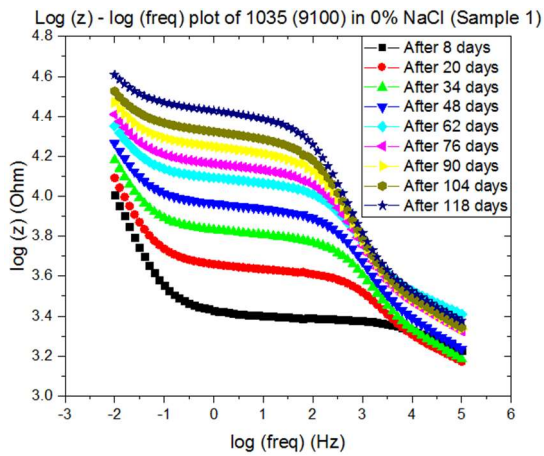


(e)

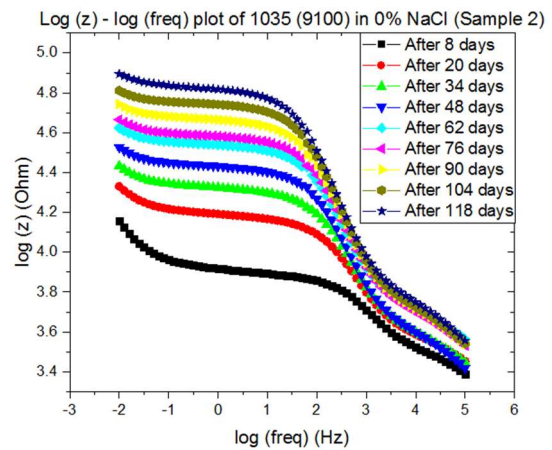


(f)

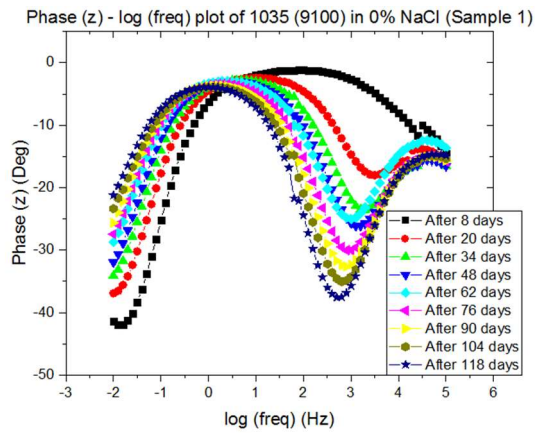
Figure 42. (a-d) Bode plots of sample 1 and 2, (e-f) Nyquist plots of sample 1 and sample 2 of 1035 (CS-M) in 3.5% NaCl.



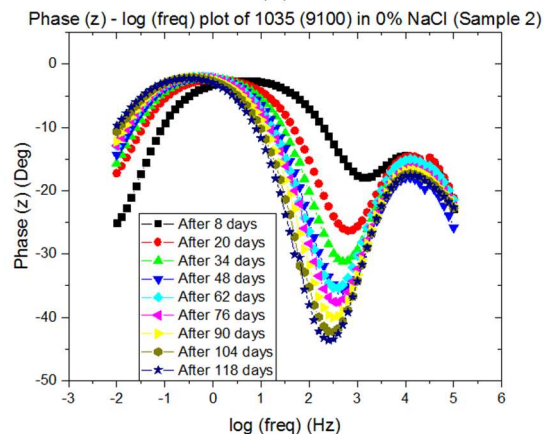
(a)



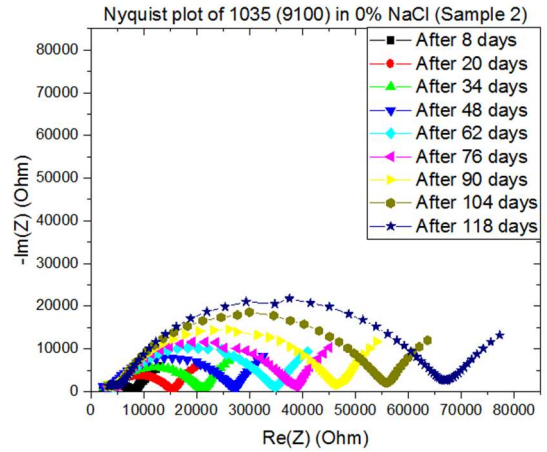
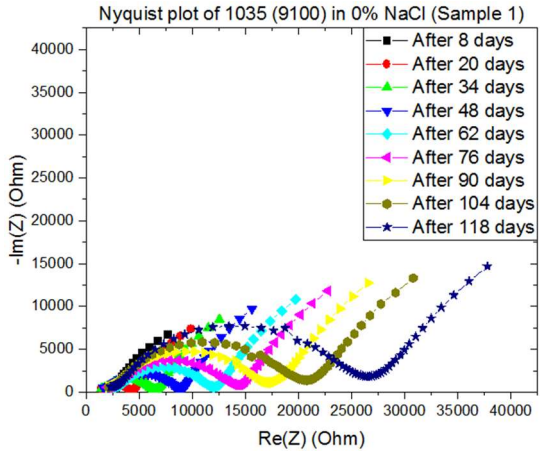
(b)



(c)



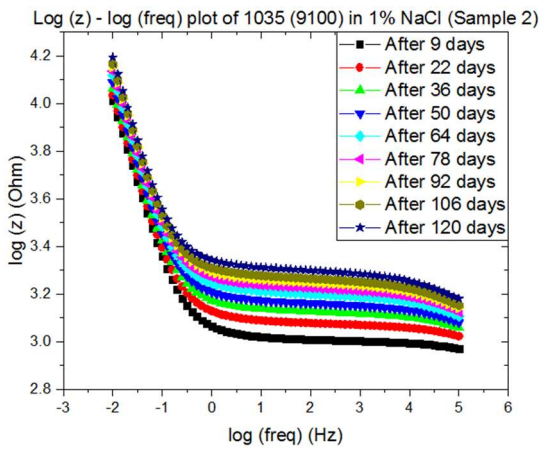
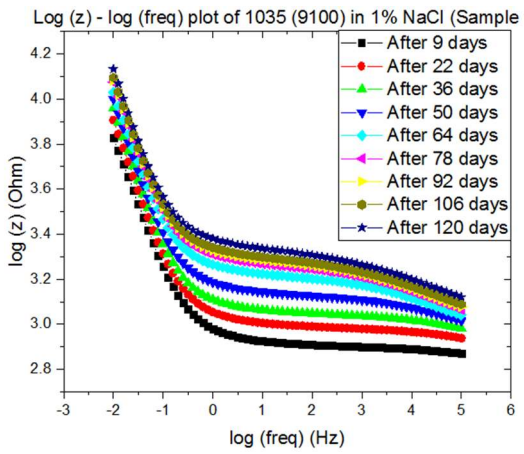
(d)



(e)

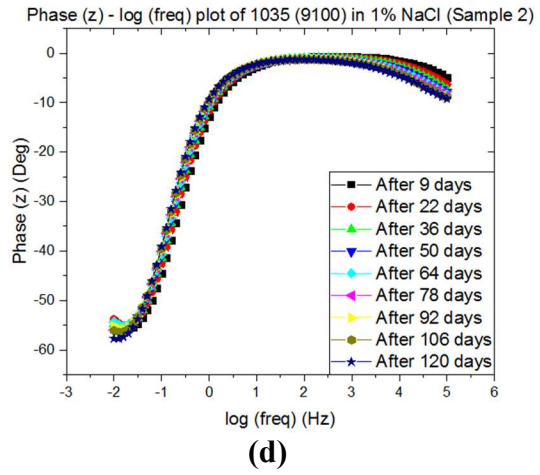
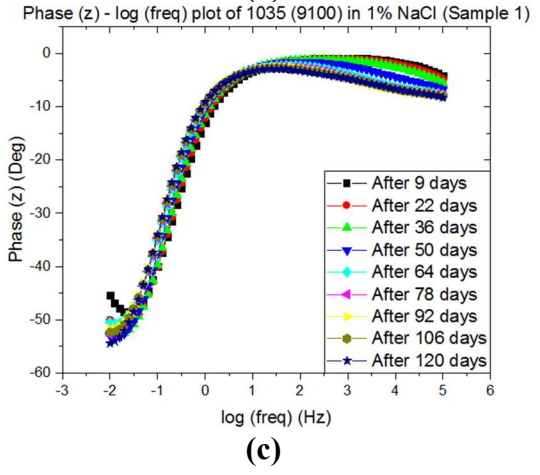
(f)

Figure 43. (a-d) Bode plots of sample 1 and 2, (e-f) Nyquist plots of sample 1 and sample 2 of 1035 (CM-z) in 0% NaCl.



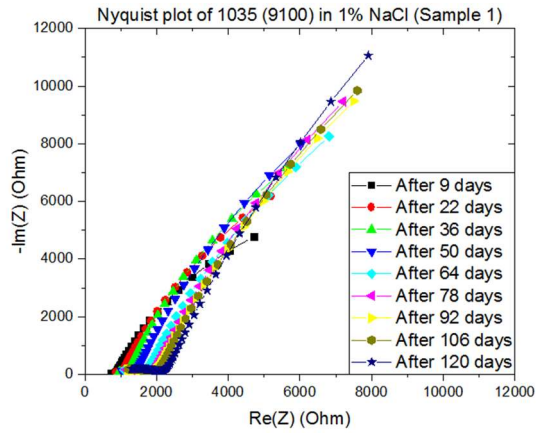
(a)

(b)

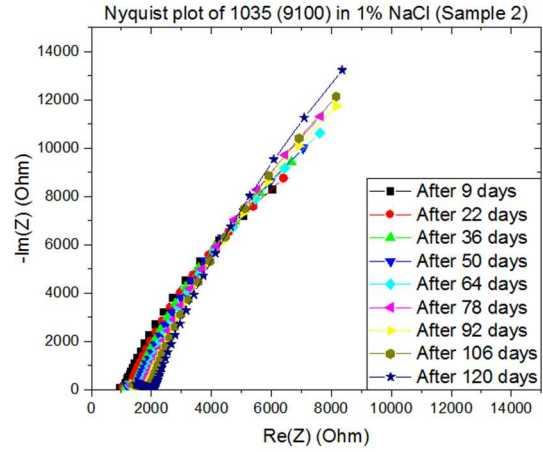


(c)

(d)

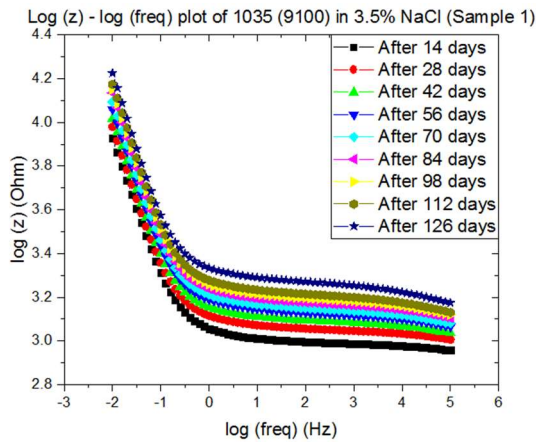


(e)

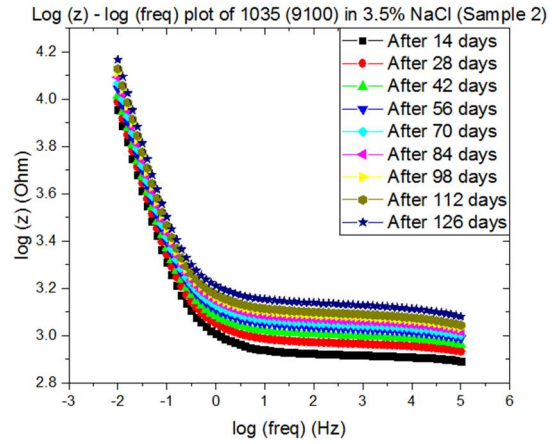


(f)

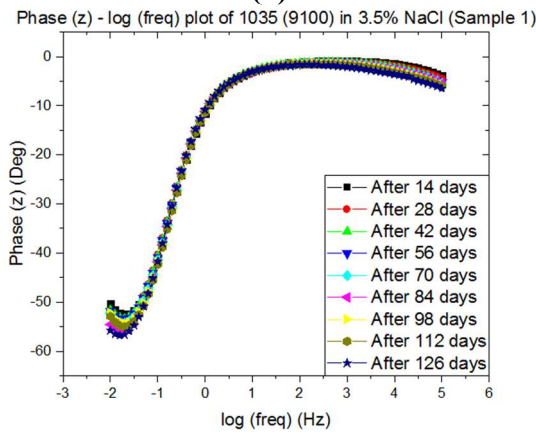
Figure 44. (a-d) Bode plots of sample 1 and 2, (e-f) Nyquist plots of sample 1 and sample 2 of 1035 (CM-z) in 1% NaCl.



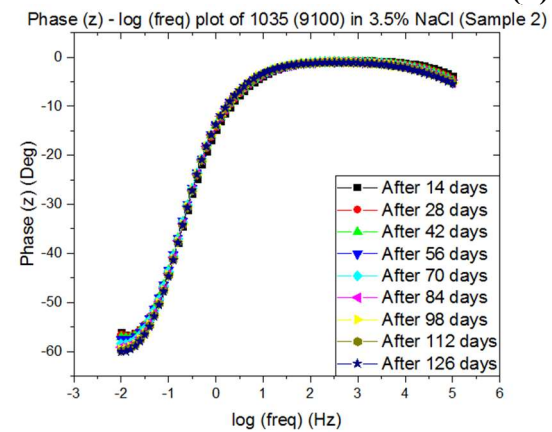
(a)



(b)



(c)



(d)

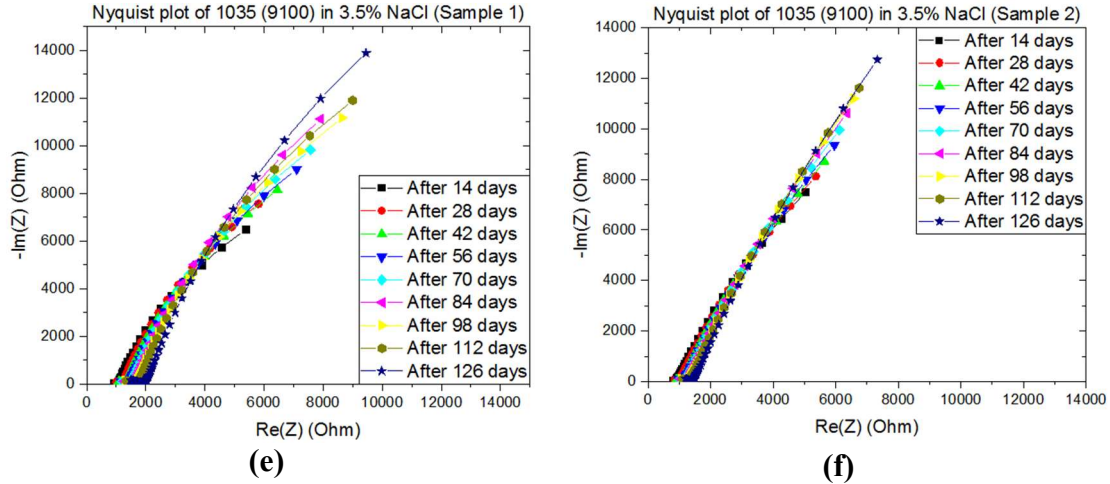
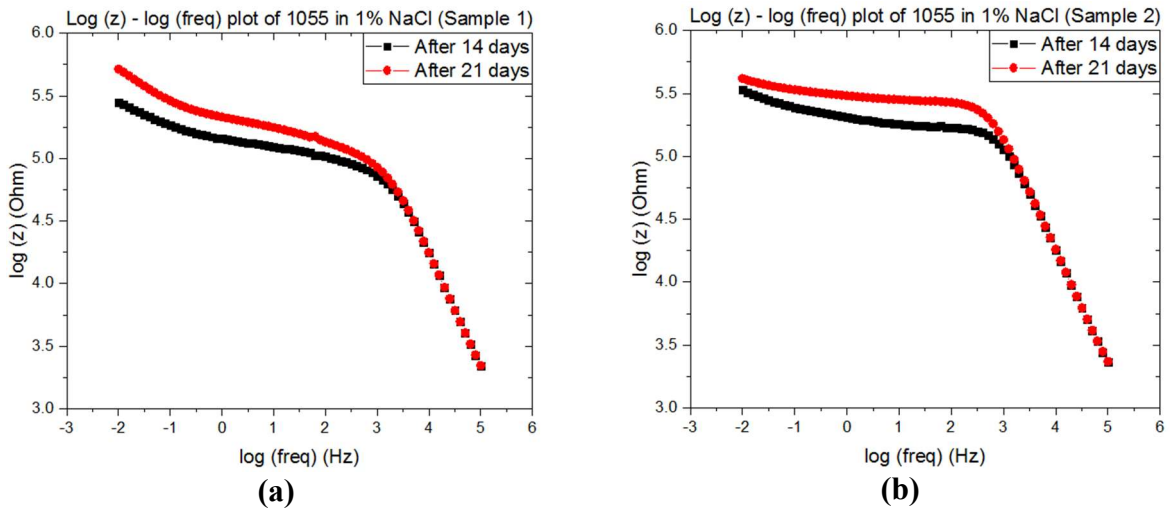
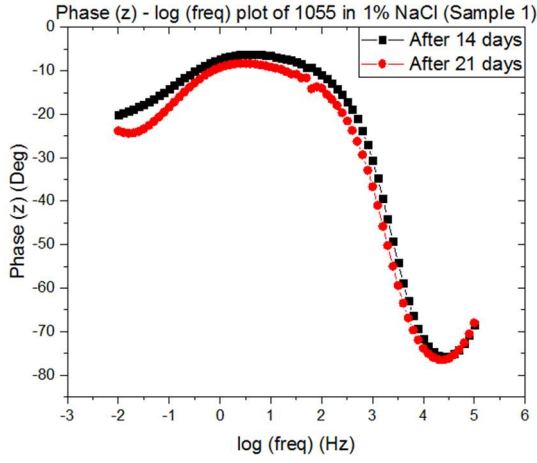


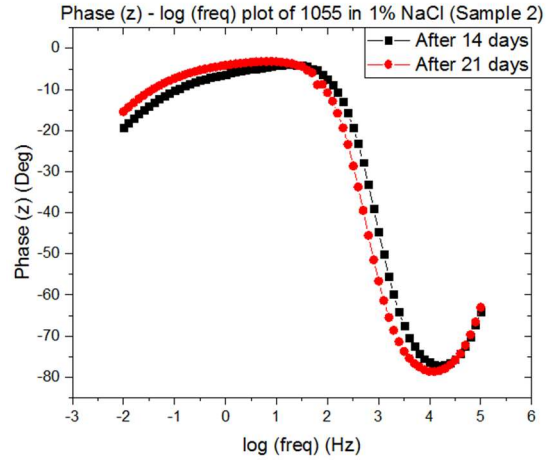
Figure 45.(a-d) Bode plots of sample 1 and 2, (e-f) Nyquist plots of sample 1 and sample 2 of 1035 (CM-z) in 3.5% NaCl.

Figure 46 and 47 show the samples including two layers on the substrate, the first layer is a galvanized layer and the second is an epoxy coating. The EIS results shows two-time constants with the lower NaCl 1% concentration. The time constants indicate a mass transfer process or water uptake within the concrete matrix, also it indicates the impedance of the system is higher than any other system. Figure 47 shows the same double layer system with higher concentration of NaCl 3.5wt% the complex diagram shows one time constant with higher impedance, the duplicates corroborate the results. All the systems faced stage 1 or initiation mechanism, however the previous results with the simulating pore solution gave faster results, the epoxy resulted in higher impedance when the electrolyte reached the outermost surface or epoxy coating, this latter was attributed to the physical barrier layer formed at the surface. For the two layer samples, the research team of this project expect to have the same results as the simulating pore solution in terms of damage evolution. The samples will be monitored for longer time to characterize the change from initiation to active stage and reported in a peer review journal.

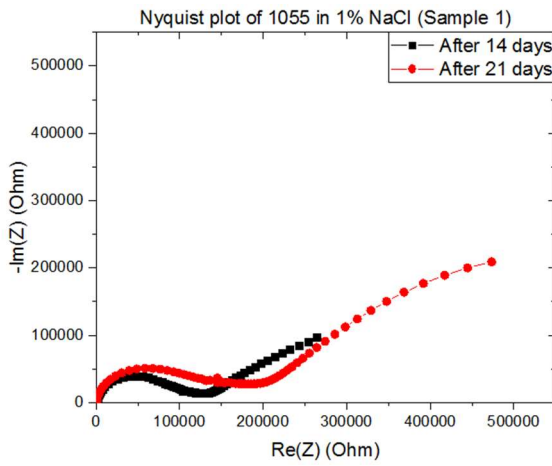




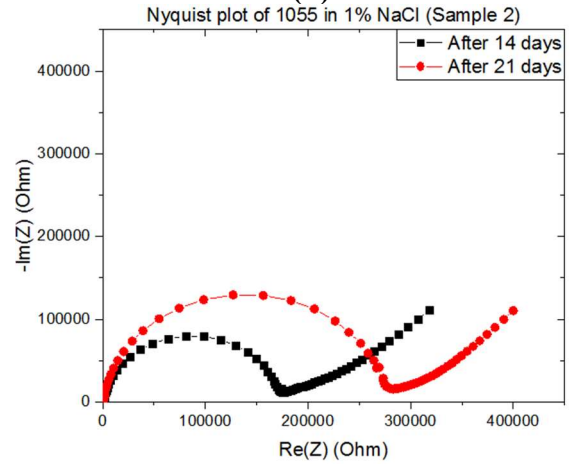
(c)



(d)

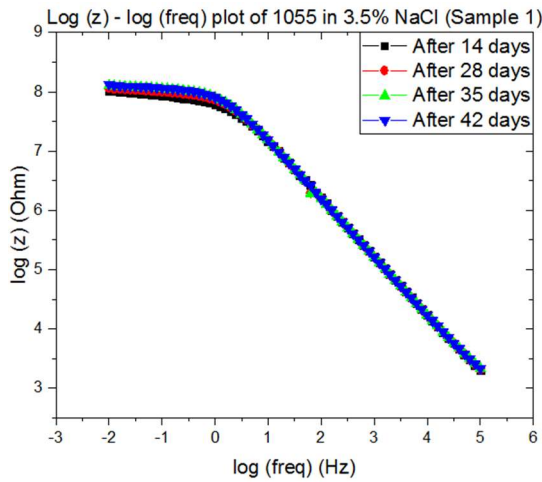


(e)

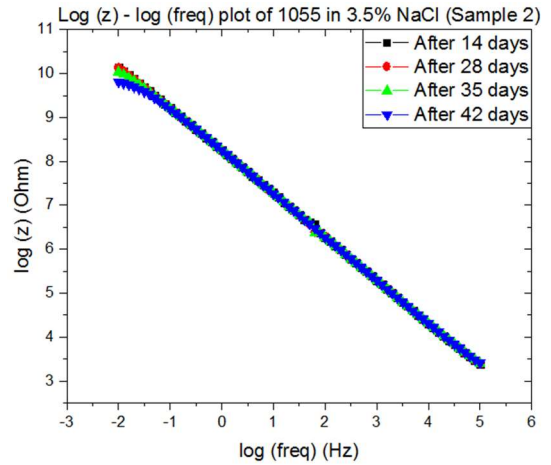


(f)

Figure 46.(a-d) Bode plots of sample 1 and 2, (e-f) Nyquist plots of sample 1 and sample 2 of 1055 in 1% NaCl.



(a)



(b)

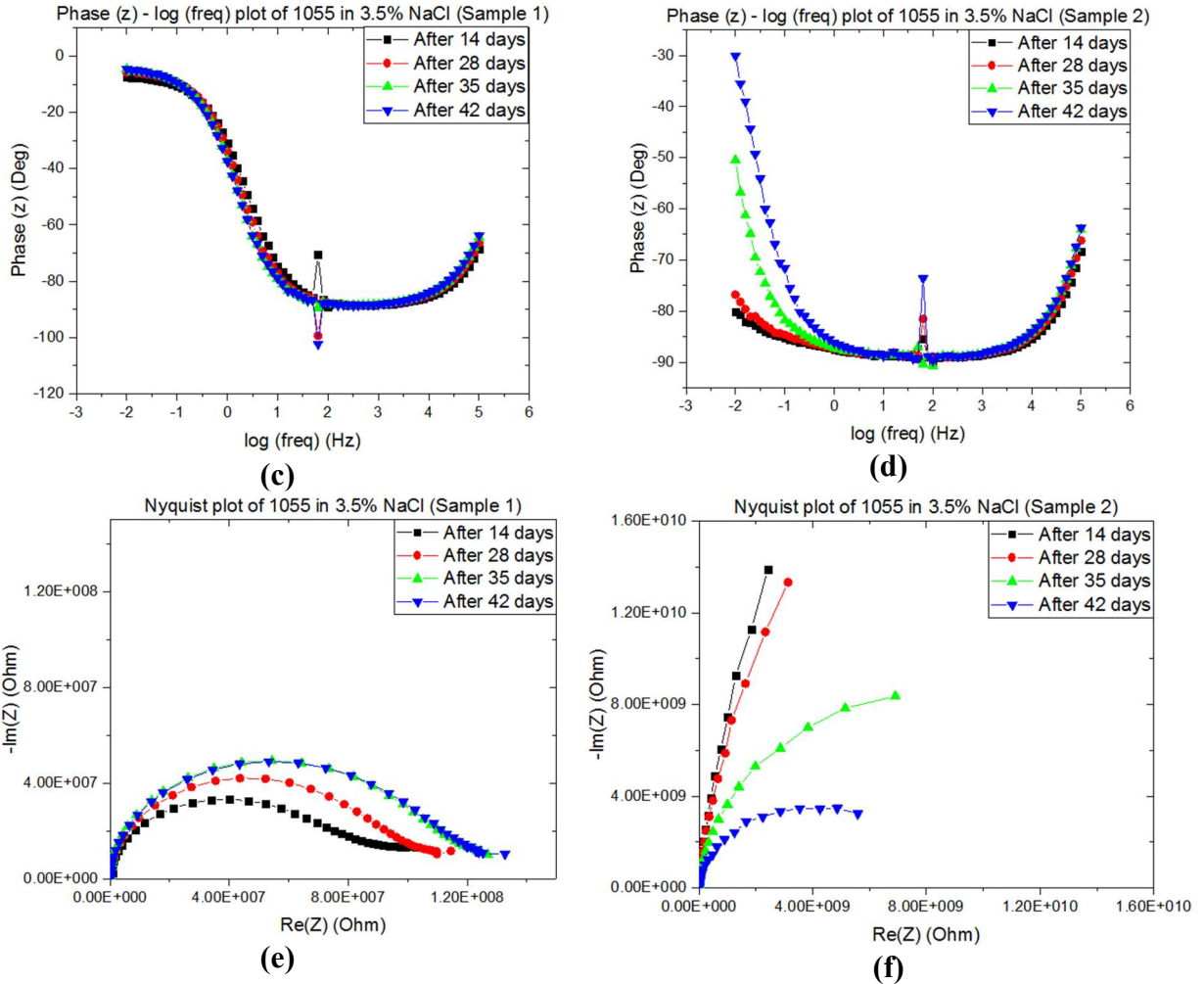


Figure 47. (a-d) Bode plots of sample 1 and 2, (e-f) Nyquist plots of sample 1 and sample 2 of 1055 in 3.5% NaCl.

Based on the Bode and Nyquist plots, it is evident that the solution has not reached the rebar yet. However, from the plots shifting towards the right in the Nyquist plots, it can be inferred that the resistance of concrete was changing due to ingress of the solution into the concrete sample. Irrespective of whether it was a bare rebar or galvanized rebar, the Nyquist plots showed a curvature indicative of a loop fitted using a constant phase element. The presence of the tail in Nyquist curves was inferred to be due to diffusion (fit using the Warburg element, shown in Figure 48(b)) since the solution was still moving through the concrete cover. The circuits used to fit the data have been shown in Figure 48. Figure 48(a) was used to fit data without the diffusion-related tail in the Nyquist curve. In the circuits, R1 indicates the resistance of the concrete while R2 indicates the charge transfer resistance which is of importance in this study.

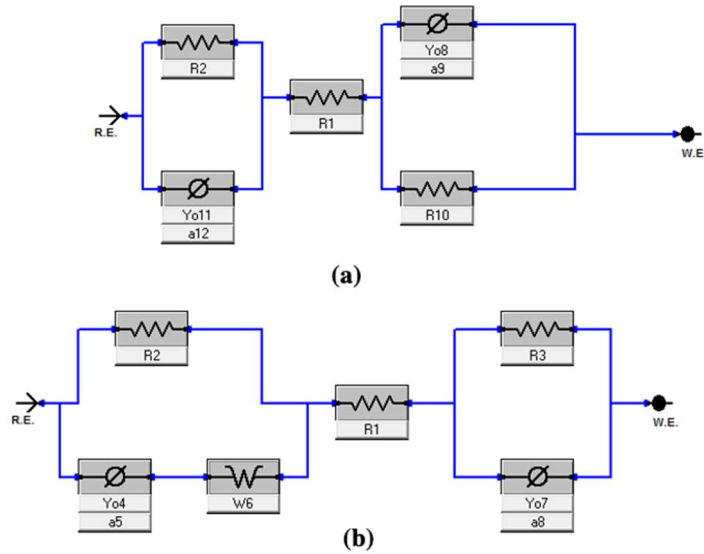


Figure 48. Circuits used to fit the EIS data.

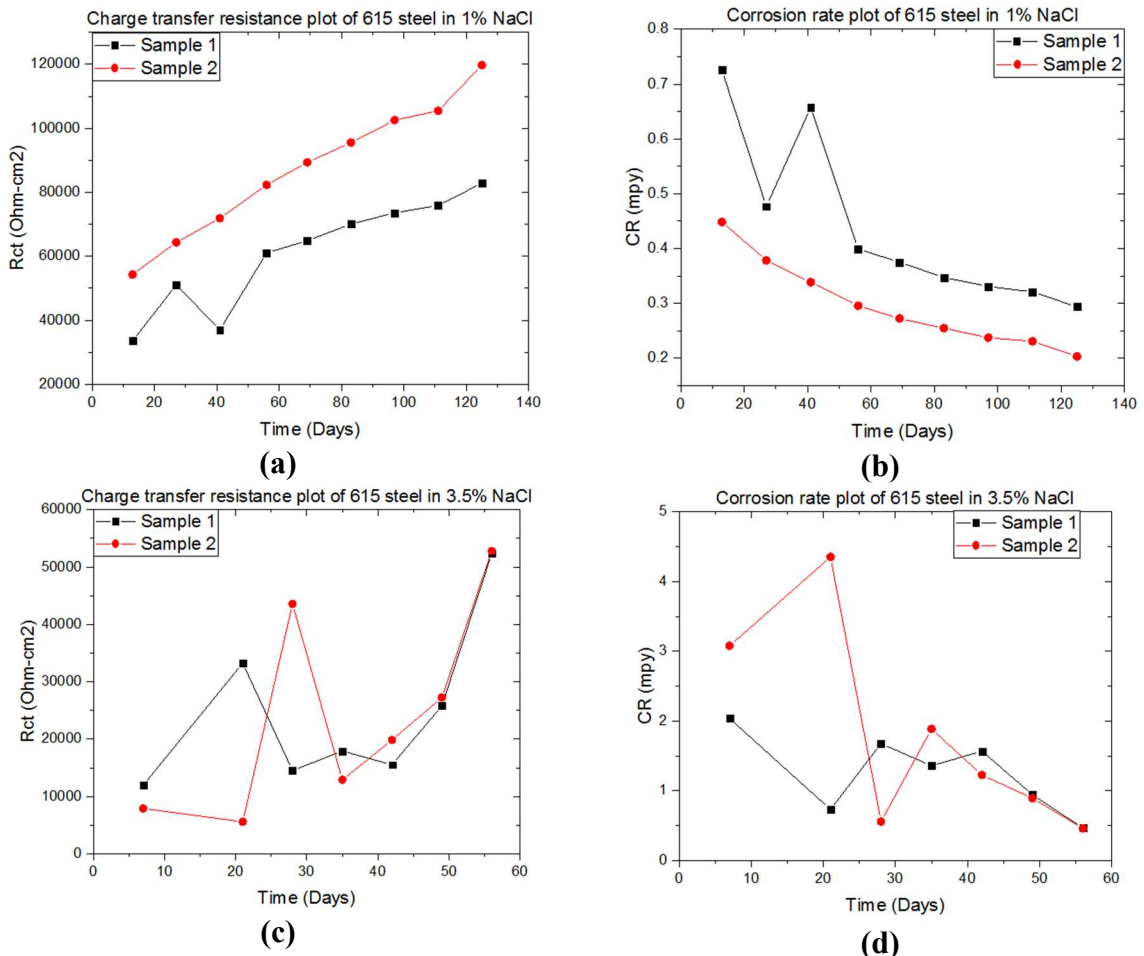
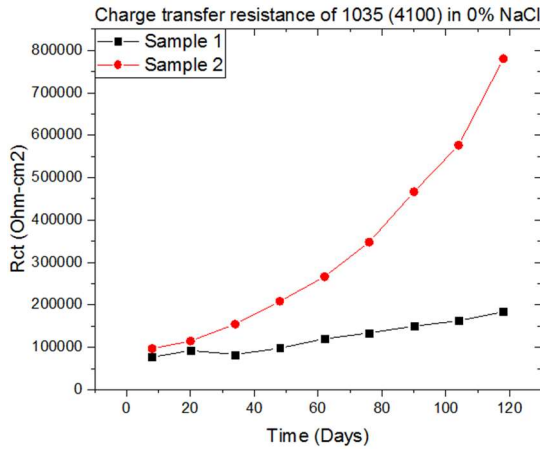


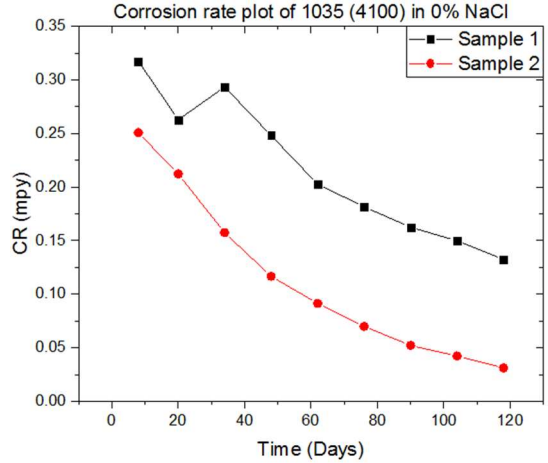
Figure 49. Change in charge transfer resistance of 615 steel in (a) 0% NaCl, (c) 1% NaCl, (e) 3.5% NaCl and corrosion rates in (b) 0% NaCl, (d) 1% NaCl, (f) 3.5% NaCl with time.

Figure 49 shows the charge transfer resistance and corrosion rate plots obtained. At medium term (between 60 days) of exposure the general trend was the increasing charge transfer resistance and decreasing corrosion rate magnitude. The later can be the reduction reaction rather than the dissolution of the metallic rebar. The water uptake process did not reach the surface of the rebar. The charge transfer process is dominated by the oxygen reduction reaction. The charge transfer resistance magnitude was inversely proportional to the NaCl concentration, the higher the concentration the lower the Rct magnitude was obtained.

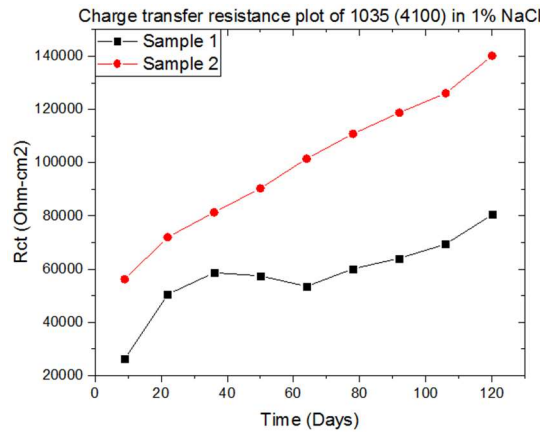
The following figures 50 to 52 show the equivalent trend for the Rct or charge transfer magnitude at longer period of time (>120days), the general trend can be related to the concentration of NaCl to be inversely proportional to the charge transfer mechanism dominance. Due to the water uptake process we related the Rct magnitudes to the cathodic reaction or oxygen reduction occurring at the zinc outermost layer on the rebar.



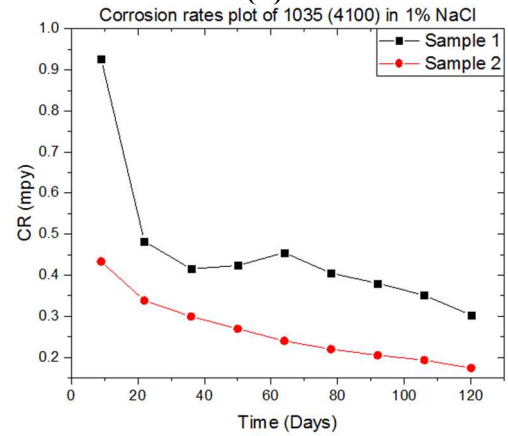
(a)



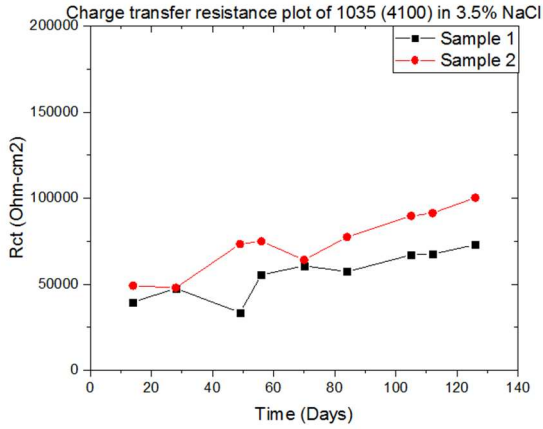
(b)



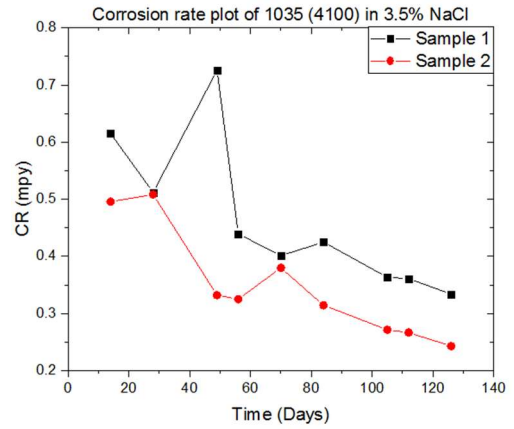
(c)



(d)

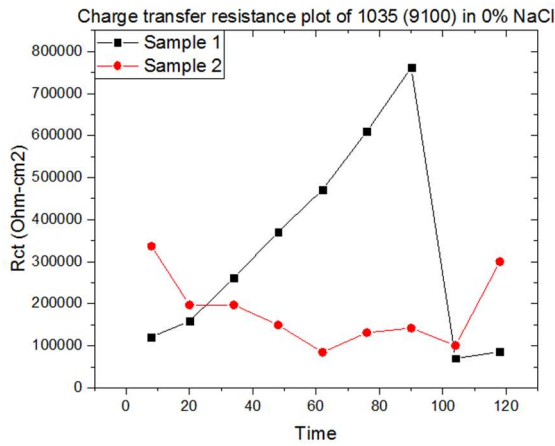


(e)

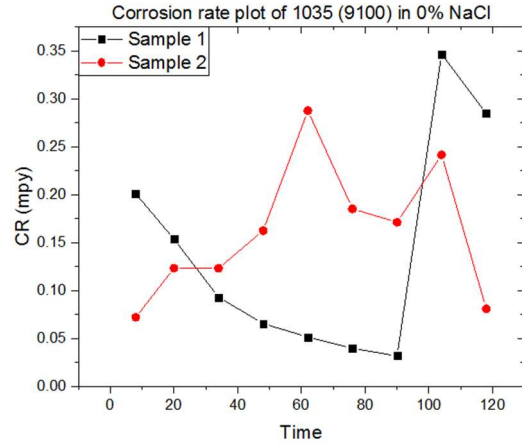


(f)

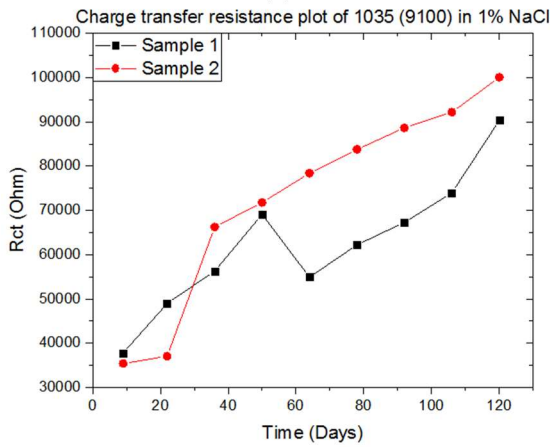
Figure 50. Change in charge transfer resistance of 1035 (CS-M) in (a) 0% NaCl, (c) 1% NaCl, (e) 3.5% NaCl and corrosion rates in (b) 0% NaCl, (d) 1% NaCl, (f) 3.5% NaCl with time.



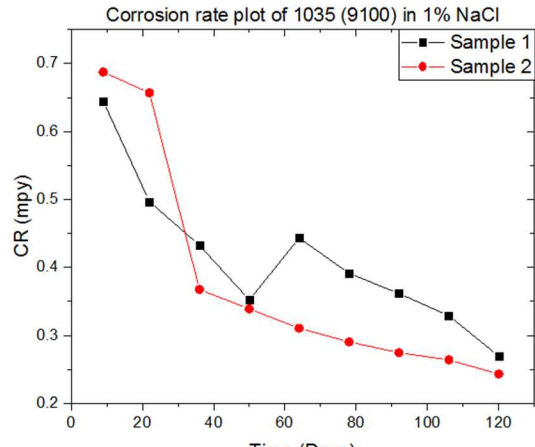
(a)



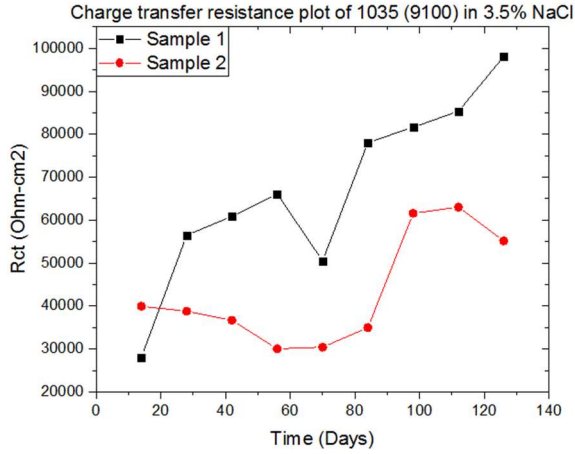
(b)



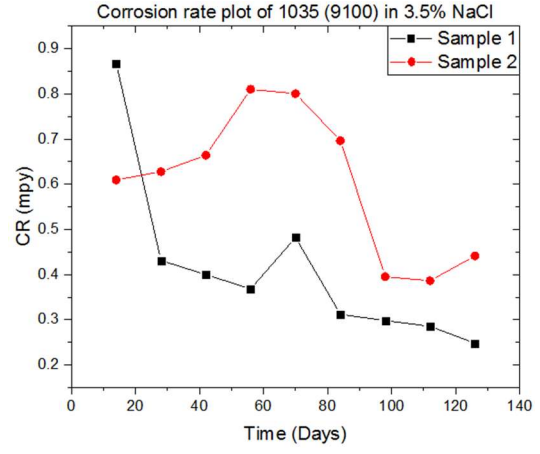
(c)



(d)

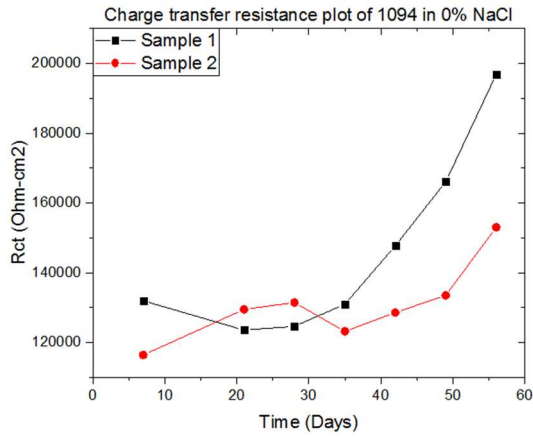


(e)

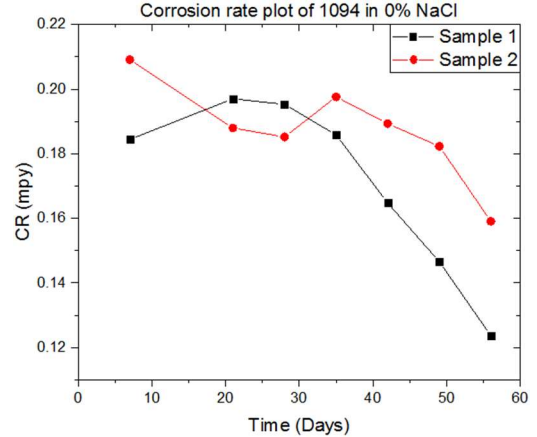


(f)

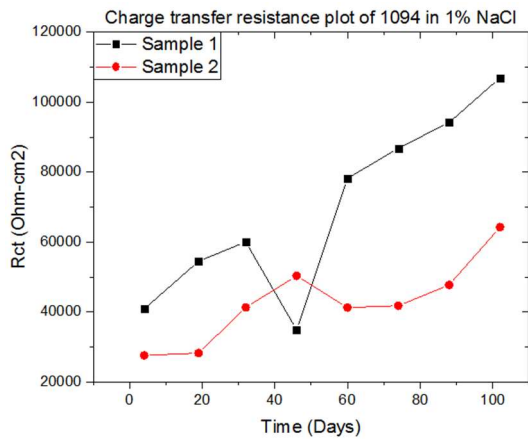
Figure 51. Change in charge transfer resistance of 1035 (CM-z) in (a) 0% NaCl, (c) 1% NaCl, (e) 3.5% NaCl and corrosion rates in (b) 0% NaCl, (d) 1% NaCl, (f) 3.5% NaCl with time.



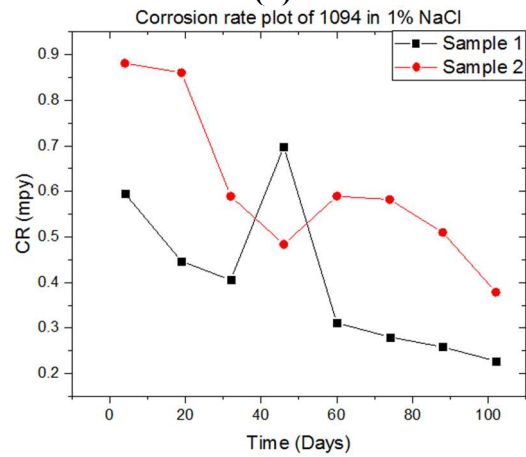
(a)



(b)



(c)



(d)

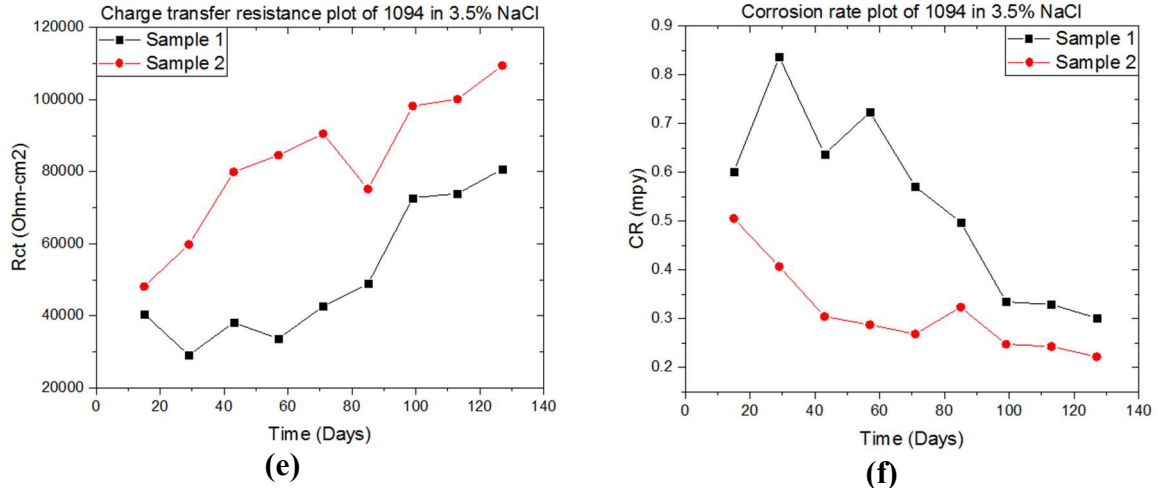


Figure 52. Change in charge transfer resistance of 1094 in (a) 0% NaCl, (c) 1% NaCl, (e) 3.5% NaCl and corrosion rates in (b) 0% NaCl, (d) 1% NaCl, (f) 3.5% NaCl with time.

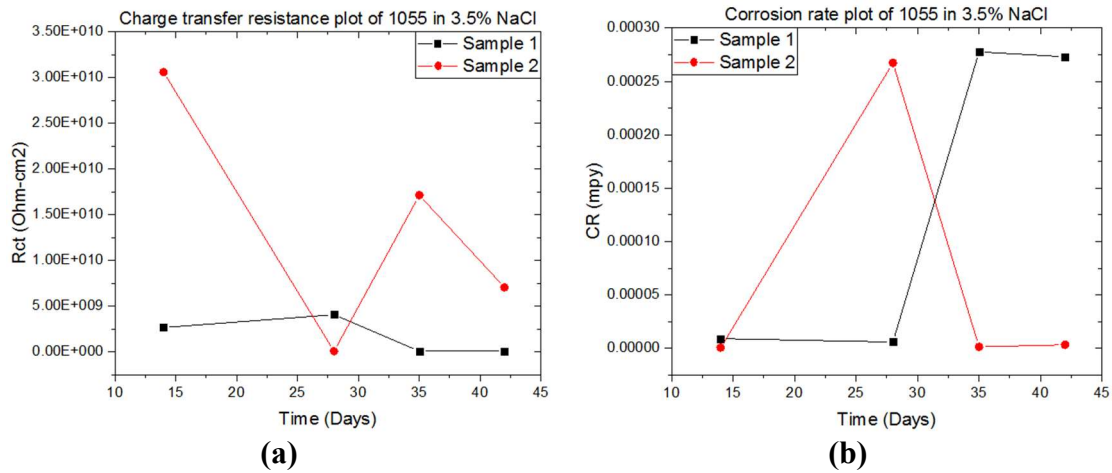


Figure 53. Change in charge transfer resistance of 1055 in (a) 3.5% NaCl and corrosion rates in (b) 3.5% NaCl with time.

Figure 53 shows the charge transfer resistance magnitude in the range of tens giga-ohms or higher and show constant magnitude due to the two-layer covering the rebar. At short term (40 days) of exposure the charge transfer resistance and the corrosion rate are related to the reduction or oxygen reaction at the epoxy layer. Once the solution reaches the rebar, it is expected that the interface will be activated and stage 2 (based on figure 2) will start due to the inner layer of Zn. The activation will influence the increase or variation in the corrosion rate.

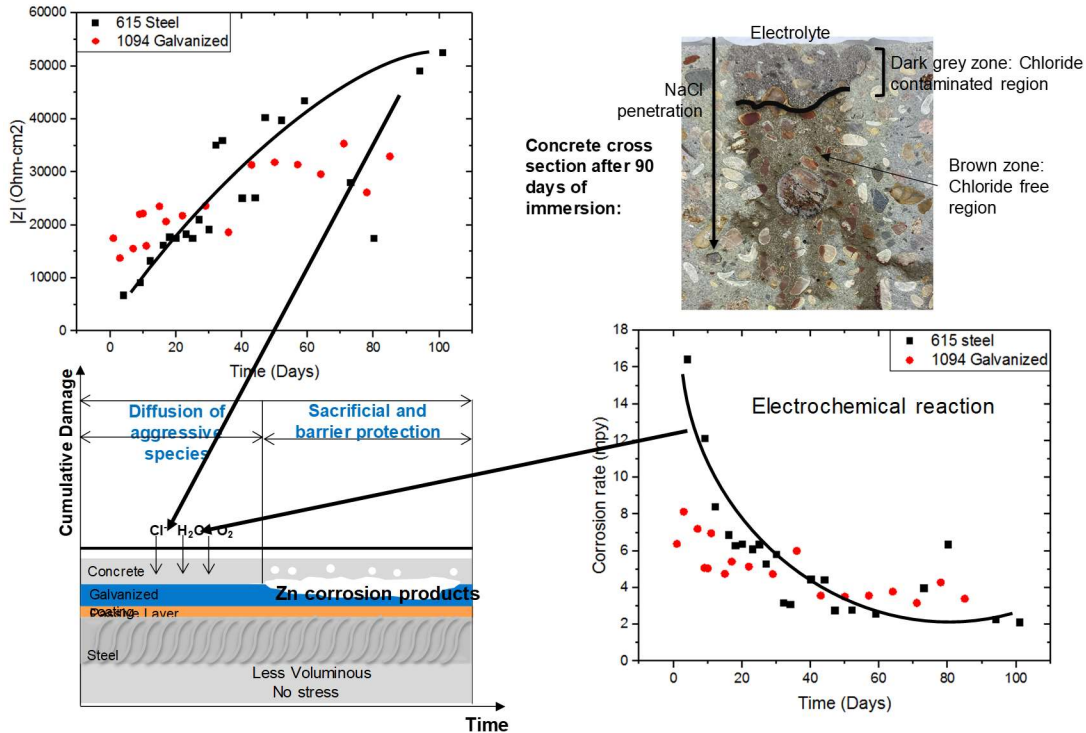


Figure 54: Stage 1 results for RC element with steel and galvanized steel.

Figure 54 shows the impedance and corrosion rate trend of the tested materials which as described above is indicative of the fact corrosion has not been initiated at the rebar interface. Instead, the oxygen reaction is sensed and monitored. The figure also shows an image of the cross section of a concrete sample tested with solution exposure up to 90 days (~3 months) on which silver nitrate and potassium chromate were sprayed. These chemicals react with elements in concrete turning the color dark grey where chlorides are present and reddish brown/yellow where chlorides are not present. The results of this test also confirm the fact that the chlorides transport or electrolyte uptake are still in stage 1 as illustrated in figure 55 (stage 1).

4.11. Deterministic Modeling

In this task, the theoretical modeling with RC elements and electrolyte characteristics, as well as their validation with electrochemical and concrete testing, is developed. A simple model based on rebar/concrete interface mechanistic analysis and real-time monitoring characterization in corrosive environments helped to develop a deterministic approach, as illustrated in Table 2.

4.11.1. Equivalent circuits analog

To interpret the EIS spectra obtained through the aforementioned experiments, suitable equivalent circuit models were constructed depending on the configuration of each sample designed, as shown in Figure 54. It is proposed for expressing the appropriate system degradation as extracting the appropriately representative effective values of the electrochemical systems.

First, the counter sample, which did not have any coating, was initially expressed on the charge transfer phenomenon as a major signal, but over immersed time, it was described as Figure 54(a-2) because it could observe the additional time constant according to the formation of the oxide film on the surface of substrate. In the case of 1055 samples covered with organic coating, if proper barrier is formed against the penetration of electrolyte, there will be no electrochemical reaction

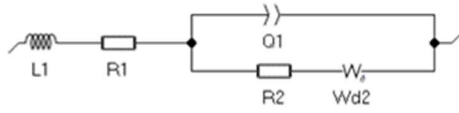
in the early state of immersion. It can be expressed as shown in Figure 54(b-1). However, when the organic barrier breaks down, the electrolyte penetrates into the coating and reaches at the metal surface, and then, electrochemical reaction takes place. Thus, the circuit model as shown in Figure 54 (b-2) is suggested. For the samples composed of the remaining various metallic coatings, the same circuit model was proposed considering the three representative phenomena, including the variation of film formation, charge transfer phenomenon, and diffusion phenomenon, to compare and analyze the changes in properties from the global perspective point of view. For the expression of diffusion phenomena, Warburg, which is commonly used to express diffusion impedance, is not used. Following diffusion impedance is considered, which is frequently used in rotating electrode.

$$Z_{wd}(f) = R_d \frac{\tanh \tanh (\sqrt{\tau_d j 2\pi f})}{\sqrt{\tau_d j 2\pi f}} \quad [29]$$

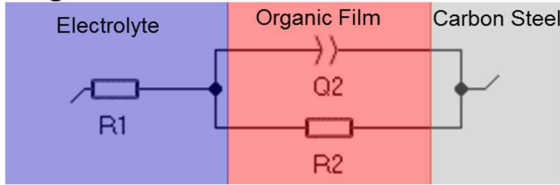
R_d , which has the similar definition as for Warburg impedance, can be used to calculate a diffusion coefficient for the mobile species. τ_d features the time it takes for the reactant to diffuse. The above expression is proposed because the sample we used takes place in the direction of diffusion occurring in cylindrical coordinate as shown in Figure 55.

Based on the suggested electrical equivalent circuit models, the results of fitting the experimental data are as illustrated in Figure 56. As shown in the figure, fitting results follow the experimental results well. In addition, the summary of equivalent values extracted through fitting can be confirmed on Table 16 to Table 20.

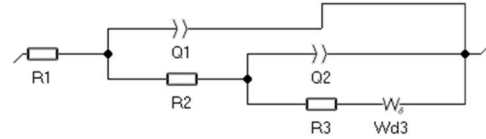
(a-1) Equivalent Circuit A (without oxide film) – initial degradation



(b-1) Equivalent Circuit A (without electrochemical reaction) – initial degradation



(a-2) Equivalent Circuit B (with oxide film)



(b-2) Equivalent Circuit B (with electrochemical reaction)

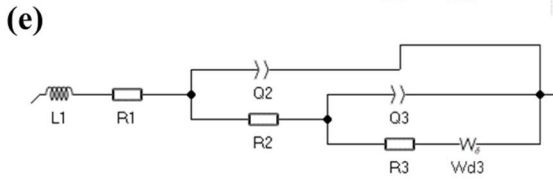
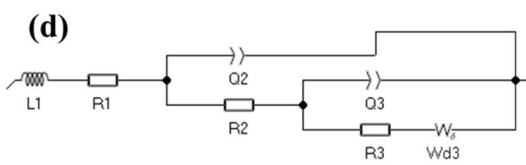
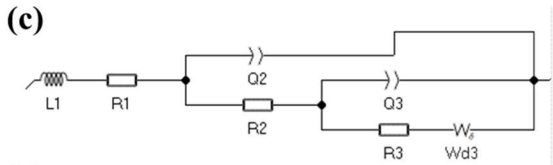
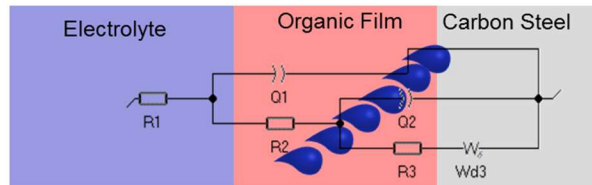
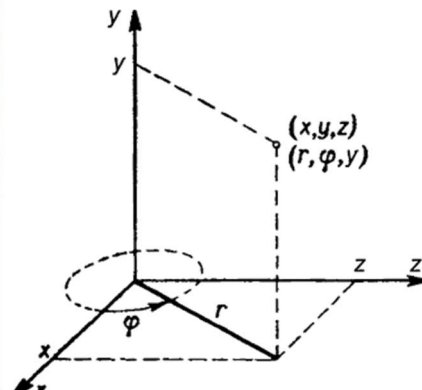


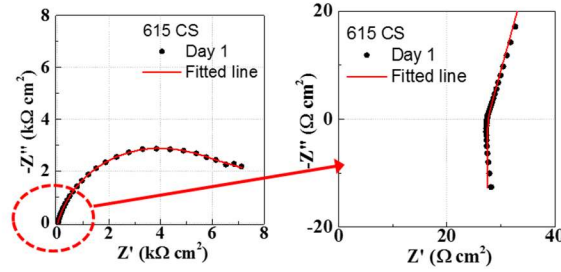
Figure 55. Equivalent circuit model for EIS spectra of the rebar specimens immersed in a simulated concrete pore solution: (a) 615 CS, (b) 1055 (, (c) 767, (d) 1035, (e)1094.



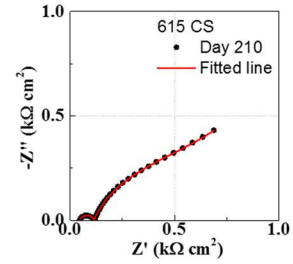
$$Z_{wa}(f) = R_d \frac{\tanh(\sqrt{\tau_d j 2\pi f})}{\sqrt{\tau_d j 2\pi f}}$$

Figure 56. Diffusion impedance for EIS spectra of the cylindrical rebar specimens immersed in a simulated concrete pore solution.

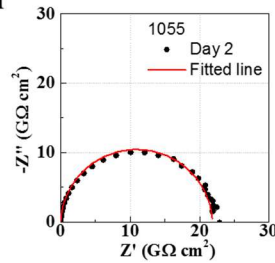
(a-1) Equivalent Circuit A (without oxide film) – initial degradation



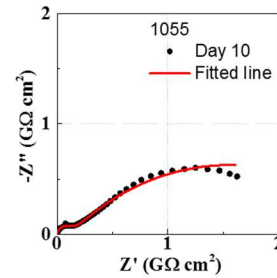
(a-2) Equivalent Circuit B (with oxide film)



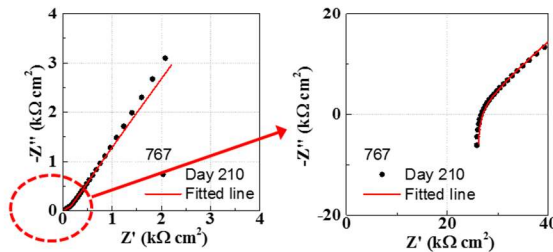
(b-1) Equivalent Circuit A (without electrochemical reaction) – initial degradation



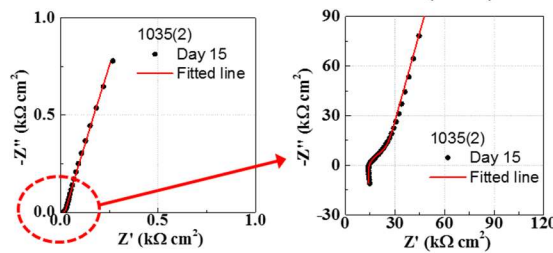
(b-2) Equivalent Circuit B (with electrochemical reaction)



(c)



(d)



(e)

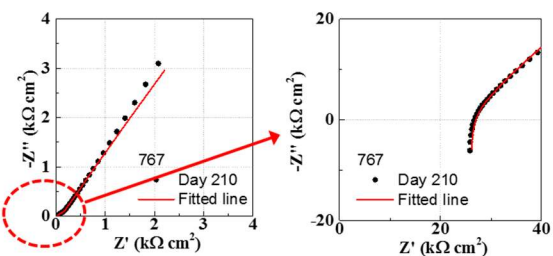


Figure 57. Fitted EIS spectra based on equivalent circuit model for the rebar specimens immersed in a simulated concrete pore solution: (a) 615 CS, (b) 1055 (CGR+Epoxy), (c) 797, (d) 1035, (e) 1094.

By using the extracted effective properties, the graphs in Figure 57 to Figure 63 describe how the systems changes over the immersed time. Figure 53 shows the change in electrochemical reaction

on 615 samples over the immersed time. As the charge transfer resistance decreases over time, it can be seen that reaction speed increases. As the CPE coefficient of double layer becomes smaller and smaller, it can be expected that the global system became heterogeneous due to the increase in the local damages of the system. R_d value related to the diffusion coefficient generally decreases over immersed time as you can see in Figure 58.

In the case of 1055 treated with organic coating, results who how important the initial formation condition of organic coating on the substrate is to prevent corrosion. As shown in sample 1 in Figure 59, there is no charge transfer phenomenon because the organic coating served as the appropriate barrier for the first three days of immersion. However, in the case of sample 2, electrolyte penetrates the coating through the pore network formed in the organic coating, and the electrochemical reaction can be occurred from the initial immersion. In addition, it can be confirmed that the difference in charge transfer resistance value is more than 1000 times as the electroactive surface area of sample 1 is smaller than that of sample 2 even after the electrolyte penetrates into sample 1.

The corrosion resistance performance is compared to 767, 1035, and 1094 samples, which have the surface treatment with different metallic coatings, in Figures 56~59. It can be seen that there is not much difference between the samples by considering the charge transfer phenomenon and the formation of film over immersed time under the given experiment conditions. The overall trend shows that the rate at which samples are degraded over immersed time increases. First, as shown in Figure 56, it can be seen that the value of the charge transfer resistance decreases slightly with immersed time. In addition, it can also be seen through the formation of film, which shows that the film resistance becomes smaller over immersed time and the CPE value of the film increases as shown in Figures 58 and 59. With little change in CPE coefficient α value, the increase in CPE value of film explains the thinning of the overall formed film's thickness in Figure 59.

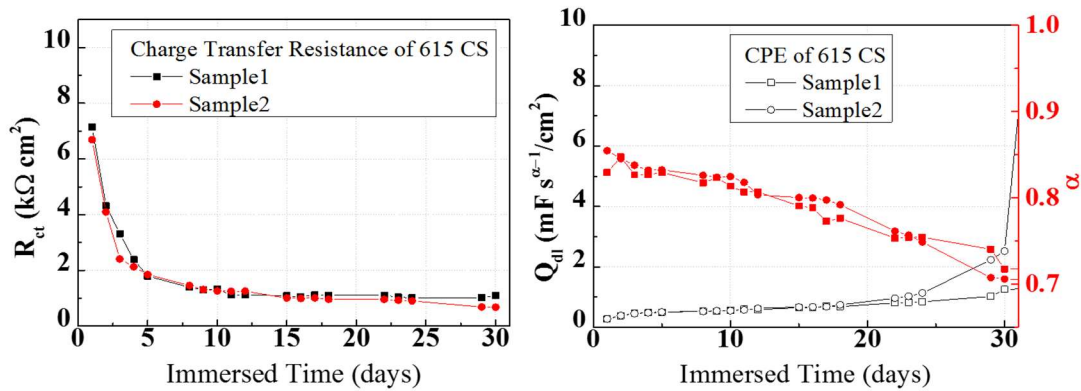


Figure 58. Charge transfer phenomenon vs immersed time for 615 cs rebar specimens immersed in a simulated concrete pore solution.

Table 16. 615 CS Samples and equivalent circuit values.

Sample #	DA Y	L1 (H cm ²)	R1(R_sol) (Ohm cm ²)	Q2(Q_dl) (F s ^{a-1} /cm ²)	a2	R2(R_ct) (Ohm cm ²)	Rd2 (Ohm cm ²)	td2 (s)
1	1	2.02121E-05	27.50064	0.000268632	0.8293	7148.64	2114.912	55.43
1	2	1.55481E-05	19.35984	0.000378538	0.8473	4316.32	2563.08	15.65
1	3	1.69685E-05	22.69248	0.000454245	0.8266	3316.952	3205.44	15.83
1	4	1.71805E-05	21.34416	0.000475708	0.8267	2382.456	3858.4	14.7
1	5	1.90461E-05	18.46096	0.000489623	0.8293	1794.792	4914.16	17.2
1	8	0.000014204	20.14424	0.000533019	0.8175	1389.872	4350.24	21.37
1	9	2.21582E-05	18.96976	0.00052217	0.8233	1300.408	4719.12	24.53
1	10	2.18445E-05	21.8572	0.000554481	0.8135	1317.792	4329.04	25.39
1	11	2.03605E-05	23.69312	0.000592689	0.8066	1118.512	4158.592	25.23
1	12	1.90079E-05	22.12432	0.000582075	0.8069	1121.056	4025.88	26.01
1	15	1.97584E-05	23.55744	0.000643396	0.7905	1086.712	3352.144	26.76
1	16	1.85966E-05	23.56592	0.000650472	0.7884	1050.248	3545.912	30.13
1	17	1.56244E-05	28.196	0.000696226	0.7728	1116.392	3549.304	31.79
1	18	1.85712E-05	27.04696	0.000678608	0.7763	1108.336	3261.408	30.82
1	22	1.50859E-05	29.41712	0.000804717	0.7532	1112.152	2828.504	30.46
1	23	1.58364E-05	29.24752	0.000823113	0.7543	1037.104	2868.36	30.82
1	24	0.000015052	28.52672	0.000841274	0.7543	1010.392	2703	29.9
1	29	1.5705E-05	29.6376	0.001017453	0.7403	1017.176	2408.744	34.58
1	30	1.36994E-05	32.76672	0.001250236	0.7174	1104.096	2004.672	34.97

Sample #	DA Y	R1(R_sol) (Ohm cm ²)	Q1 (Q_oxide) (F s ^{a-1} /cm ²)	a1	R2 (R_oxide) (Ohm cm ²)	Q2 (Q_dl) (F s ^{a-1} /cm ²)	a2	R3 (R_ct) (Ohm cm ²)
1	210	44.9016	5.76651E-06	0.7276	70.6808	0.004228774	0.7718	561.8
1	240	46.3432	5.97877E-06	0.7197	79.9664	0.004091981	0.7742	581.304

Sample #	DA Y	L1 (H cm ²)	R1 (R_sol) (Ohm cm ²)	Q2 (Q_dl) (F s ^{a-1} /cm ²)	a2	R2 (R_ct) (Ohm cm ²)	Rd2 (Ohm cm ²)	td2 (s)
2	1	2.15858E-05	18.43976	0.000271934	0.8547	6690.72	4753.04	209.2
2	2	2.50584E-05	21.34416	0.000382311	0.8454	4094.144	2229.392	12.09
2	3	2.62244E-05	18.55848	0.000451651	0.8378	2408.32	3472.136	13.58
2	4	2.1501E-05	20.2036	0.000475708	0.832	2130.6	4105.592	16.2
2	5	2.31334E-05	17.46032	0.000499764	0.8323	1851.184	4081.848	18.53
2	8	0.000020776	17.74016	0.000524057	0.8261	1453.472	4536.8	23.74
2	9	2.31377E-05	19.716	0.000540094	0.8238	1314.4	4757.28	27.84
2	10	2.45962E-05	18.66024	0.000545283	0.8246	1258.008	3794.8	24.04
2	11	2.38966E-05	19.398	0.000571698	0.8179	1249.104	3998.32	26.04
2	12	2.64915E-05	21.16184	0.000625943	0.8033	1252.072	3450.936	26.93

2	15	2.20692E-05	19.40648	0.000665094	0.8003	1004.032	3365.712	30.43
2	16	2.51093E-05	19.8432	0.000669811	0.7998	991.312	3372.496	30.4
2	17	2.16876E-05	20.59368	0.000677358	0.7974	1008.696	2753.456	26.98
2	18	2.05555E-05	19.1436	0.000740094	0.792	962.48	2402.384	24.35
2	22	1.76426E-05	21.45864	0.000957783	0.7612	958.24	2175.544	25.6
2	23	1.83422E-05	20.84808	0.001025472	0.7566	926.016	1964.816	25.9
2	24	1.72572E-05	21.12368	0.001128774	0.7486	900.152	1961.424	27.31
2	29	1.78462E-05	20.25872	0.002225943	0.7074	686.88	1486.968	28.31
2	30	1.77953E-05	19.36832	0.002518868	0.7057	677.128	1499.688	29.69
Sample #	DA Y	R1 (R_sol) (Ohm cm ²)	Q1 (Q_oxide) (F s ^{a-1} /cm ²)	a1	R2 (R_oxide) (Ohm cm ²)	Q2 (Q_dl) (F s ^{a-1} /cm ²)	a2	R3 (R_ct) (Ohm cm ²)
2	210	3.29914E-10	1.15142E-09	0.8187	1385.632	0.005419811	0.5593	1614.168
2	240	7.33096E-13	1.95401E-09	0.7826	1344.504	0.005549528	0.5604	1560.32

Table 17. 767 Samples and equivalent circuit values.

Sample #	DAY	L1 (H cm ²)	R1 (R_sol) (Ohm cm ²)	Q2 (Q_film) (F s ^{a-1} /cm ²)	a2	R2 (R_film) (Ohm cm ²)	Q3 (Q_dl) (F s ^{a-1} /cm ²)	a3	R3 (R_ct) (Ohm cm ²)	Rd3 (Ohm cm ²)	td3 (s)
1	1	1.77995E-05	14.54	3.33019E-05	0.87	32.084	2.2764E-05	0.187	8802.2	65253.6	63.01
1	2	1.88977E-05	15.83	0.000693396	0.83	227.77	0.00019519	0.909	20186.6	1.249E-07	12760000
1	3	1.86984E-05	14.3	0.000777594	0.83	165.1	0.00029127	0.89	25851.2	13902.96	74.5
1	4	1.71338E-05	14.78	0.001503302	0.81	74.53	0.00071769	0.963	14424.4	13207.6	0.01488
1	8	1.85924E-05	16.2	0.002220047	0.82	34.92	0.00259906	0.885	189.61	21551.92	5.881
1	9	0.000019504	15.7	1.20118E-05	0.86	14.02	0.00610849	0.545	139.83	0.1948704	6.97E-12
1	10	1.85458E-05	1.97	7.71934E-09	0.20	12.34	0.01534906	0.793	30.752	2809	6.4
1	11	1.85627E-05	13.68	0.003658019	0.83	3.94	0.0098467	0.817	307.27	9637.52	0.000964
1	12	1.74646E-05	14.96	0.004818396	0.82	4.307	0.01117689	0.819	61.09	38066.72	10.43
1	15	1.73628E-05	15.70	0.006757075	0.83	4.78	0.01139387	0.85	7.73	642.36	8.071
1	16	1.92454E-05	15.5	0.006683962	0.82	5.23	0.01396462	0.821	86.79	3.825E+17	25.69
1	17	1.82956E-05	15.3	0.006195755	0.81	6.90	0.01354717	0.812	193.59	2.313E+23	0.003418
1	18	1.91945E-05	15.4	0.006799528	0.79	8.56	0.01663915	0.856	23.04	761.504	9.89E-09
1	19	2.05089E-05	15.93	0.004981132	0.78	8.63	0.01568868	0.823	195.16	7.768E+16	7.48E-05
1	22	1.79988E-05	15.34	0.005959906	0.82	4.15	0.01574292	0.826	129.23	8.862E+20	3.33E-05
1	23	1.90291E-05	14.54	0.006790094	0.78	6.59	0.01664387	0.833	253.04	7.361E+16	5.54E-06
1	24	1.8143E-05	13.99	0.004622642	0.77	6.17	0.01762736	0.844	5.414	9.599E+17	426.8
1	25	1.95888E-05	13.68	0.007174528	0.83	4.25696	0.01479481	0.829	182.91	2.859E+16	4.66E-05
1	26	2.12636E-05	15.48	0.00496934	0.79	5.43144	0.01413915	0.875	2.3031	597.416	7.444
1	29	1.81218E-05	14.68312	0.008915094	0.8294	6.03776	0.01291981	0.816	40.40	1.316E+17	8.15E-08
1	30	1.96566E-05	16.83704	0.007198113	0.8349	6.63136	0.01488915	0.856	41.70	612.256	8E-15

1	210	1.08544E-05	25.25768	0.000584906	0.5365	225.1864	0.00091156	0.669	17.23	4.198E+18	0.00365
1	240	1.3657E-05	26.72896	0.000431132	0.5264	409.796	0.00084882	0.649	10.48	6.937E+20	500915

Sam ple #	DAY	L1 (H cm ²)	R1 (R_sol) (Ohm cm ²)	Q2 (Q_film) (F s ^{a-1} /cm ²)	a2	R2 (R_film) (Ohm cm ²)	Q3 (Q_dl) (F s ^{a-1} /cm ²)	a3	R3 (Rct) (Ohm cm ²)	Rd3 (Ohm cm ²)	td3 (s)
2	1	0.00001823	16.56	0.000577358	0.79	2686.46	2.8349E-05	0.50	27178.4	7.09352	0.3052
2	2	1.79818E-05	16.70	0.000545991	0.85	115.24	0.00030118	0.67	28806.56	1.879E-13	1809000
2	4	1.69303E-05	16.22	0.00176934	0.81	84.715	0.00115118	0.89	46555.2	3.136E-07	1.25E-11
2	5	1.89401E-05	17.17	0.001447642	0.82	75.04	0.00138797	0.85	50583.2	3.224E-24	6.28
2	11	1.86094E-05	16.14	0.001886085	0.77	54.017	0.00261321	0.83	1456.016	196736	14.58
2	12	1.67395E-05	16.1	0.001860849	0.72	100.23	0.00213844	0.75	77.0408	92050.4	2.01E-24
2	15	1.68413E-05	17.06	0.001983491	0.78	52.576	0.00319575	0.83	4233.216	2.943E+18	2.2E-191
2	16	1.89613E-05	16.02	0.0035	0.76	35.463	0.00466274	0.85	6890	16086.56	3.07
2	17	1.85627E-05	16.87	0.003589623	0.76	29.603	0.00729245	0.85	4290.88	6.36E+51	7.45E-05
2	19	1.90546E-05	17.163	0.003292453	0.77	29.497	0.00745991	0.85	5.813E-06	4.897E+11	16.32
2	23	1.7685E-05	16.76	0.003660377	0.77	30.968	0.00708726	0.85	14.57712	12160.32	19.9
2	25	1.95718E-05	16.7	0.00484434	0.74	26.516	0.00941509	0.84	3160.4	81747.2	2.21E-24
2	26	1.57813E-05	15.361	0.005563679	0.75	27.56	0.00835849	0.85	1860.93	29641.84	1E-24
2	29	2.55248E-05	9.099	0.002134198	0.72	30.28	0.00857783	0.77	914.992	1693.88	2.25E-14
2	30	1.45856E-05	18.299	0.005974057	0.73	31.3124	0.00895283	0.86	6.496E-08	8.412E+16	2.525
2	210	0.00001123	27.23	0.000686321	0.5	136.06	0.00137571	0.70	41.06	2.562E+18	44.36
2	240	1.27158E-05	28.26	0.000602358	0.51	238.24	0.00118137	0.71	278568	4.104E+18	6.806

Table 18. 1035 (2) Samples and equivalent circuit values.

Sample #	DAY	L1 (H cm ²)	R1 (R_sol) (Ohm cm ²)	Q2 (Q_film) (F s ^{a-1} /cm ²)	a2	R2 (R_film) (Ohm cm ²)	Q3 (Q_dl) (F s ^{a-1} /cm ²)	a3	R3 (R_ct) (Ohm cm ²)	Rd3 (Ohm cm ²)	td3 (s)
1	3	0.000015158	14.91	0.001163208	0.8103	15.92	0.00033797	0.89	18.76	26856.16	1.728
1	4	1.70575E-05	14.86	0.00240566	0.8003	54.1	0.00044009	0.9	33.05	1.54E+19	0.050
1	9	1.57558E-05	13.94	0.003591981	0.7934	37.15	0.00291745	0.89	236.33	54.6536	8.369
1	10	1.44923E-05	15.49	0.004063679	0.7801	39.26	0.00326651	0.89	306.55	40954.16	7.999
1	11	1.54209E-05	15.21	0.004035377	0.7764	34.97	0.00357547	0.88	25.21	103456	7.683
1	15	1.76045E-05	14.31	0.004924528	0.7462	22.5	0.00707075	0.87	22921.4	1803272	9.415
1	16	1.80242E-05	15.99	0.004235849	0.757	26.86	0.00582547	0.88	15.93	11303.84	13.32
1	17	1.74688E-05	14.5	0.014009434	0.6282	41.69	0.00805189	0.99	39.033	399.62	0.035
1	18	1.76002E-05	15.36	0.005561321	0.7382	28.45	0.00736792	0.87	8.52E-05	3.6E+17	0.0003
1	19	1.75706E-05	16.54	0.00729717	0.699	43.7	0.00569575	0.99	100.40	5495.04	0.017
1	23	1.88722E-05	14.2	0.005858491	0.7281	26.4	0.00810377	0.88	8.46E-05	3.994+14	2E-08
1	24	2.00756E-05	15.73	0.007334906	0.6723	41.7	0.00543868	0.98	452.83	916.688	5E-07

1	25	1.74349E-05	15.3	0.005658019	0.7045	24.0	0.0095967	0.90	1510.71	41.16192	1.537
1	26	1.62689E-05	15.06	0.007075472	0.7098	25.40	0.00862736	0.91	851.39	150.9016	0.055
1	29	0.000013674	15.4	0.004735849	0.7007	21.36	0.00936792	0.94	2.44690	1118.512	9.692

Sample #	DAY	L1 (H cm ²)	R1 (R_sol) (Ohm cm ²)	Q2 (Q_film) (F s ^{a-1} /cm ²)	a2	R2 (R_film) (Ohm cm ²)	Q3 (Q_dl) (F s ^{a-1} /cm ²)	a3	R3 (R_ct) (Ohm cm ²)	Rd3 (Ohm cm ²)	td3 (s)
2	1	1.51877E-05	13.462	0.00013017	0.85	37.51976	0.00124575	0.30	477.42	39.27088	1.337
2	3	0	12.999	0.0018184	0.79	25.91064	0.00062241	1	51431.2	687.304	13971
2	5	1.49206E-05	14.38	0.00184434	0.81	26.86888	0.00182736	0.87	349.41	37591.84	4.599
2	9	1.52767E-05	13.81	0.00381368	0.78	21.21696	0.00458255	0.84	144.541	12283.28	13.78
2	10	1.61502E-05	13.90	0.00382547	0.78	25.228	0.00442925	0.87	257.66	11240.24	10.82
2	15	1.81811E-05	13.39	0.00420047	0.74	25.74528	0.00532075	0.86	53.21	4829.36	9.352
2	19	1.80582E-05	16.06	0.00412736	0.74	23.96872	0.00634198	0.85	55.20	6423.6	12.31
2	23	1.90842E-05	13.05	0.00356132	0.73	22.65008	0.00607311	0.86	31.320	2751.76	9.25
2	24	1.82066E-05	11.84	0.00414151	0.75	25.18136	0.00608962	0.8	52.70	4524.08	10.87
2	25	1.74094E-05	15.50	0.0040566	0.72	26.16504	0.006	0.86	59.57	2154.768	8.093
2	26	1.64512E-05	15.21	0.00440566	0.73	26.61448	0.00566981	0.87	23.718	2538.064	8.817
2	29	1.45093E-05	15.79	0.00422406	0.73	28.48008	0.00523113	0.87	23.341	4655.52	10.26
2	30	1.45983E-05	16.74	0.00433962	0.72	31.53712	0.00440566	0.89	4.566	1982.2	7.783

Table 19. 1055 Samples and equivalent circuit values.

Sample #	DAY	R1 (R_sol) (Ohm cm ²)	Q2 (Q_film) (F s ^{a-1} /cm ²)	a2	R2 (R_film) (Ohm cm ²)	Q3 (Q_dl) (F s ^{a-1} /cm ²)	a3	R3 (R_ct) (Ohm cm ²)	Rd3 (Ohm cm ²)	td3 (s)
1	1	3.7223E-10	N/A	N/A	N/A	1.491E-11	0.9728	1.575E+11	N/A	N/A
1	2	1.02269E-10	N/A	N/A	N/A	1.54E-11	0.9729	2.185E+10	N/A	N/A
1	3	7.4412E-10	N/A	N/A	N/A	2.044E-11	0.9485	1.053E+10	N/A	N/A
1	4	6.6441E-157	1.444E-11	0.9823	0.0022654	1.12E-10	0.05704	205088800	2.146E+10	1.721
1	5	0.689848	1.481E-11	0.9799	305152800	1.757E-10	0.4885	7.267E+09	374731.2	11759
1	8	0.443928	1.442E-11	0.9834	73564000	4.035E-10	0.2086	87556000	4.715E+09	10.73
1	9	0.1525552	1.467E-11	0.9827	78524800	5.63E-10	0.3069	95527200	3.739E+09	9.392
1	10	3.10834E-10	1.505E-11	0.9811	79203200	6.613E-10	0.2862	71359200	3.216E+09	10.95
1	11	4.14714E-09	1.206E-10	1	0.0001157	6.705E-10	0.317	283274400	2.519E+09	13.18
1	12	2954.008	1.245E-11	0.997	4.545E-09	1.071E-09	0.2724	391097600	3.537E+09	13.26
1	15	5613.76	1.23E-11	1	33757481	1.875E-09	0.3306	401316000	2.3E+09	15.58
1	16	7.25464E-07	1.553E-11	0.9794	63642400	2.297E-09	0.402	365276000	1.604E+09	14.07
1	17	2.46938E-06	1.568E-11	0.9799	55459200	2.287E-09	0.3464	256774400	2.102E+09	19.92
1	18	3.39158E-06	1.513E-11	0.9825	27560000	1.76E-09	0.2952	276702400	2.081E+09	26.61

1	19	1.51029E-09	1.588E-11	0.9792	31171038	1.928E-09	0.4327	333306400	625824000	20.09
1	22	1.22663E-09	1.588E-11	0.9792	31171038	1.928E-09	0.4327	333306400	625824000	20.09
1	23	3.82957E-09	1.608E-11	0.9788	31517150	2.252E-09	0.4225	386433600	459192000	16.7
1	24	0.00018952	1.565E-11	0.9811	21821542	2.658E-09	0.3903	384228800	342888800	18.97
1	29	9.06088E-05	1.614E-11	0.9789	15246234	2.38E-09	0.4247	235574400	198898400	27.4
1	30	8.55208E-05	1.672E-11	0.9766	16949824	4.646E-09	0.429	247616000	222388000	34.9

Sample #	DA Y	R1 (R_sol) (Ohm cm ²)	Q2 (Q_film) (F s ^{a-1} /cm ²)	a2	R2 (R_film) (Ohm cm ²)	Q3 (Q_dl) (F s ^{a-1} /cm ²)	a3	R3 (R_ct) (Ohm cm ²)	Rd3 (Ohm cm ²)	td3 (s)
3	1	14564.4	2.333E-08	0.55	778803.2	1.814E-09	0.99	151028.8	180284800	0.5375
3	2	26449.12	1.071E-07	0.49	3766264.8	1.781E-08	1	47572.8	443928000	0.3749
3	16	25397.6	2.717E-08	0.59	46809.6	9.915E-08	0.69	744925.6	53084800	0.733
3	17	8.5182E-13	4.255E-11	0.92	42442.4	3.663E-08	0.61	454443.2	38026270	46.22
3	18	157.0072	2.091E-09	0.63	78991.2	7.601E-08	0.53	1612641.6	68900000	1.877
3	22	3.85077E-28	1.27E-11	1	53551.2	6.96E-08	0.522	2198228	106212000	5.028
3	29	2.32564E-06	4.851E-08	0.43	38164.24	2.071E-07	0.68	1162226.4	57833600	0.2534
3	30	5.35512E-21	2.58E-08	0.48	44986.4	3.491E-07	0.64	1180246.4	75980800	2.289

Table 20. 1094 Samples and equivalent circuit values.

Sample #	DAY	L1 (H cm ²)	R1 (R_sol) (Ohm cm ²)	Q2 (Q_film) (F s ^{a-1} /cm ²)	a2	R2 (R_film) (Ohm cm ²)	Q3 (Q_dl) (F s ^{a-1} /cm ²)	a3	R3 (R_ct) (Ohm cm ²)	Rd3 (Ohm cm ²)	td3 (s)
1	2	1.50732E-05	16.67	0.00047712	0.8	6.75008	0.00056769	0.92	43.2	575664.8	3665
1	3	1.22409E-05	14.19	0.00062524	0.88	7.8016	0.00095165	0.86	78.3	21395.04	0.00022
1	4	1.53191E-05	14.94	0.00074387	0.86	29.92168	0.00050613	0.87	50.41	11944.08	4.414
1	5	1.33899E-05	14.65	0.00140165	0.85	13.1864	0.00170613	0.85	43.5	24753.12	3.431
1	8	1.15328E-05	15.43	0.0018342	0.80	38.64336	0.00153325	0.88	43.8	20542.8	6.207
1	9	1.42125E-05	15.72	0.00214882	0.81	27.54728	0.00235401	0.87	43.7	19902.56	6.098
1	10	1.41234E-05	12.34	0.00176981	0.77	53.8056	0.00137075	0.89	42.56	18541.52	7.15
1	11	1.11173E-05	13.47	0.00245047	0.79	21.5392	0.00329717	0.86	44.39	15488.72	7.19
1	12	1.34281E-05	15.60	0.00258726	0.77	24.46056	0.00318632	0.85	44.01	10557.6	6.02
1	15	1.73755E-05	19.78	0.00290566	0.7	20.27992	0.00485142	0.85	175.87	15480.24	7.458
1	16	1.48612E-05	14.39	0.0030967	0.77	19.57184	0.00507311	0.86	128.38	12334.16	7.975
1	17	1.24062E-05	13.70	0.00328774	0.75	19.42768	0.00499292	0.86	88.78	8340.08	5.921
1	18	0.00001409	15.2	0.00316038	0.76	22.0056	0.00519104	0.87	193.42	20381.68	9.158
1	22	1.54082E-05	14.4	0.00378538	0.76	16.55296	0.00683019	0.86	71.52	7017.2	9.367

1	23	1.56668E-05	15.7	0.00379717	0.7	18.9528	0.00651651	0.87	99.38	10731.44	8.452
1	24	1.67395E-05	13.4	0.00353066	0.76	14.57288	0.007	0.85	49.56	17498.48	9.234
1	29	1.59466E-05	14.39	0.00366745	0.75	13.1864	0.00667217	0.84	43.75	3710.42	8.766
1	30	1.54802E-05	15.4	0.00344104	0.75	14.27608	0.00637736	0.84	43.62	4166.22	8.144

Sample #	DAY	L1 (H cm ²)	R1 (R_sol) (Ohm cm ²)	Q2 (Q_film) (F s ^{a-1} /cm ²)	a2	R2 (R_film) (Ohm cm ²)	Q3 (Q_dl) (F s ^{a-1} /cm ²)	a3	R3 (R_ct) (Ohm cm ²)	Rd3 (Ohm cm ²)	td3 (s)
2	1	1.80115E-05	12.351	0.00168774	0.69	57.45	0.0001629	1	267.20	31.1470	10.47
2	2	1.48909E-05	15.62	0.0006842	0.83	8.56	0.0005610	0.92	24926.	54.5264	1.625
2	3	1.39199E-05	15.531	0.0004717	0.89	10.93	0.0005969	0.87	260.6	16039.9	6.831
2	5	0.000015052	14.865	0.00129505	0.84	10.52	0.0023797	0.83	142.97	25414.5	4.316
2	11	1.28345E-05	13.160	0.00247642	0.77	22.34	0.0037075	0.81	186.09	10807.76	9.328
2	15	1.66886E-05	14.755	0.00275708	0.74	30.90	0.0039080	0.82	268.30	16866.72	11.54
2	16	1.38521E-05	13.190	0.00306368	0.73	20.49	0.0056297	0.79	304.47	13110.08	7.925
2	17	1.49121E-05	16.599	0.00248585	0.73	23.76	0.0040896	0.82	42.56	2809	9.394
2	23	1.71635E-05	16.586	0.0031816	0.75	16.42	0.0069528	0.83	49.73	3813.456	9.943
2	24	1.76384E-05	14.568	0.00323821	0.74	16.10	0.0066391	0.83	48.42	3296.176	9.453
2	29	1.77868E-05	12.571	0.00366038	0.73	15.80	0.0075353	0.82	213.65	14547.44	11.22
2	30	1.74476E-05	15.836	0.00378302	0.74	15.85	0.0074599	0.82	8.577	7152.88	12.2

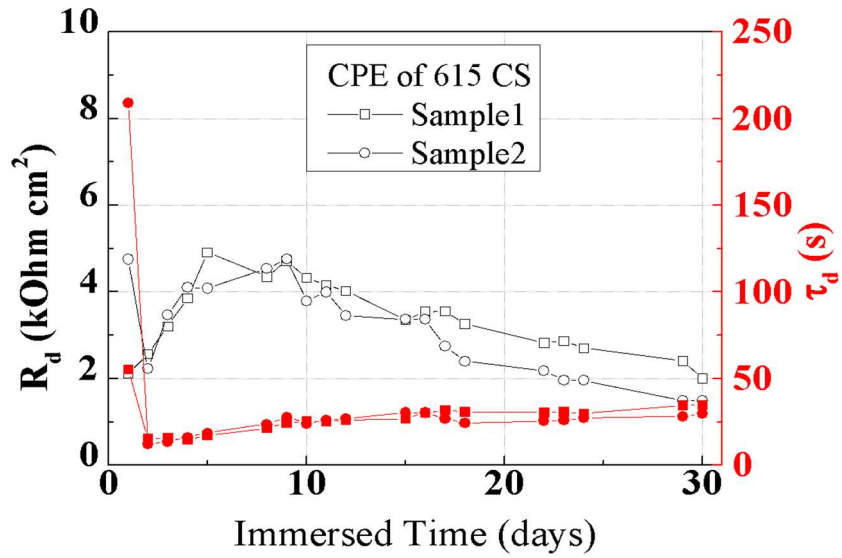


Figure 59. Diffusion phenomenon vs immersed time for 615 cs rebar specimens immersed in a simulated concrete pore solution.

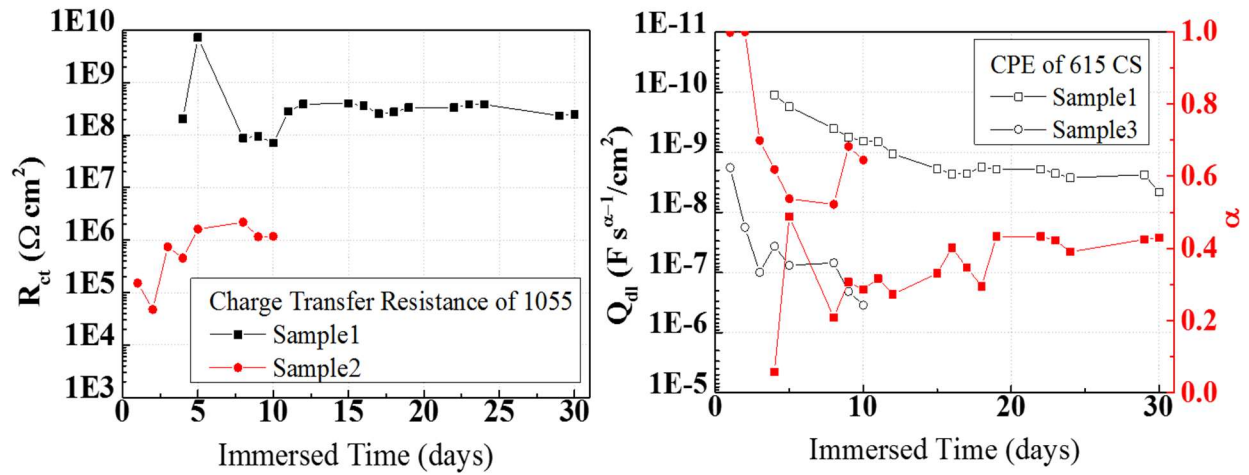


Figure 60. Charge transfer phenomenon vs immersed time for 1055 rebar specimens immersed in a simulated concrete pore solution.

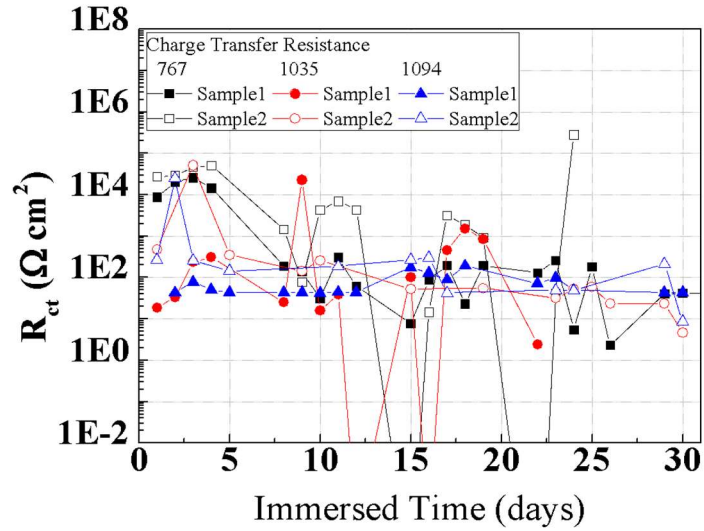


Figure 61. Charge transfer resistance vs immersed time for 767, 1035, and 1094 rebar specimens immersed in a simulated concrete pore solution.

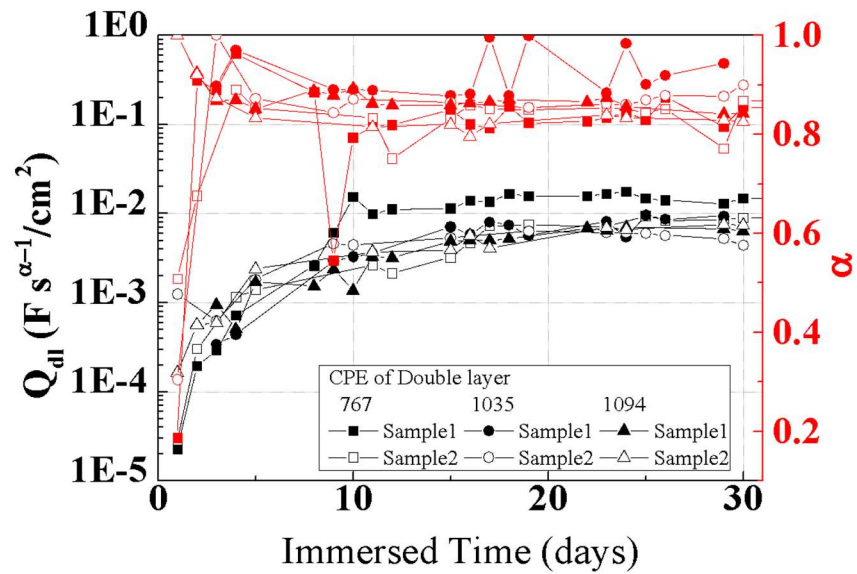


Figure 62. CPE of double layer phenomenon vs immersed time for 767, 1035, and 1094 rebar specimens immersed in a simulated concrete pore solution.

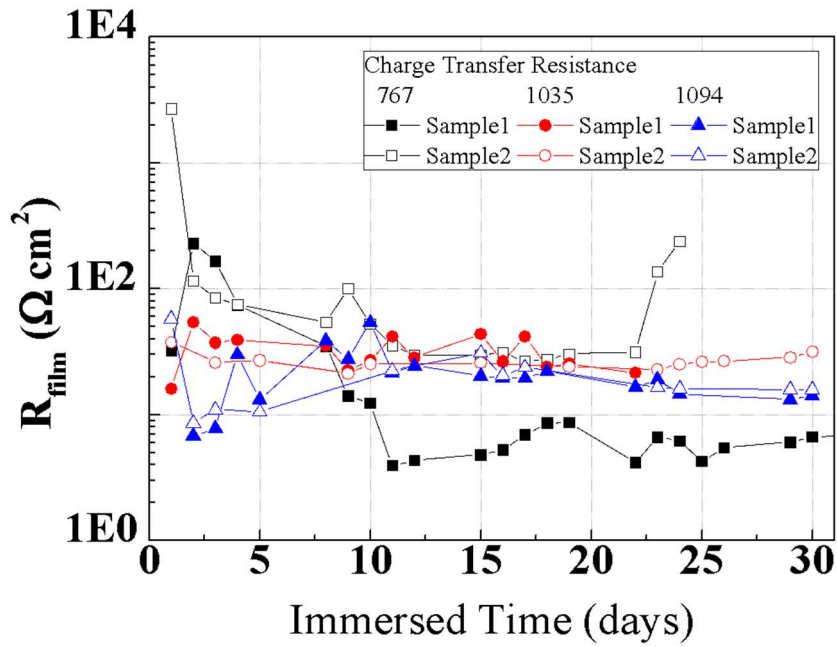


Figure 63. Film resistance vs immersed time for 767,1035, and 1094 rebar specimens immersed in a simulated concrete pore solution.

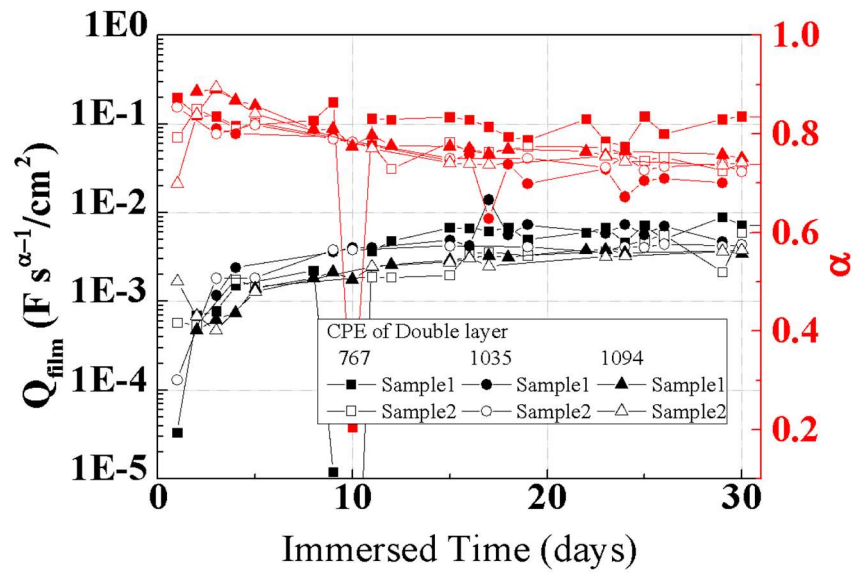


Figure 64. CPE of film vs immersed time for 767, 1035, and 1094 rebar specimens immersed in a simulated concrete pore solution.

5. RESULTS AND FINDINGS

Task 3: Develop a procedure for tracking the performance of control actions used in reinforced concrete bridge elements by comparing the current methods

5.1. Corrosion Propagation Model: Based on mechanistic analysis of damage evolution

Different works have shown the approach of probabilistic modeling based on a semi-empirical correlation; the expression comes from parameters associated with the degradation mechanisms. The most common expression is based on mass transfer or diffusion expression (Fick's Law), the corrosion or degradation have been included several parameters based on the conditions of the concrete and also the mass transfer mechanism. In this work we are building expressions for charge transfer expressions based on the characteristics of the interface steel/electrolyte or steel/Zn/electrolyte. The following are transfer functions that are obtained from the experimental results with time for different rebar conditions. The charge transfer or R_{ct} is inversely proportional of corrosion current and corrosion rate. The expressions for R_{ct} for 615 bare steel rebar with oxide film, 1055 and the galvanized rebars (767, 1094, 1035) are shown in equations 30-32.

$$R_{ct}(t) = \frac{1}{\frac{1}{|z| - R_1 - Q_1(j\omega)^{a_1}} - R_2 - Q_2(j\omega)^{a_2} - R_{d3}\sqrt{j\omega}} \quad [30]$$

$$R_{ct} = \frac{1}{\frac{1}{|z| - R_1 - Q_1(j\omega)^{a_1}} - R_2 - Q_2(j\omega)^{a_2} - R_{d3}\sqrt{j\omega}} \quad [31]$$

$$R_{ct} = \frac{1}{\frac{1}{|z| - R_1 - j\omega L_1 - Q_2(j\omega)^{a_2}} - R_2 - Q_3(j\omega)^{a_3} - R_{d3}\sqrt{j\omega}} \quad [32]$$

The corrosion current is obtained by following the Tafel expression and Stern and Geary classic analysis to express the corrosion rate, where the R_{ct} is the charge transfer resistance, R_{ct} . The proportionality constant V for a particular system, in this case the steel rebar in cement electrolyte (RC element or pore solution simulation) or can be expressed in terms of the Tafel slopes (characterized and quantified experimentally for the steel/electrolyte and the Zn/electrolyte systems).

$$i_{corr}(t) = \frac{V}{R_{ct}(t)} \quad [33]$$

$$V = \frac{\beta_a \beta_c}{2.3(\beta_a + \beta_c)} \quad [34]$$

Where β_a and β_c are the Tafel anodic and cathodic slopes respectively. The quantification is in terms of parameters that are characterized by electrochemical methods instead of metal loss or nondestructive evaluation methods. Both of the procedures only sense the potential metal wall thickness leading to the loss of capacity of the rebar with time. Electrochemical parameters

evidence the damage evolution at the interface by characterizing the mechanisms and also the properties of the corrosion products, the mass or charge transfer mechanism and parameters that can be used in the deterministic or probabilistic modeling. The expressions for different control actions based on the rebar approach are illustrated the Figure 65 where the stages are different based on the classical bare steel with the initiation and chloride threshold activation stage leading the propagation conditions. The figure reveals different slopes in terms of the damage at the steel surface, while Figure 65(b) denotes different stages and also durability by adding the control action in terms of the rebar. The galvanized rebar initiates the degradation process and once the electrolyte without any specific chloride content will affect the inorganic coating layer, this latter will form corrosion products that the electrochemical technique was able to capture. When the electrolyte reached the surface of the steel rebar, the stage change will be either same, slower or faster that the propagation stage by the bare rebar. The corrosion products will influence in the theoretical or data driven calculation in terms of mechanical approach by adding not only the loss of capacity but also higher loading conditions. Because the more volume accumulation in the steel rebar samples the implication of stresses are higher than the zinc corrosion products. The magnitudes for corrosion products are included as parameter for the corrosion rate or current corrosion estimations.

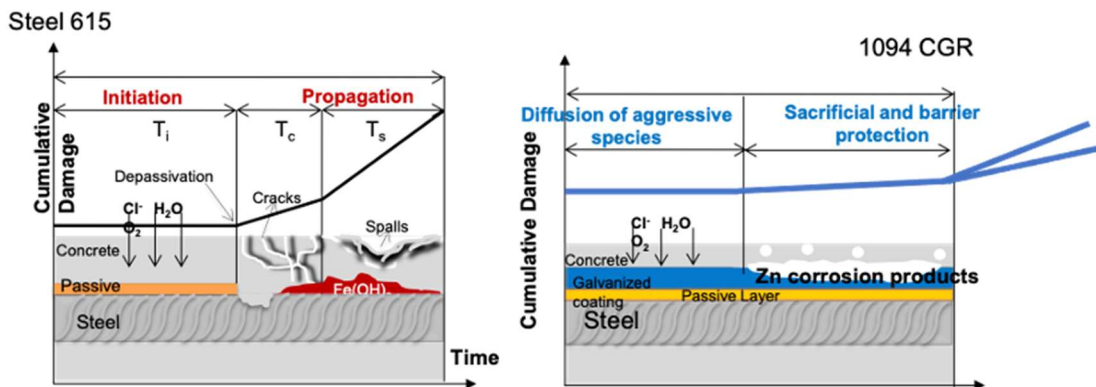


Figure 65. Damage evolution of the loss of capacity and or increase in the loading conditions when the propagation stage dominates the process.

Review Inspection Capabilities: there are different methods, techniques and tools available to measure corrosion rates or characterize corrosion. The technologies used on this work includes electrochemical methods, deterministic and non-deterministic analysis. Nondestructive evaluation is also other possibility for this current project for the field measurement. We also test this NDE in the laboratory to monitor and follow the state of the rebar in terms of metal loss, the technologies we use were GCorrTM and GiatecTM. There is other NDE that can follow the stage of the rebar but in terms of corrosion assessment we include the ones we can link with the corrosion mechanisms. The laboratory techniques can also be use in field measurements with the proper accessories and implementations, making a good option for the use of modeling in a more robust and reliable platform.

Table 21. Some examples of evaluation of NDE technologies used in the laboratory and in the field.

NDE Techniques	Applications	Limitations
Gecor (polarization technique)	<ul style="list-style-type: none"> • Field measurements • rebar corrosion rate • reliability of the structure based on metallic degradation 	<ul style="list-style-type: none"> • Might be difficult to read a rebar network • hard to use in difficult access areas • You need electrical access to the rebar
Giatic (polarization technique)	<ul style="list-style-type: none"> • rebar corrosion rate • Non-intrusive wireless capabilities • It can follow the network and the rebar distribution 	<ul style="list-style-type: none"> • Need to have expertise to rely on the results • Need to have battery supply
Potentiostatic and galvanostatic EIS	<ul style="list-style-type: none"> • rebar corrosion rate • reliability of the structure based on metallic degradation 	<ul style="list-style-type: none"> • Might be difficult to read a rebar network • hard to use in difficult access areas

Ultrasound and thermo based techniques can have some parameters associated to corrosion rate but the metal loss should be validated and characterize accordingly. The unification of several techniques can be another course of action. Combination of electrochemical/NDE will be the approach to take for the corrosion assessment, reliability modeling and Corrosion Management.

In Depth Corrosion Assessment: Following the field or laboratory characterization, the results should be analyzed based on the parameters considered for the corrosion mechanism with different corrosion control actions presented. The addition of a coating (inorganic and organic) on the surface of the rebar extends the stages of the damage resulting in a reliable and viable option for long term durability. Galvanized systems also have illustrated the second and following stages, where the activation will produce less volumetric corrosion products and potential migration of the products to the concrete matrix feasible to have more robust system and more reliable system. The corrosion assessment also considered two different routes for degradation, the general corrosion and local attack. The first can be approach by electrochemical methods or non-destructive evaluation techniques, the second represents highest threat for engineering assets. In this work we developed a reliable model in terms of local attack conditions and previously we developed a reliability model based on general corrosion.

Rating based on Macroconditions and micro-conditions factors and for corrosion assessment (Corrosion Index): the first part of this work we proposed the environmental critical factors that include different levels of impact in the corrosion mechanism. The corrosion index can be defined based on the degradation mechanism, and the corrosion precursors. Table 1 exhibits the parameters and the range of magnitudes that consider the levels of corrosion parameter in the mechanism. The index is based on different levels of influence in the corrosion mechanism. The ranking or index based on the control action is also considered based on the steady state response of steel/electrolyte, steel/Zn/electrolyte and steel/Zn/Epoxy/electrolyte systems. The galvanized systems resulted in a higher ranking than traditional bare steel systems by following different stages in the degradation

processes. Finally, the ranking or index for the RC elements can be interpreted based on the corrosion control actions implements from the initial conditions. The galvanized systems observe in short- and medium-term higher impedance properties, however we suggest more exposure time to validate the following stages. The local attack conditions can be implemented to have a different index due to the nature of the damage evolution when a local condition exist, the randomness should be implemented, and maybe different mechanism of corrosion can cover this process. This latest ranking considered the durability based on each stage of the damage evolution dynamics.

Preliminary Summary of Repair and Corrosion Control Methods: There are different repair methods for reinforced concrete structures reported previously. Following a specific index or number, the repair method used can be correlated with the proposed index. We give an example of used repair methods and corrosion control methods in Table 22. One way of classifying the repair methods, according to Yehia et al. (29) could be categorizing them in two different categories: protective methods (e.g., grouting, sealing, overlay, injection) and the second classification is non-protective methods (e.g., overlay, patching, sealing).

Table 22. Repair and corrosion control methods.

Repair Principle	Repair name	Description	Comment
Physical	Patching	<ul style="list-style-type: none"> • epoxy injection • flood with corrosion inhibitor • surface application of corrosion inhibitor • recoating exposed steel • patching with admixed corrosion inhibitors <p>combine the methods</p>	<ul style="list-style-type: none"> • the designer's responsibility to evaluate the repair areas and determine the most suitable repair method; • a cheap way to repair local damage; • not completely waterproof. It may be a temporary remedy to the problem, but it may further deteriorate the problem
Electrochemical	Cathodic Protection	<ul style="list-style-type: none"> • achieved by supplying an external source of current to counteract the internal corrosion current • can be applied to new construction and rehabilitation 	FHWA has stated that cathodic protection is the only rehabilitation technique that has proven to stop corrosion in salt-contaminated bridge decks regardless of
Electrochemical	Cathodic Protection	<ul style="list-style-type: none"> • achieved by supplying an external source of current to counteract the 	FHWA has stated that cathodic protection is the only rehabilitation technique that has proven

		<p>internal corrosion current</p> <ul style="list-style-type: none"> • can be applied to new construction and rehabilitation 	<p>to stop corrosion in salt-contaminated bridge decks regardless of</p>
Electrochemical	Cathodic Protection	<ul style="list-style-type: none"> • achieved by supplying an external source of current to counteract the internal corrosion current • can be applied to new construction and rehabilitation 	<p>FHWA has stated that cathodic protection is the only rehabilitation technique that has proven to stop corrosion in salt-contaminated bridge decks regardless of</p>

Remaining Life Models based on Reliability: Figure 66 demonstrated how the proposed framework can be used to choose between rehabilitation alternatives and form a continuous optimization cycle (see Figure 66). The goal of any repair method is to ensure the structural integrity of the structure under normal operating conditions. Two repair alternatives, Repair #1 and Repair #2, restore the reliability index to its initial value before the onset of corrosion. The difference between these two methods is that Repair #1 does little to reduce the rate of corrosion, which results in a service life of slightly over 50 years. Conversely, Repair #2 slows the degradation rate, which results in a service life of about 60 years. Reducing the degradation rate can be achieved using different methods. For example, Fiber Reinforced Polymer wrapping of RC beams is known to deprive the corrosion cell of oxygen, which results in slower corrosion rates. Nevertheless, the achieved service is still below what an owner might desire (e.g., 75 years). To achieve a longer design life, Figure 66 shows that a higher initial reliability index, β , will be needed for the same corrosion rate as that resulting from Repair #2. This is the case for Repair #3, for which the initial β after repair is increased, which adds about 5 years of service life over Repair #2 alternative.

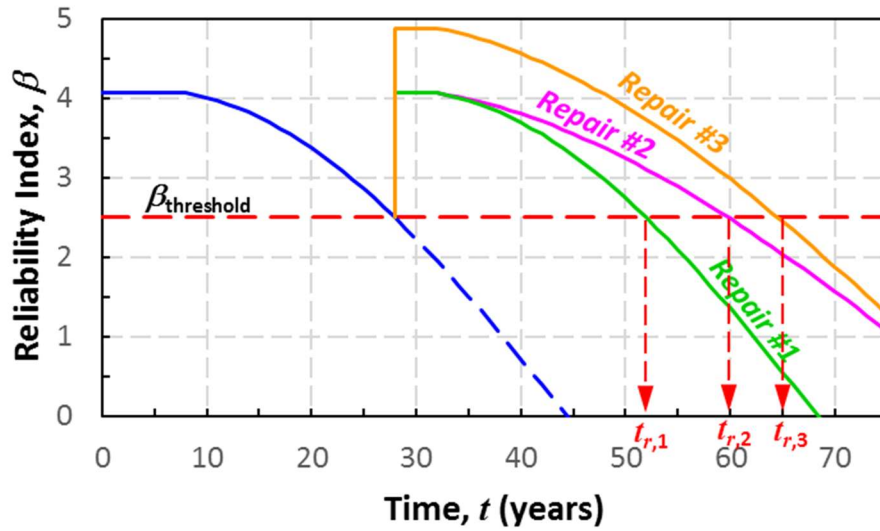


Figure 66. Effect of different intervention strategies on expected service life

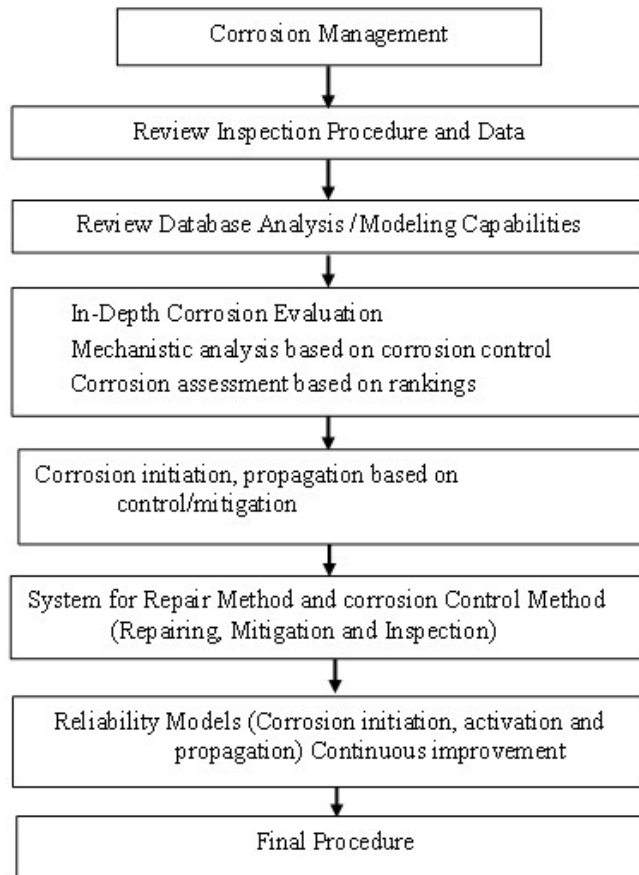


Figure 68. Steps for different intervention strategies on corrosion Management

Case study

Due to the current circumstances, we have not been able to perform field work, the initial plan included a visit to perform monitoring of several parameters that will help to validate the current proposed model and also the performance of different bridges. During the monitoring of several parameters illustrated in Table 23, we will be able to validate several steps in the corrosion management methodology. Figure 67 shows the bridge containing Galvanized rebar as a reinforcement. The system was built in 2018 additionally the plan was to select one bridge with the same age and built by bare steel.

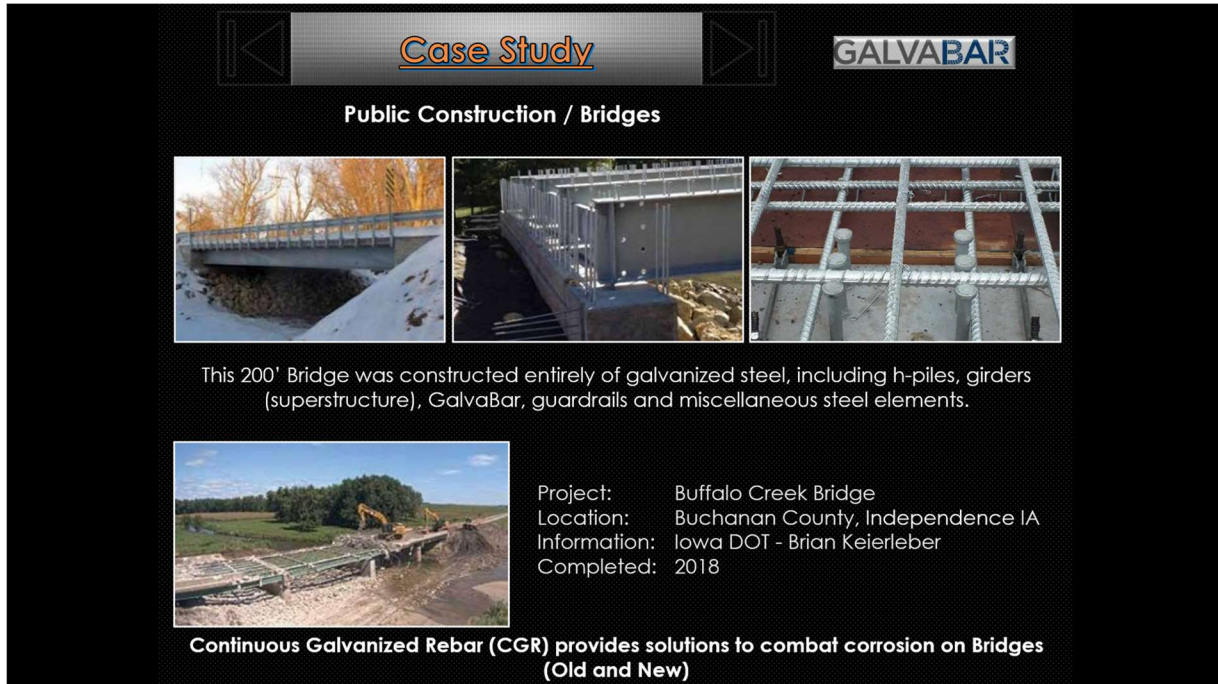


Figure 67. Bridges made with galvanized steel rebar.

Table 23. Parameters considered for the study.

Parameter	Precip.	Temp.	Chloride Content	Humidity Relative	Deicing	CO ₂
Location	Macro conditions	Macro conditions	Macro-Micro-condition	Macro conditions	Macro conditions	Macro conditions
OCP	Indirect Influence	Influence	Influence	Indirect Influence	Indirect Influence	Influence
Corrosion rate	Influence	Influence	Influence Localized	Indirect Influence	Indirect influence	Influence
pH	Indirect influence	Influence	Indirect Influence	NA	NA	Influence
Resistivity	Influence	NA	Influence	Indirect influence	Indirect Influence	NA

6. CONCLUSIONS

In this study, a corrosion management procedure framework can be implemented by characterizing and quantifying the damage evolution of an RC system. Different stages are proposed for a classic bare steel and galvanized steel, the second as a control action. The damage evolution follows different paths. Deterministic and probabilistic models can be able to characterize the reliability of the RC system and compare the difference when a control action is implemented at the initial point. Figure 68 illustrates the concept of corrosion management for an RC element based on the in-depth mechanistic analysis and control action with the rebar.

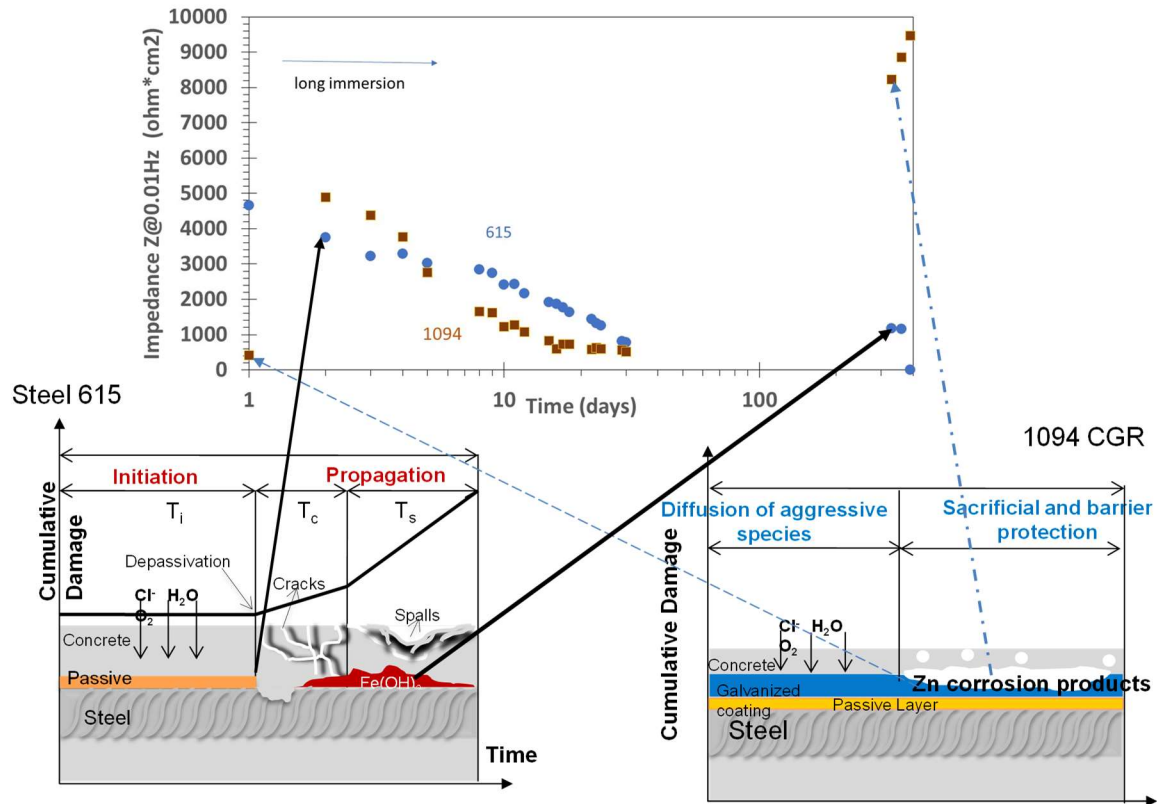


Figure 68. Stages of rebar degradation correlated with observed impedance values.

The localized model is a more realistic approach for the reliability assessment, however the combination of both should be implemented, general corrosion and localized attack could be the next step for the reliability assessment.

The preliminary framework is based on corrosion assessment by considering the damage evolution as the main threat. The loss of capacity is considered to be attributed mainly to corrosion in this corrosion management set of steps. A flow diagram is proposed to follow up with the implementation and further research in this topic. The proposed framework can be converted in a procedure or methodology.

REFERENCES

1. Tuutti, K. (1982). Corrosion of steel in concrete. Swedish Cement and Concrete Research Institute, Stockholm. <http://www.cbi.se/viewNavMenu.do?menuID=317&oid=857>
2. Yeomans SR, 2019, 'Galvanized reinforcement in bridge and coastal construction', in 20th Congress of IABSE, New York City 2019: The Evolving Metropolis - Report, New York City, pp. 1592 - 1598, presented at 20th Congress of the International Association for Bridge and Structural Engineering (IABSE 2019) The Evolving Metropolis, New York City, 04 September 2019
3. Kim, C., Choe, D.-E., Castro-Borges, P., & Castaneda, H. (2020). *Probabilistic Corrosion Initiation Model for Coastal Concrete Structures*. *Corrosion and Materials Degradation*, 1(3), 328–344. doi:10.3390/cmd1030016
4. Grubb, J.A., H.S. Limaye, and A.M. Kakade, *Testing pH of Concrete*. Concrete International, 2007. 29(4).
5. Angst, U.M., et al., *Chloride Induced reinforcement corrosion: electrochemical monitoring of initiation stage and chloride threshold values*. Corrosion Science, 2011. 53(4): p. 1451-1464.
6. Alonso, C., et al., Chloride threshold values to depassivate reinforcing bars embedded in a standardized OPC mortar. Cement and Concrete research, 2000. 30(7): p. 1047-1055.
7. Broomfield, J.P., *Corrosion of steel in concrete: Understanding, investigation and repair*. 2007, London: Taylor & Francis.
8. Yeomans, Stephen. (2004). Galvanized Steel Reinforcement in Concrete: An Overview.
9. Virmani, Y.P. and G.G. Clemena, *Corrosion protection: Concrete bridges*. 1998, United States. Federal Highway Administration.
10. F.H. W. Effective chloride barrier for reinforced concrete structures in order to extend the service-life. In: Grosse CU, editor. *Advances in Construction Materials* Berlin, Heidelberg: Springer Berlin Heidelberg; 2007. p. 427-37.
11. Otieno M, Beushausen H, Alexander M. Chloride-induced corrosion of steel in cracked concrete – Part I: Experimental studies under accelerated and natural marine environments. Cement and Concrete Research. 2016;79:373-85.
12. Farsani AM, Keshtegar B. Reliability Analysis of Corroded Reinforced Concrete Beams Using Enhanced HL-RF Method. Civil Engineering Infrastructures Journal. 2015;48(2):297-304.
13. D. Schmidt, B. Shaw, E. Sikora, W. Shaw, L. Laliberte, Comparison of testing techniques used to analyze the corrosion resistance of sacrificial coating systems, Corrosion, 63 (2007) 958-974.
14. NACE International (2000) *Impressed current cathodic protection of reinforcing steel in atmospherically exposed concrete structures*. Houston, TX: NACE International (NACE standard, RP0290-2000).
15. J.P. Broomfield, *Corrosion of steel in concrete: understanding, investigation and repair*, CRC Press, 2006.
16. Tang F, Chen G, Brow RK. Chloride-induced corrosion mechanism and rate of enamel- and epoxy-coated deformed steel bars embedded in mortar. Cement and Concrete Research. 2016;82:58-73.
17. Ghanooni-Bagha M, Shayanfar MA, Reza-Zadeh O, Zabihi-Samani M. The effect of materials on the reliability of reinforced concrete beams in normal and intense corrosions. Eksploatacja i Niezawodność – Maintenance and Reliability 017;19(3):393-402.
18. Liberati EAP, Leonel ED, Nogueira CG. Influence of the reinforcement corrosion on the bending moment capacity of reinforced concrete beams: a structural reliability approach. Revista IBRACON de Estruturas e Materiais. 2014;7(3):379-413.

19. Frangopol DM, Lin K-Y, Estes AC. Reliability of Reinforced Concrete Girders under Corrosion Attack. *Journal of Structural Engineering*. 1997;123(3):286-97.
20. 211 AC. 211.1-91: Standard Practice for Selecting Proportions for Normal, Heavyweight, and Mass Concrete. ACI; 2002.
21. Zivica V. Corrosion of reinforcement induced by environment containing chloride and carbon dioxide. *Bulletin of Materials Science*. 2003;26(6):605-8.
22. Bastidas-Arteaga E, Soubra A-H. Reliability Analysis Methods. Stochastic Analysis Modelling: ALERT Doctoral School 2014; 2014.
23. Nowak AS, Collins KR. Reliability of Structures: McGraw Hill, USA; 2000.
24. El-Tawil S, Okeil AM. LRFD Flexural Provisions for Prestressed Concrete Bridge Girders Strengthened with Carbon Fiber-Reinforced Polymer Laminates. *Structural Journal*. 2002;99(2):181-90.
25. Okeil AM, El-Tawil S, Shahawy M. Flexural Reliability of Reinforced Concrete Bridge Girders Strengthened with Carbon Fiber-Reinforced Polymer Laminates. *Journal of Bridge Engineering*. 2002;7(5):290-9.
26. Okeil AM, Belarbi A, Kuchma DA. Reliability Assessment of FRP-Strengthened Concrete Bridge Girders in Shear. *Journal of Composites for Construction*. 2013;17(1):91-100.
27. American Association of State HT, Officials. AASHTO LRFD bridge design specifications, seventh edition, 2014, U.S. customary units : 2015 interim revisions 2014.
28. Changkyu Kim; Doeun Cho and H., Castaneda Corrosion Reliability and Probabilistic Model of Corrosion Initiation for Coastal Concrete Structures: Computational Framework, Materials and Structures, In review 2018
29. T. Onore, Okeil AM, H. Castaneda, M.R. Taha, A Framework for Reliability Assessment of Corrosion Damaged Reinforced Concrete Structures, proceedings of the 2018 World *Transport Convention Beijing, China, June 18-21, 2018*
30. Sohanghpurwala, A. A. (2006). "Manual on Service Life of Corrosion-Damaged Reinforced Concrete Bridge Superstructure Elements." NCHRP Report 558.
31. Yehia, S., Abudayyeh, O., Fazal, I. and Randolph, D. (2008). "A decision support system for concrete bridge deck maintenance", *Advances in Engineering Software*, 39, p202-210.
32. AASHTO LRFD Bridge Design Specifications. Washington, D.C. :American Association of State Highway and Transportation Officials, 2017. Print.
33. Castaneda, Homero; Karsilaya, Aydin; Okeil, Ayman; and Taha, Mahmoud Reda, (2018). Publications. 26. https://digitalcommons.lsu.edu/transet_pubs/26.
34. Castro-Borges, P., Balancán-Zapata, M., López-González, A. Analysis of Tools to Evaluate Chloride Threshold for Corrosion Onset of Reinforced Concrete in Tropical Marine Environment of Yucatán, México, *J. Chem.* 2013 (2013) 1–8. doi:10.1155/2013/208619.
35. Dai H, Wang W. Application of low-discrepancy sampling method in structural reliability analysis. *Structural Safety* 2009; 31(1): 55-64, <https://doi.org/10.1016/j.strusafe.2008.03.001>.
36. Darmawan MS, Stewart MG. Spatial variability of pitting corrosion and its effect on the reliability of prestressing wires. In: Der Kiureghain A, Madanat S, Pestana JM, editors. Ninth International Conference on Applications of Statistics and Probability in Civil Engineering, 1. Rotterdam: Millpress; 2003. p. 541–8.
37. Darmawan, M. S. (2010). "Pitting corrosion model for reinforced concrete structures in a chloride environment." 91-101.

38. Gonzalez JA, Andrade C, Alonso C, Feliu S. Comparison of rates of general corrosion and maximum pitting penetration on concrete embedded steel reinforcement. *Cement Concrete Research* 1995;25(2):257–64.
39. Hasaan, J., Bressollette P., Cheateaneuf, A., El Tawil, K. Reliability-based assessment of the effect of climatic conditions on the corrosion of RC structures subject to chloride ingress. 2010.
40. Liberati, E. A. P., Leonel, E. D., and Nogueira, C. G. (2014). "Influence of the reinforcement corrosion on the bending moment capacity of reinforced concrete beams: a structural reliability approach." *Revista IBRACON de Estruturas e Materiais*, Vol 7, Iss 3, Pp 379-413(3), 379.
41. Nogueira et al. Probabilistic Failure Modeling of Reinforced Concrete Structures Subjected to Chloride. 2012.
42. Okeil, Ayman M., et al. "Reliability Assessment of FRP-Strengthened Concrete Bridge Girders in Shear." *Journal of Composites for Construction*, vol. 17, no. 1, Jan. 2013, pp. 91-100. EBSCOhost, doi:10.1061/(ASCE)CC.1943-5614.0000315.
43. Stewart MG. Spatial variability of pitting corrosion and its influence on structural fragility and reliability of RC beams in flexure. *Structural Safety* 2004;26(4):453–70.
44. Turnbull, A. (1993). "Review of modeling of pit propagation kinetics." *Br. Corros. J.*, London, 28(4), 297–308.
45. Val DV. Deterioration of strength of RC beams due to corrosion and its influence on beam reliability. *J Struct Eng, ASCE* 2007;133(9):1297–306
46. Val DV, Melchers RE. Reliability of deteriorating RC slab bridges. *J Struct Eng ASCE* 1997;123(12):1638–44.
47. Vu K A, Stewart M G. Structural reliability of concrete bridges including improved chloride-induced corrosion models. *Structural Safety* 2000; 22(4): 313-333, [https://doi.org/10.1016/S0167-4730\(00\)00018-7](https://doi.org/10.1016/S0167-4730(00)00018-7).